STRESS METROLOGY AND THERMOMETRY OF AlGaN/GaN HEMTs USING OPTICAL METHODS

A Thesis
Presented to
The Academic Faculty

By

Sukwon Choi

In Partial Fulfillment
Of the Requirements for the Degree
Doctor of Philosophy in Mechanical Engineering

Georgia Institute of Technology

August, 2013

Stress Metrology and Thermometry of AlGaN/GaN HEMTs Using Optical Methods

Approved By:

Dr. Samuel Graham, Advisor
School of Mechanical Engineering
Georgia Institute of Technology

Dr. Heller
Materials and Manufacturing Directorate
Air Force Research Laboratory

Dr. Yogendra Joshi
School of Mechanical Engineering
Georgia Institute of Technology

Dr. Ting Zhu
School of Mechanical Engineering
Georgia Institute of Technology

Dr. Alan Doolittle
School of Electrical and Computer Engineering
Georgia Institute of Technology

Dr. Shyh-Chiang Shen
School of Electrical and Computer Engineering
Georgia Institute of Technology

Date Approved: July 1, 2013

PREFACE

Compared to the old days (perhaps one or two decades ago), the role and expectations for modern mechanical engineers have changed. Mechanical engineering itself involves diverse areas of study including thermal science, structural mechanics, analysis of dynamic systems, systems control, fluid mechanics, and so on and so forth. Conventional mechanical engineers were able to deal with indeed 'purely mechanical systems' such as automobiles, turbines, HVAC systems, etc. However, the problems that modern mechanical engineers face are different in nature. Even for the case of automotive industry, companies are increasing the number of hired engineers from disciplines other than mechanical engineering. Examples one may easily guess range from needs for building power windows to development of engine control units and by-wire systems, etc. Eventually automobile manufacturers are aiming for developing fully electrically driven vehicles due to environmental and political reasons and at the meantime we see hybrid type electric vehicles running on roads which are interim achievements leading to their final goal. To make these lengthy statements short, modern engineering problems that we face are virtually all 'multi-disciplinary' in nature.

This means modern mechanical engineers are required to gain base knowledge from different fields of studies or at least need to become able to 'talk' with collaborators from different engineering majors. The good news is that even under these circumstances, we can still keep our specialty that other disciplines do not cover. As a broad field of study, mechanical engineering is an essential knowledge base for virtually all engineering

problems and plays a crucial role in realization of brilliant ideas into actual products that contribute to improve the standard of life of the human race.

Personally, when I decided to major in mechanical engineering in 1998, I was thinking maybe someday I would be able to design and build a rocket flying to the moon or something similar. However, after having years of academic and industrial experience on automotive and residential hydrogen fuel cell systems (2005-2007) after graduating college, now I see myself having specialty in thermal characterization of microelectronics which I have never even imagined about. Once I had a serious agony about what my engineering identity was. But I've concluded, this is the real world and life that modern mechanical engineers are subject to. Therefore, I believe for mechanical engineers, it is important to not only have a sound foundation or specialty in terms of mechanical engineering but also not to fear challenging unfamiliar engineering problems, and instead, diving into those new areas to fulfill one's curiosity.

The study recorded in this thesis may be a good example that shows the progress of one naïve mechanical engineer adapting himself in a problem having its roots fastened deep into a totally different field of study and the process of discovering meaningful new findings with a different point of view from the engineers in the main stream. I remember the first question I asked to my thesis advisor Dr. Samuel Graham before joining his group. "I have no knowledge and no idea regarding this research project. Do you still feel I can work on it?" His answer was "No problem."

ACKNOWLEDGEMENTS

Firstly, I would like to give special thanks to my thesis advisor Dr. Samuel Graham for his guidance and encouragement throughout my PhD research at Georgia Tech. He was always patient, open to discussions, and considerate to my personal issues. While he let me do research independently most of the time, whenever I encountered problems, he helped me in person until all issues got cleared. His assistance was huge from the first moment I joined his research group so that I could successfully get accustomed to the research project that was entirely new to me. And at this point, where the time for leaving the group is close, his assistance still remains enormous, actively looking for numerous job opportunities for his student. I would like to express my gratitude and respect deeply from my heart for his courtesy and hospitality during my study at Georgia Tech.

I am deeply grateful to the Materials and Manufacturing Directorate of the Air Force Research Labs for financial support and Dr. Heller and Dr. Dorsey for fruitful discussions. They have never failed in their interest in my work and have always been there for me to discuss and learn from. Thanks to their support, the project work resulted in one book chapter, eight journal publications, and nine conference presentations. I would also like to thank Dr. Ramakrishna Vetury and Dr. Michael Hodge at RFMD for providing devices and giving me critical feedback in terms of electrical and commercial aspects of AlGaN/GaN HEMTs.

In addition, I truly appreciate the committee members Dr. Yogendra Joshi, Dr. Ting Zhu, Dr. Alan Doolittle, and Dr. Shyh-Chiang Shen for their time and guidance.

I wish many thanks to Dr. Thomas Beechem and Dr. Anusha Venkatachalam for conveying all the essential knowledge required for this research to me. The three month intense training with Thomas gave me capability to independently continue the research project after he left Georgia Tech. When I had trouble in understanding the device physics and reliability issues for AlGaN/GaN HEMTs, Anusha joined our group and was willing to dedicate your time and effort to assist me gain sufficient base knowledge for conducting the multi-disciplinary research.

Thanks must go to Dr. Jung-Il Hong at MSE department of Georgia Tech for XRD measurements. Thanks to Nick Burke and Dr. Eunah Lee at HORIBA Jobin Yvon for the spectrometer technical support. Thanks to Dr. Olivier Pierron, Eva Baumert, and Bhaskar Pant at ME department of Georgia Tech for the collaborative research, technical support, and training for device packaging. Thanks to Tamara Stephenson at Kyma Technologies for providing GaN samples. Thanks to Jeomoh Kim at MSE department of Georgia Tech for providing AlGaN/GaN heterostructure samples.

Thanks to all my colleagues, past and present, Dr. Yongjin Kim, Minseok Ha, Samuel Kim, Dr. Adam Christensen, Dr. Namsu Kim, Dr. Roderick Jackson, Dr. Anuradha Bulusu, Dr. Hossein Sojoudi, Nazli Donmezer, Shweta Natarajan, Hyungchul Kim, Mark Gleva, William James, Jason Jones, Yishak Habtemichael, Dr. Parisa Pour Shahid, Fernando Reiter, Prem Nagarathnam, Anne Mallow, and Yvette Chen for many social and occasionally scientific collaborations.

Finally, I owe an immeasurable debt of appreciation to my wife Sookkyung who has consistently shown unbounded love and support to me and my son Suhnjun. I enjoyed

only happiness during the past 5-year life in Atlanta for having a family relationship with them.

Thank you God for forgiving my sins, always being together with me, guiding me to the best pathways with abundant love, changing my sense of values, and opening my eyes to see the truth.

TABLE OF CONTENTS

LIST OF TABLES

LIST OF FIGURES

NOMENCLATURE

a	Lattice constant along the a-axis
a_0	Relaxed (unstrained) true a-lattice constant
c	Lattice constant along the c-axis
c_0	Relaxed (unstrained) true c-lattice constant
C_{ij}	Elements of elastic stiffness tenser
d	Inter-planar spacing along the in-plane direction / spot diameter
E	PL peak position (energy)
$\hat{E}$	Young's Modulus
E_0	Strain free PL peak position (energy) at room temperature
I_{dmax}	Maximum drain current
I_{dss}	Drain-source saturation current
k	Thermal conductivity
K_{PL}	PL biaxial stress conversion factor
$K_{RS}^{E2(high)}$	Biaxial stress conversion factor for the E_2(high) phonon of GaN
$K_{RS}^{A1(LO)}$	Biaxial stress conversion factor for the A_1(LO) phonon of GaN
$MTTF$	Mean time to failure
NA	Numerical aperture of objective lense
P	Dissipated power density
R^B	Biaxial relaxation coefficient
T_{base}	Baseplate temperature

T_{CH} *or* T_{ch}	Channel temperature
V_{gs}	Gate-source voltage
V_{ds}	Drain-source voltage
Y	Biaxial modulus

Greek Characters

α_a	Coefficient of thermal expansion along a-axis
α_c	Coefficient of thermal expansion along c-axis
Γ	Linewidth of the Raman peak
ε_a	Strain along the a-axis
ε_c	Strain along the c-axis
σ_a, σ_b	Biaxial stress in the c-plane
σ_c	Out of plane stress (along the c-axis)
$\hbar$	Planck's Constant divided by 2π
τ	Scattering time of a phonon mode
ω	Phonon frequency
ω_0	Phonon frequency at reference state
λ	Laser wavelength
ν	Poisson ratio

SUMMARY

The development of state-of-the-art AlGaN/GaN high electron mobility transistors (HEMTs) has shown much promise for advancing future RF and microwave communication systems. These revolutionary devices demonstrate great potential and superior performance and many commercial companies have demonstrated excellent reliability results based on multiple temperature accelerated stress testing. However, a physical understanding of the various reliability limiting mechanisms is lacking and the role and relative contribution of the various intrinsic material factors, such as physical stress and strain has not been clearly explained in the literature. Part of issues that impact device reliability are the mechanical stresses induced in the devices as well as the self-heating that also limit device performance. Thus, quantification of stress and temperature in AlGaN/GaN HEMTs is of great importance.

To address some of the needs for metrology to quantify stress in AlGaN/GaN HEMTs, micro-Raman spectroscopy and micro-photoluminescence (micro-PL) were utilized to quantify the residual stress in these devices. Through the use of micro-Raman and micro-PL optical characterization methods, mapping of the vertical and lateral stress distributions in the device channels was performed. Results show that stress can be influenced by the substrate material as well as patterned structures including metal electrodes and passivation layers.

Previously developed and reported micro-Raman thermometry methods require an extensive calibration process for each device investigated. To improve the implementation of micro-Raman thermometry, a method was developed which offers

both experimental simplicity and high accuracy in temperature results utilizing a universal calibration method that can be applied to a broad range of GaN based devices. This eliminates the need for performing calibration on different devices. By utilizing this technique, it was revealed that under identical power dissipation levels, the bias conditions (combination of V_{gs} and V_{ds}) alter the heat generation profile across the conductive channel and thus influence the degree of device peak temperature.

The role of stress in the degradation of AlGaN/GaN HEMTs was also explored. A combined analysis using micro-Raman spectroscopy, coupled electro-thermo-mechanical simulation, and electrical step stress tests was conducted to investigate the link between performance degradation and the evolution of total stress in devices. It was found that in addition to stresses arising from the inverse piezoelectric effect, the substrate induced residual stress and the operational themo-elastic stress in the AlGaN layer play a major role in determining the onset of mechanically driven device degradation. Overall, these experiments were the first to suggest that a critical level of stress may exist at which point device degradation will start to occur.

The optical characterization methods developed in this study show the ability to reveal unprecedented relationships between temperature/stress and device performance/reliability. They can be used as effective tools for facilitating improvement of the reliability of future AlGaN/GaN HEMTs.

CHAPTER 1

INTRODUCTION

1.1 AlGaN/GaN HEMTs

1.1.1 Device Physics, Applications, and Current Status

Gallium nitride (GaN) based systems are under development due to their potential use in not only advanced electronics but also optoelectronic devices in UV-C spectral regions. GaN is a direct wide band gap (~3.4 eV at room temperature) semiconductor with an attractive combination of very high breakdown electric field, good electron mobility, high saturated electron velocity, reasonable thermal conductivity, and stability at high temperatures (Fig. 1).

High electron mobility transistors (HEMTs) or heterostructure field effect transistors (HFETs) made from AlGaN/GaN are of great interest because these improved intrinsic material properties allow for large improvements in key material specific tradeoffs relevant to high frequency RF devices and power switches such as between power and frequency or on-resistance and breakdown voltage. These advantages distinct AlGaN/GaN HEMTs from conventional HEMTs, HFETs, metal semiconductor field effect transistors (MESFETs) or metal oxide semiconductor field effect transistors (MOSFETs) built with legacy materials. Notably, the material exists normally in a wurtzite phase which exhibits strong polarization in the c-direction (or <0001> direction)

that allows for very high carrier concentration densities and that are achievable without ionized dopants for c-plane, Ga-face AlGaN/GaN HEMTs (currently the most common growth direction for this technology). In Fig. 1, representative materials used for building transistors are qualitatively compared in terms of material properties relevant to device performance.

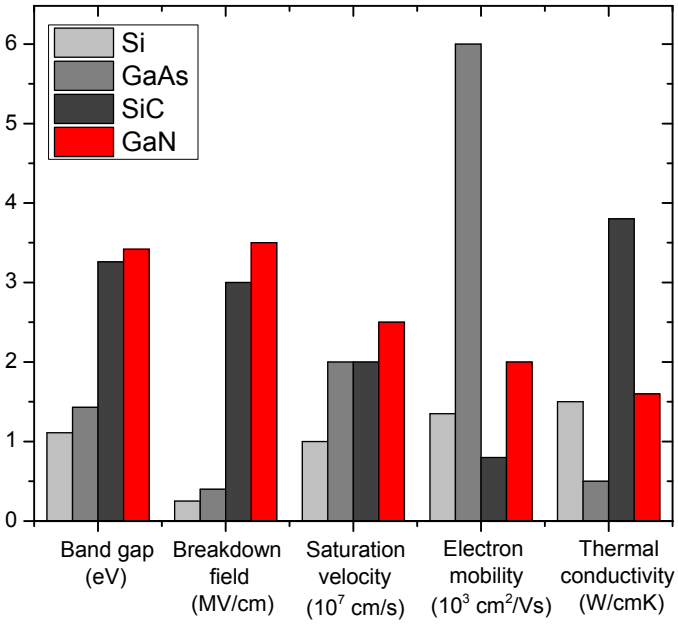

Fig. 1. Diagram of material properties for typical transistor base materials. The electron mobility shown for GaN refers to the mobility at the 2-DEG of an AlGaN/GaN heterostructure (2000 cm^2/Vs). The electron mobility in bulk GaN is 1000 cm^2/Vs.

The AlGaN/GaN system is highly analogous to AlGaAs/GaAs, also employed to build HEMTs. The most notable difference is that careers (electrons) in the two-dimensional electron gas (2-DEG) of AlGaAs/GaAs HEMTs are provided from a donor sheet in the AlGaAs layer whereas for AlGaN/GaN, the strong intrinsic (spontaneous)

and piezoelectric polarization of wurtzite GaN (and AlGaN) can easily generate enough sheet charge at the AlGaN/GaN interface to draw $>10^{13}$ cm^{-2} free electrons to the GaN side of this interface, forming a 2-DEG without the use of dopants [1]. Notably, this sheet charge arises from the crystal lattice itself and is periodic in nature so does not result in the ionized impurity scattering and mobility reduction that come from random ionized dopant atoms. Because polarization charge requires no thermal energy for ionization (unlike dopants), high carrier density is maintainable at very low temperatures which enables special applications such as deep space signal reception. Optionally, the AlGaN may be doped (in analogy to AlGaAs/GaAs), which with the existing large conduction band discontinuity at the hetero-interface can further increase the 2-DEG career concentration while still keeping 2-DEG electrons away from ionized scattering centers.

The polarization of the III-N materials is critical. Due to the non-centro symmetric crystal nature, i.e., lacking of an inversion center, of these III-V materials, AlGaN and GaN have spontaneous electric polarizations, and notably that of AlGaN is significantly larger. The sign is such that Ga-face grown material will contain positive sheet charge at the AlGaN/GaN interface due to the difference in polarization encountered at the interface. The thin AlGaN layer is pseudomorphically grown on the GaN layer. Thus the AlGaN layer's in-plane crystallography obeys that for the relatively thick GaN layer underneath. This means the crystal as well as thermal mismatches between the thin pseudomorphic layer (AlGaN) and the thick GaN layer are accommodated solely by elastic strain in the thin layer without any plastic relaxation or formation of misfit dislocations to match the GaN crystal lattice. The in-plane or a-lattice constant of AlGaN is smaller than that of GaN which decreases in size by increasing the Al mole fraction [2].

Therefore, the pseudomorphically grown AlGaN is under tensile strain with respect to GaN because of their lattice mismatch, and the resulting piezoelectric polarizations in the AlGaN adds to the positive sheet charge at the interface, resulting in a charge layer that can be well above 10^{13} cm^{-2} [1]. This charge does not go uncompensated, but instead a 2-DEG forms in the GaN buffer near the heterointerface. The 2-DEG sheet carrier density in this channel is typically about 10^{13} cm^{-2}, which is an order of magnitude higher than that of GaAs based HEMTs. This translates into their high current-carrying capabilities. Furthermore, the electron mobility and electron velocity in GaN remains at fairly high values even at elevated temperatures. Although Si and GaAs based structures can offer high mobility and electron velocity, they have smaller band gaps. GaN's wide band gap results in a large breakdown field (~3 MV/cm) which is about ten times higher than that for Si or GaAs. These superior material properties enable high power RF operation (large voltage and large current operation simultaneously) thus render AlGaN/GaN HEMTs as promising components for high temperature, high power, and high frequency electronics.

Due to lack of availability of GaN substrates, the III-N structure is typically grown by epitaxial techniques such as MBE or MOCVD on distinct substrate materials such as sapphire, Si, or SiC. Ohmic source and drain contacts are formed and the Schottky gate is deposited on the barrier material (AlGaN). A dielectric passivation layer (typically low temperature PECVD grown Silicon Nitride) covers the device which prevents charging of undesired surface states and protects the device from contaminants. Advanced design schemes can be implemented to control reliability issues in AlGaN/GaN HEMTs. For example, source connected field plates and T-gates can be added to mitigate the high electric field which develops at the drain edge of the gate in the presence of a large

voltage bias. A typical AlGaN/GaN HEMT structure is shown in Fig. 2.

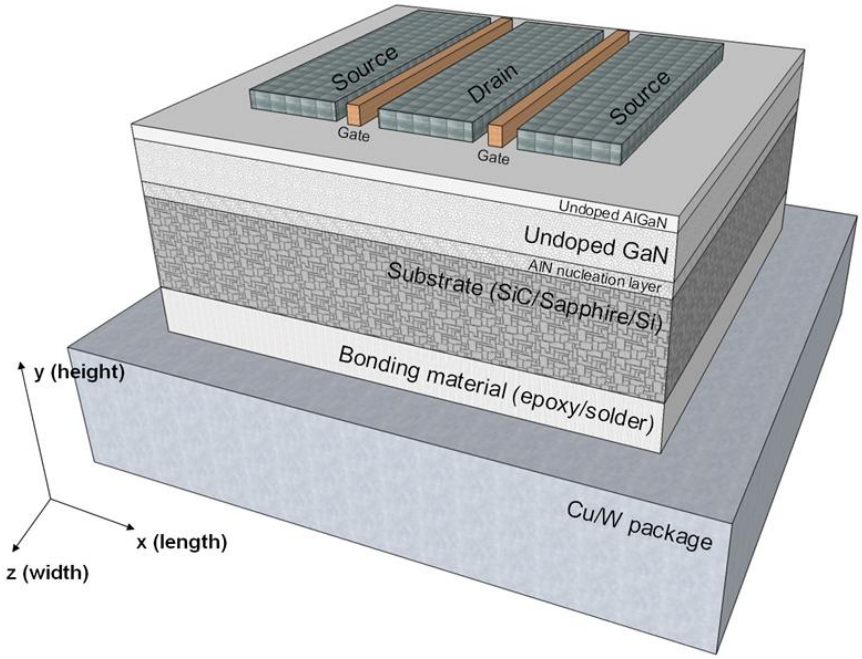

Fig. 2. Typical AlGaN/GaN HEMT structure.

AlGaN/GaN HEMTs are planned for or already finding wide applications in RF sources and power amplifiers for commercial ground base stations, satellite communications, and next-generation high data rate wireless communication systems thanks to their high power, high frequency, and broadband capabilities compared to relevant GaAs based parts. SiC is also capable of high voltage operation due to its wide bandgap (~3.2 eV) and is advantageous in terms of high power operation due to its very high thermal conductivity. However, devices based on SiC suffer from poor electron transport properties (Fig. 1) that hinder their use in high frequency applications [3]. By using AlGaN/GaN HEMTs, reduction in both overall system size and power consumption

(higher efficiency) is warranted [4].

There is a demand for AlGaN/GaN HEMTs in the automotive industry for power switching applications, for example, AC charging system and DC/DC buck converter used in hybrid electric vehicles (HEVs) [5]. GaN switches are advantageous over Si based counterparts, for instance, Si-insulated gate bipolar transistors (IGBTs), featuring substantially lower conduction and switching losses. Since GaN devices can operate at high temperature environments at more than 200 °C, the cooling system for the power control unit can be integrated with that for the engine compartment. These capabilities can lead into development of down-sized, lighter, and cost effective vehicle power control systems with higher energy efficiency.

Efforts are being made to develop low cost AlGaN/GaN HEMTs using Si substrates and active research is underway for heterogeneous on-wafer integration of GaN-on-Si devices and Si electronics as an alternative to direct competition with existing Si technologies [6].

Although these devices demonstrate great potential and superior performance, a physical understanding of the various reliability limiting mechanisms is immature. For Si and GaAs based transistors, the major concern or limiting factor in terms of device reliability was the relatively low breakdown voltage. In contrast, for AlGaN/GaN HEMTs, even though the nominal operating voltages are much higher, these conditions are far away from the breakdown voltage for these devices and developers have been facing new device degradation physics. Hot electrons induced by high electric fields can be trapped on or in the passivation, in the AlGaN, or in the GaN buffer and even generate traps which degrade device performance [7]. The inverse piezoelectric effect, on the other

hand, can drive a failure mechanism as a result of the electric field in the device where excessive tensile strain induced in AlGaN leads to formation of crystallographic defects in this layer [8]. The bias condition for operation is an important factor that determines which failure mode plays a dominant role in device degradation. This was shown in [7] comparing the impact of three bias conditions on device degradation, namely, pinch-off state (V_{gs}=-7.7 V, V_{ds}=20 V, highest gate-to-drain electric field in absence of carriers in the channel), semi-on state (V_{gs}=-5.5 V, V_{ds}=20 V, high electric field and existence of hot carriers in the channel), and on state (V_{gs}=0 V, V_{ds}=20 V, lowest electric field and highest population of less energetic electrons in the channel). Hot-electron degradation prevails at semi-on conditions with moderate V_{ds} (<30 V) since a fairly high current and electric field present in the device induces a large population of hot electrons. At pinch-off states with high V_{ds} (>30-50 V), the inverse piezoelectric effect becomes prominent due to highest V_{gd} in the device. In contrast, in the fully on state junction temperature is typically highest with potential to degrade the Schottky gate and ohmic contacts, drive thermal diffusion and intermixing processes, and form material defects (wear-out) thus causing device failure or reliability problems. Clarification of the physical mechanisms underlying the various reliability limiting mechanisms is a topic of great interest to the GaN HEMT community. Many factors have been postulated in the literature on this subject since early 2000.

Understanding of device degradation physics is the first step to improve the device reliability. For this reason, not only conducting electrical measurements along with accelerated lifetime tests but also performing mechanical characterization is essential. Micro-Raman spectroscopy and micro-photoluminescence (PL) are noncontact and

nondestructive optical material characterization techniques with adequate submicron spatial resolutions suitable for *in situ* investigation of AlGaN/GaN HEMTs in terms of examining mechanical stress and temperature during device operation. In the following subsections, a presentation accounting for current reliability concerns involving mechanical effects (structural and thermal) is given. Also the adopted optical characterization techniques (micro-Raman spectroscopy and PL) are briefly introduced and their advantages over other conventional stress/temperature measurement methods are discussed.

1.1.2 Reliability Concerns: Structural

At present, most of commercial GaN layers implemented in AlGaN/GaN HEMTs are obtained by hetero-epitaxy on substrates with lattice and symmetry similarities due to limitations (size, cost, quality, availability) in commercially available free-standing GaN substrates. Sapphire has been a low cost conventional substrate extensively used by having a good epitaxial relationship with GaN. Despite its high cost, SiC exhibits significant advantages over sapphire (and Si). Smaller lattice constant mismatch and thermal expansion coefficient difference with GaN allows growth of high-quality GaN films with low dislocation density. The high thermal conductivity of SiC (an order of magnitude greater than that of Sapphire) prevents excessive heating in GaN devices and enables high power operation. Si substrates are under keen interest due to their low cost, large wafer size, high crystal quality, and good thermal conductivity, and used commercially when the cost-performance tradeoff makes this advantageous, such as for

large power switches. Si substrates may allow the integration of GaN devices into Si microelectronics as well. However, deposition on Si substrates is not ideal due to the large mismatch (especially thermal mismatch) between Si and GaN crystal structures. Growth of GaN on diamond substrates and their application (GaN on diamond HEMTs) have also been reported which offers potential for development of HEMTs with even higher power outputs and higher density layouts.

However, the thin GaN hetero-epitaxial layers inevitably possess a residual strain (or stress) due to the growth process on lattice mismatched substrates and post-growth cooling with difference in thermal expansion coefficients between the substrate material and the GaN epitaxial layer. Strain from defects which is usually tensile arises due to point defects, dislocations, stacking faults, and twins [9]. Thus details of the buffer layer also modify the stress in the GaN layer significantly [10]. This stress is commonly biaxial across the thin GaN film and stress free in the growth direction. It has been reported that GaN grown on sapphire contains compressive stress while GaN on 6H-SiC and Si is under tensile stress [11], [12], [13] (for GaN grown on SiC, the stress can also be compressive, depending on the processing method). Excessive residual stress induces formation of dislocations, stacking faults, and cracking near the GaN-substrate interface which leads to degraded performance and shortened lifetime in GaN-based electronic devices [14]. Furthermore, wafer bowing caused by residual stress can complicate device fabrication and residual stress also affects optical and electrical properties of the GaN epi-films. Therefore, stress information in not only the AlGaN barrier but also the GaN layer is crucial in terms of improving device performance and reliability of high power GaN based devices.

In addition, mechanical stress inherent in the AlGaN layer of AlGaN/GaN HEMTs due to the hetero-epitaxial growth and other processing methods can negatively impact device performance. The 2-DEG in AlGaN/GaN HEMTs is responsible for the high current capability and is created in response to the large spontaneous/piezoelectric polarization in AlGaN which causes electrons to drift towards the hetero-interface and aggregate into the quantum well. The electronic performance of these devices is mainly limited by the sheet carrier density and electron mobility in the 2-DEG. These electrical properties are a strong function of the mechanical strain built in the AlGaN layer. For example, imposing tensile in-plane strain in the AlGaN layer increases the piezoelectric field thus results in higher 2-DEG sheet carrier density in Ga(Al)-face heterostructures. Stress-induced effects on device performance due to Al content [15], [16], passivation [17], and substrate-induced residual stress in the GaN layer [18] have been reported. Simply operating AlGaN/GaN HEMTs leads to a vertical electric field in the device structure which generates inverse piezoelectric strain. Under high voltage conditions, the large electric field in the vicinity of the drain side gate edge is responsible for generation of large in-plane tensile strains in the AlGaN layer. These strains can result in device degradation via the formation of electrically active defects or trap states near the gate in the AlGaN [8] (Fig. 3). Mitigation of the inverse piezoelectric stress can be realized by smoothing the peak electric field by introducing field plates. From the mechanics point of view, minimizing the built-in residual strain in the AlGaN layer at non-biased conditions is important but accompanies a trade-off in less output power due to a smaller 2-DEG sheet carrier density.

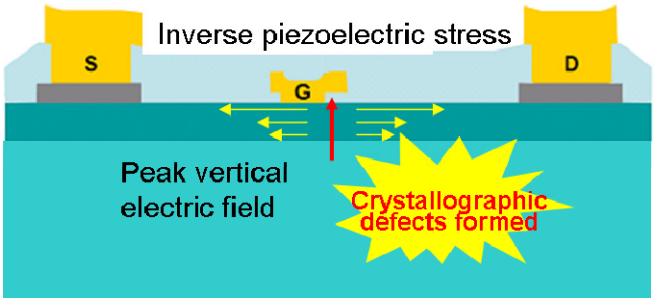

Fig. 3. AlGaN/GaN HEMT degradation driven by the inverse piezoelectric effect**.**

1.1.3 Reliability Concerns: Thermal

As AlGaN/GaN devices can operate at exceptionally high power densities, for example, over 30 W/mm [15], the overall power is large and as a consequence, considerable heat generation in the active region becomes a crucial issue in terms of device performance and reliability. Considerable self-heating negatively impacts transport properties. The electron mobility and drift velocity reduce with increasing temperature mainly due to enhanced polar optical phonon scattering that in turn decreases the device output current and operational frequency (i.e., a decrease in DC and RF performance). Current saturation occurs at an applied electric field that is much lower than the electric field required (~200 kV/cm) for electron drift velocity to saturate in bulk GaN [19]. The self-heating effect is also observable in the I-V characteristics, i.e., negative DC output conductance at large V_{ds} conditions. Excess high junction temperature has potential to degrade the stability of gate Schottky and ohmic contacts as well as form material defects, thus causing reliability problems and even device failure.

Under normal operating conditions, a peak electric field is concentrated over a small

region in the vicinity of the drain side gate edge near the AlGaN/GaN interface [20]. This intense electric field spike can lead to breakdown even for relatively small values of V_{ds}. An extremely high electric field can occur in conventional structures which do not employ field-plates or recessed gates. The energetic or hot electrons generated by the high electric field lose energy to the lattice primarily by emitting longitudinal optical (LO) phonons via Fröhlich interaction ('A Coulomb interaction between electrons and the longitudinal electric field produced by the LO phonons [21]') due to the strong ionic nature of GaN. Generally, the GaN A_1(LO) phonon lifetime is significantly longer than that for other wurtzite materials such as AlN [22]. There is a large gap in phonon density of states between the acoustic and optical phonon branches [23]. Thus simple decay paths such as two-phonon symmetric decay are not possible. Hot electrons relax predominantly by LO-phonon emission in GaN since it is a polar semiconductor. The long LO phonon lifetimes in GaN enhance hot phonon effects which increase relaxation times of hot carriers. This phenomenon exacerbates thermal energy dissipation or hot spot formation. The group velocity of an optical phonon is near zero thus the emitted LO phonons remain in the channel until they either are reabsorbed by electrons or decay into transverse optical (TO) phonons and acoustic phonons. Acoustic phonons play a role to effectively transport the Joule heat away from the active region of the device towards the substrate. In the 2-DEG, the LO phonon decay time or lifetime (~350 fs) considerably exceeds the LO phonon emission time by a hot electron (~10 fs) [24]. Thus at the drain end of the gate electrode where the lateral electric field is highest, a localized accumulation of non-equilibrium LO phonons or so-called hot phonons takes place which acts as a bottleneck in thermal energy transport. At this local region a nanoscale "hot spot" (diameter of 10-

100 nm [25]) in lattice temperature forms as a result of the combination of electric field spike, complex phonon interactions, and ballistic transport effects [26]. This hotspot formation mechanism is briefly illustrated in Fig. 4. Determining the temperature rise in AlGaN/GaN HEMTs under these conditions using conventional thermal models (using diffusion type conduction heat transfer equations) based on power dissipation alone is thus incorrect. This fact reflects needs for more advanced modeling schemes or experimental methods that can estimate the channel temperature with reasonable accuracy.

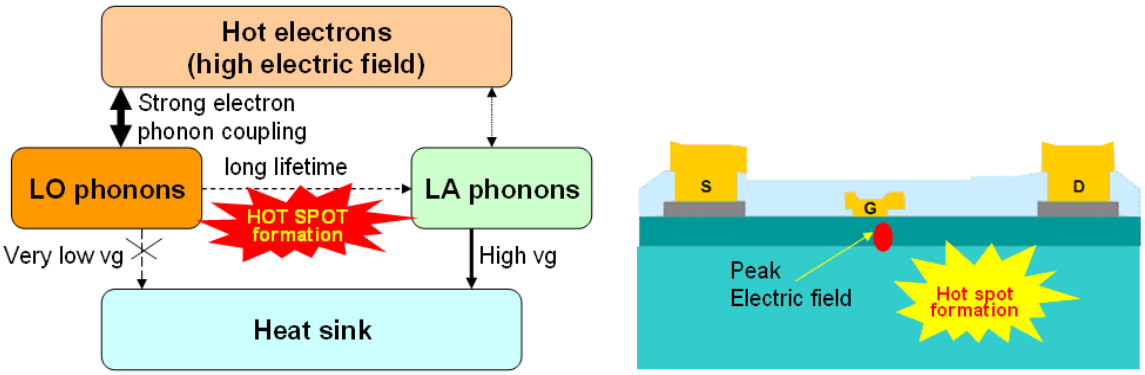

Fig. 4. Hot spot formation mechanism for operational AlGaN/GaN HEMTs.

1.2 Experimental Methods to Quantify Temperature and Stress in AlGaN/GaN HEMTs

In this section typical techniques that have been commonly used for characterizing mechanical stress and temperature of semiconductor devices are introduced. Then the suitableness of utilizing Raman spectroscopy and photoluminescence (PL) spectroscopy

for analyzing AlGaN/GaN HEMTs in terms of structural and thermal aspects is discussed.

1.2.1 Stress measurement techniques

In measuring residual stress using x-ray diffraction (XRD), the strain in the crystal lattice is calculated based on measured lattice parameters and the associated stress is determined using the elastic stiffness coefficients assuming linear elastic deformation. This non-destructive method is applicable to crystalline materials including not only semiconductors but also metallic or ceramic materials with relatively small or fine grain size. Another method to determine stress in thin epi-films is wafer curvature method (WCM). Based on measured wafer bows, the radius of curvature is calculated, and the average stress in the film is calculated using Stoney's formula. This technique also requires knowledge of elastic properties of materials under interest. Even though both of these techniques have been widely used for quantifying the residual stress in GaN epi-films [27], they are more suitable for estimating wafer level film stress. These methods are inadequate for determining local variation of stress in AlGaN/GaN HEMTs due to their large probing area. HRXRD is more sensitive to the stress near the surface of the wafer whereas WCM is sensitive to the stress at the epilayer interface.

1.2.2 Thermometry techniques

Infrared (IR) micro-thermography is a widely used tool to image temperature

distributions of electronic devices. This is a tool passive optical technique utilizing naturally emitted IR radiation from a surface. However, it was shown in [28] that this technique significantly underestimates the channel temperature of AlGaN/GaN HEMTs. Emissivity calibration issues related with background radiation is one problem. The low lateral resolution (~10 μm) limited by the wavelength of the IR radiation from the device surface, and the fact that IR radiation is transparent to wide bandgap materials including GaN limit the accuracy of this technique and makes it inadequate for estimating the channel temperature occurring in operating AlGaN/GaN HEMTs.

Electrical temperature sensitive parameter (TSP) methods such as the DC characterization method were utilized to measure the channel temperature of AlGaN/GaN HEMTs [29]. DC characterization method relies on the negative differential resistance in the HEMT output characteristics originating from self-heating effects. This is a noninvasive and fast technique requiring simple experimental apparatus. In addition, measurement is not limited by the device layout and also works for fully packaged devices. However, as pointed out in [30], electrical TSP techniques probe an electrical average temperature over a large domain (entire source-drain gap for the DC electrical method) whereas significant inhomogeneous lateral gradients are present in operating AlGaN/GaN HEMTs. Thus the obtained temperature values are significantly lower than the actual device peak temperature. Also TSP methods need to rely on drastic simplifying assumptions which place the measurement accuracy in question.

Liquid crystal thermography (LCT) uses nematic liquid crystals which change crystalline order from the nematic or anisotropic phase into isotropic phase at a known temperature. Accordingly, the optical state of the liquid crystal changes as well. A liquid

crystal layer with thickness on the order of several micrometers is deposited over an electronic device, e.g., transistor, and illuminated with a polarized light. The reflected light is monitored through another polarizer (analyzer). Above the phase transition temperature, the reflected light remains its polarization orientation. Below this temperature, the polarization orientation of the reflected light is altered. This technique has been used for hotspot identification and temperature measurement of electronic devices and was applied for measuring the surface temperature of AlGaN/GaN HEMTs [31], [32]. LCT offers simplicity in measurement, high spatial resolution and relatively low system cost but finding a liquid crystal having optimal transition temperature (which one would prefer to equal to the maximum device operating temperature) suitable for a particular device is uneasy. In addition, it is not easy to properly apply the crystal over the device surface and maintain the crystal layer during measurement.

Thermoreflectance is another technique that has been used for monitoring surface temperature of AlGaN/GaN HEMTs [33]. Temperature rise induces a change in the optical reflectance of the surface of some materials. This technique measures the change in reflection amplitude of visible wavelength illumination using a CCD camera and generates a two 2-D map of the surface temperature distribution. Sub-micron spatial resolution is achievable using visible light. However, low signal to noise ratio obscures obtaining accurate temperature information of materials having low values of thermoreflectance coefficients which quantitatively represents the material's reflectivity change in response to temperature rise.

Atomic force microscopy (AFM) can also serve as a thermometry tool with spatial resolution limited solely by the size of the thermal probe which can be only a few

nanometers [34], [35]. Thermal resistance between the material surface and probe as well as the heat capacity of the probe needs to be taken into account to raise the accuracy of measurement results. Physical contacting methods such as AFM are not preferred for measuring operating semiconductor electronic devices.

1.2.3 Active optical techniques

Raman spectroscopy and photoluminescence (PL) provide non-contact and fast means to locally analyze microscale devices such as AlGaN/GaN HEMTs with sufficient spatial resolutions of ~1 μm [36]. The probing area of both of these optical methods is limited by the device layout, i.e., optical access to the semiconductor material is required.

Micro-Raman spectroscopy measures phonon frequency of semiconductor materials thus is capable of indirectly measuring stress and temperature [37]. Sub surface depth profiling measurement can be done in confocal mode and sub-microsecond transient measurements can also be made [38]. Information from metal layers is not obtainable due to fluorescence effects and their low phonon energies. Measurement over a large area using micro-Raman spectroscopy is not an easy task as it requires positional scanning and long data acquisition times unlike IR thermography or thermoreflectance. Visible Raman spectroscopy can serve as an effective *in situ* tool for examining operating devices since interference to the electrical performance of the device by photon irradiation can be minimized by utilizing a sub-bandgap visible laser with reduced power.

PL spectroscopy utilizes a monochromatic light source with photonic energy larger than the bandgap energy of the semiconductor monitored. The incident laser light is

absorbed at the surface of the material creating electron-hole pairs. The energy bandgap of the material is detected from the radiative decay of photo-excited carriers during their thermalization or recombination process. The bandgap energy is known to vary with temperature and applied stress. PL should be utilized with caution when measuring devices under electrical bias since free carrier generation occurs at the illuminated region, typically the channel or active region when measuring AlGaN/GaN transistors. Even when measurement is taken under an unbiased state, laser power has to be carefully adjusted not to induce local heating by laser light absorption.

As seen in the foregoing subsections 1.2.1 and 1.2.2, a wide variety of techniques exist for measuring mechanical stress and operating temperature in semiconductor devices. Ultimately, the choice of technique depends on several factors including the type of devices studied, required accuracy, and spatial resolution, etc. Active optical methods were employed in this study as they seemed to be the most optimal techniques for investigating stress and temperature distributions and relevant physical phenomena occurring in the channel of AlGaN/GaN HEMTs. A more detailed overview of Raman and PL spectroscopy will be given in Chapter 2.

1.3 Outline of Study and Contributions

The study developed in this work can be broken into two major parts: i) development of methods to measure stress and temperature of AlGaN/GaN HEMTs using optical material characterization techniques, and ii) a reliability study that involves electrical stress tests, optical stress/temperature measurements, and multi-physics based simulation

intended to highlight the role of mechanical effects in the electric field induced degradation of AlGaN/GaN HEMTs postulated in [8]. These studies were conducted to obtain better understanding in device degradation physics in order to facilitate realization of GaN electronics.

First, in Chapter 2, a detailed presentation regarding the underlying physics of the optical techniques adopted in this work, i.e., Raman spectroscopy and PL, that relate the correlation between stress/temperature and their optical responses is given.

For stress measurement, first a self-consistent framework combining XRD, Raman spectroscopy, and PL was developed in Chapter 3. Strain free references and conversion factors required for stress assessment of GaN thin films using Raman spectroscopy and PL were determined. This was attempted to overcome dispersion or inconsistency in stress metrologies using Raman spectroscopy and PL reported in past literature. The parameters obtained can be utilized with confidence to measure stress in GaN based devices. The developed method provides efficient means of process feedback in terms of stress monitoring utilizing optical techniques (Raman spectroscopy and PL) between fabrication steps in the test and development stage of GaN devices.

The stress measurement methods developed were applied to actual devices in Chapter 4 for measuring residual stress in the channels. This yielded insight into lateral as well as vertical gradients of stress present in the conductive channel of AlGaN/GaN HEMTs for the first time in literature. This observation of the stress distribution within the conductive channel revealed that tensile strain is induced in the AlGaN layer near the edge of metal electrodes. This means metallization schemes that induce compressive strain in the AlGaN layer or proper passivation overlayer deposition that results in less tensile strain at

its edges will be beneficial in terms of device reliability.

In Chapter 5, a time-efficient, simple, and accurate Raman thermometry method utilizing linear relations between stress/temperature and frequencies of multiple phonon modes was developed. This method does not require a temperature calibration process since it mainly relies on intrinsic characteristics of the material under interest, i.e., GaN. However, this method must be used only when biaxial stress is present within the c-plane of GaN.

Various Raman thermometry methods including the '2-peak fit method' developed in Chapter 5 were applied to device measurement in Chapter 6 in order to study complex thermal phenomena occurring in AlGaN/GaN HEMTs under operation. The effect of electrical biasing conditions on the self-heating in AlGaN/GaN devices was examined. Bias-dependent self-heating in non-field plated devices was investigated experimentally and verified by coupled electro-thermal simulation. Among diverse bias conditions resulting in same power dissipation, the heat generation region becomes more concentrated into a nanoscale domain under the drain end of the gate at bias conditions with higher V_{ds} and more negative V_{gs}. Consequently a higher channel temperature results compared to that for conditions with lower V_{ds} and less negative V_{gs} even though the overall dissipated power in the device is identical. Since Raman spectroscopy probes the depth average stress in the GaN layer, electro-thermal simulation was performed to extrapolate the peak channel temperatures. This bias dependent thermal effect exerts local peculiarity in the device and should be taken into account in lifetime testing and fundamental reliability studies for AlGaN/GaN HEMTs.

Chapter 7 shows further extension of the studies conducted through Chapter 3 and 6

in conjunction with electrical stress tests and multi-physics based simulation. Coupled electro-thermo-mechanical simulations were utilized to quantify the mechanical stresses induced in the AlGaN layer of AlGaN/GaN HEMTs originating from different physical effects, i.e., thermo-elastic and inverse piezoelectric effects, under different voltage bias conditions. Electric field driven device degradation was investigated in a mechanics point of view by monitoring the magnitude of total stress induced in the AlGaN layer under the drain side corner of the gate at operating conditions where the onset of electrical performance degradation took place.

The overall objective of this work is to supplement reported degradation schemes with characterization of mechanical properties (stress and temperature) using novel optical techniques (Raman and PL spectroscopy) and reveal complex phenomena occurring in devices that deserve attention in the test and development stage of AlGaN/GaN HEMTs.

CHAPTER 2

OPTICAL CHARACTERIZATION TECHNIQUES: RAMAN AND PHOTOLUMINESCENCE SPECTROSCOPY

In this chapter, a brief introduction to the underlying physics of micro-Raman spectroscopy and micro-photoluminescence spectroscopy is given. Then their applicability to temperature and stress quantification in thin GaN epi-films is discussed. A survey of past efforts and methodologies developed in literature regarding these applications is presented.

2.1 Raman Spectroscopy

2.1.1 Theory

Raman spectroscopy is an optical scattering technique that is used to probe the vibrational energies or frequencies of the (Raman active) optical phonons in a material. Raman scattering is observed by the energy difference between the incident light and radiation scattered from the sample which corresponds to the molecular vibrational frequency. In the light scattering process the electric field of the radiation interacts with a molecule by distorting the electron cloud around the chemical bonds in the molecule. Electrons are promoted to a so-called virtual state and return to their ground state by reradiating photons. Here the dominant process is elastic scattering, i.e., no energy

change, where the frequency of the light incident upon the sample and that of the scattered light are identical. This process is called Rayleigh scattering. However, there exists an inelastic scattering process that occurs for one out of 10^6-10^8 photons such that quantized vibrational energy levels of the molecule get involved during the scattering process. As a consequence, this vibrational energy is transferred either from the incident photon to the molecule (Stokes) or from the molecule to the scattered photon (anti-Stokes). This process is Raman scattering. This elucidation of Raman scattering was based on non-interacting randomly oriented molecules in gas or liquid phase. When solid samples such as semiconductors are under the Raman scattering process, the energies of quantized lattice waves or so-called phonons are observable. The Raman scattering process is illustrated in Fig. 5.

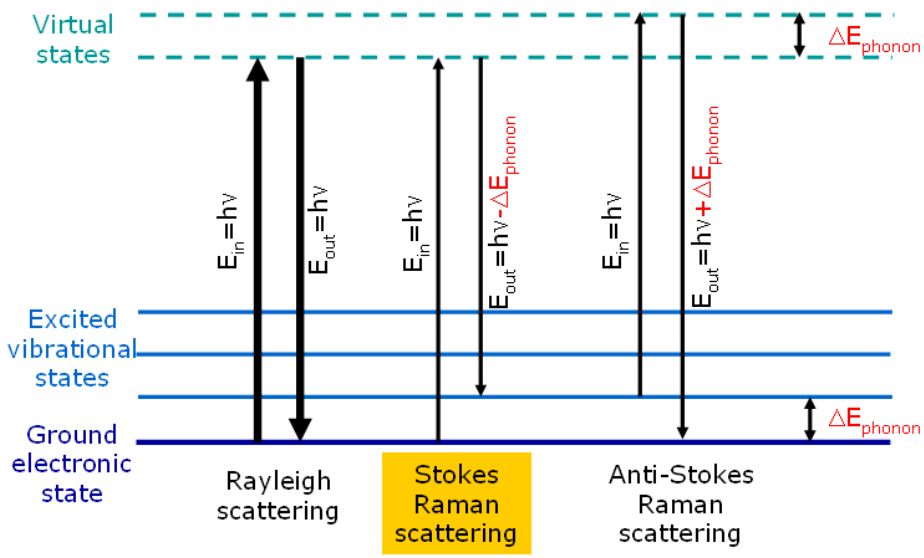

Fig. 5. Energy level diagram for Rayleigh and Raman scattering processes.

Modern Raman instruments are equipped with lasers that are capable of irradiation on a sample with very high photon density and provide a wide range of choice to be utilized as a light source of single frequency well away from the absorption band of the illuminated material. Therefore, Raman spectroscopy has become a routine tool comparable to IR absorption spectroscopy. Usually Raman scattering is recorded only on the low energy side from the energy of the source laser beam to give the Stokes Raman shift since the Stokes signal intensity is much higher than that of the anti-Stokes signal at room temperature. Using a harmonic approximation for the potential energy curve between atoms that constitute the molecule, it is easily deduced that the lighter the atoms are and the stronger the bond is, the higher the vibrational frequency will be. Raman scattering is expressed as a shift in energy from that of the exciting radiation usually in wavenumbers (cm^{-1}). In Raman spectroscopy, this linear wavenumber scale is commonly used because it has a direct proportionality with energy and frequency. The relationship among wavenumber ($\bar{\omega}$),energy (E), frequency (v) and radiation wavelength (λ) is $E=hv=hc/\lambda=h\bar{\omega}$ where h is Planck's constant (6.626×10^{-34} J•s) and c is the speed of light (2.998×10^{8} m/s).

Molecular vibrations that cause a change in the polarizability of the molecule that varies as a function of the distance between constituent nuclei result in efficient Raman scattering and called to be Raman active. This contrasts with vibrations that induce a net change in dipole moment or charge distribution whereon absorption of the radiation takes place when the radiation frequency (mid-IR region) exactly matches the natural vibrational frequency of the molecule (IR active). This distinction is referred to as the selection rule. Raman spectroscopy and IR absorption are thus complementary techniques,

especially for non-centro-symmetric molecules, to extract information of the vibrational characteristics of a molecule. An excellent presentation of a classical approach to the theory of Raman scattering is given in [39] with more details.

2.1.2 Stress Measurement using Raman spectroscopy

Micro-Raman spectroscopy provides effective means to examine stress in microscale AlGaN/GaN HEMTs. Lateral resolutions are on the order ~1 μm while the depth resolution depends on the excitation wavelengths and optical properties of the AlGaN/GaN layers.

Micro-Raman spectroscopy probes the energy or frequency associated with Raman active phonon modes. The zone-center (Γ point, k≈0) phonons are responsible for the first-order Raman scattering due to the energy and momentum conservation rules in the light scattering process. The material response to applied strain is observed through the Stokes peak position shift of the observed Raman active modes from its true strain free value [40]. With the laser incidence along the normal direction of the basal plane (i.e., parallel to the c-axis of the GaN layer which is also normal to the surface for Ga face growth most commonly used for AlGaN/GaN HEMTs) and a 180° backscattering configuration, the allowed zone-center optical phonon modes detectable for hexagonal wurtzite GaN (C_{6v}^{4} space group symmetry) are A_1(LO) (~734 cm^{-1}), E_2(low) (~143 cm^{-1}), and E_2(high) (~568 cm^{-1}), unless there are disoriented microstructures [41]. The E_2(high) mode of GaN corresponds to the atomic oscillation in the c-plane which has a non-polar character as shown in Fig. 6. Its mode frequency is therefore sensitive to the lattice strain

in the c-plane and suitable for examining the in-plane biaxial stress in GaN epifilms [42]. In general, the E_2(high) phonon frequency decreases in comparison to that of strain free GaN as tensile biaxial stress in the c-plane is applied. This phenomenon can be explained by the elongation of the bonds perpendicular the c-axis followed by relaxation of the force constants. The change in interatomic forces between atoms results in a change in the vibrational frequency.

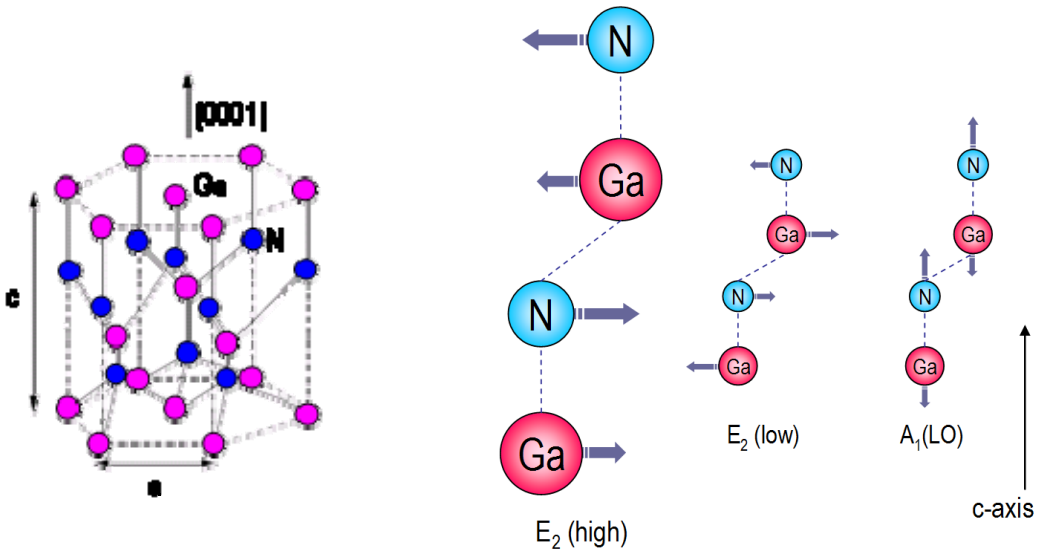

Fig. 6. Wurtzite crystal structure of GaN and graphical description of atomic vibration modes in hexagonal (wurtzite) GaN.

The following descriptions introduce past efforts made in literature to quantify stress built in GaN thin films or GaN based devices using micro-Raman spectroscopy. A number of studies attempted to investigate the degree of mechanical stress residing in AlGaN/GaN HEMTs as a performance limiting factor and/or its impact on device reliability. A consistent description of the biaxial and hydrostatic stress in GaN thin films utilizing Raman spectroscopy, photoluminescence, and x-ray diffraction was reported in

[43]. A combined analysis employing Raman spectroscopy and photoluminescence to investigate biaxial stress in GaN epilayers grown on Si, 6H-SiC, and sapphire was presented. Roles of the AlN buffer, lattice and thermal mismatch between the GaN epilayers and the substrates to residual strain in the films was discussed [44]. A critical review of discrepancies between experimental and theoretical results in literature with regards to elastic properties, electronic as well as phonon deformation potentials and the respective strain and stress coefficients of uniaxially and biaxially stressed GaN and AlN was given based upon ab initio studies using a pseudopotential-plane-wave method [45]. The relationship between band gap and biaxial stress of wurtzite ZnO and GaN was investigated by side-inclination x-ray diffraction, optical absorbance spectrum, and ab initio calculation [46]. Raman spectroscopy was used to study the inverse piezoelectric strain in AlGaN/GaN HEMTs via observation of the E_2(high) phonon frequency shift between biased (pinch-off) and unbiased states. The inverse piezoelectric strain in GaN was shown to be related with the magnitude of the vertical component of the electric field in GaN layer [47]. The magnitude of stress loads that evolve during AlGaN/GaN HEMT operation, i.e., operational thermo-elastic stress, inverse piezoelectric stress, and residual stress, were quantified by simultaneously utilizing the Stokes peak position and linewidth of the Raman signal. It was shown that GaN on Si devices exhibited more tensile residual stress at room temperature and more compressive thermo-elastic stress under operation compared to GaN on SiC devices with similar structures whereas the magnitude of inverse piezoelectric stress induced between gate and drain in the GaN layer were comparable (compressive) at comparable pinch-off conditions [48].

2.1.3 Raman Thermometry

Micro-Raman spectroscopy can also be utilized as an effective tool for monitoring the channel temperature of AlGaN/GaN HEMTs. A brief introduction to Raman theory was covered in section 2.1.1. In general, a temperature rise in GaN results in a red-shift in phonon frequency and increase in the phonon linewidth due to anharmonic effects. The downshift in phonon frequency at high temperatures originates from thermal expansion of the lattice and phonon self-energy suppression, i.e., decay of phonons by dissipating the phonon energy to lower frequency modes such that the energy and momentum are conserved [49]. Here the dominant contribution comes from the thermal expansion. The increase in interaction among optical phonons at high temperature results in increased phonon scattering and thus decreased phonon lifetime. The phonon linewidth Γ (cm^{-1}) is related with the phonon lifetime τ via the energy-time uncertainty relation $\Gamma/\hbar = 1/\tau$ where $\hbar$=5.3×10-12 cm^{-1}s [50]. Therefore rise in temperature accompanies phonon peak broadening. The foregoing discussions about the influence of temperature to the Raman signature of GaN as well as the effect of stress introduced in section 1.2.2 are illustrated in Fig. 7.

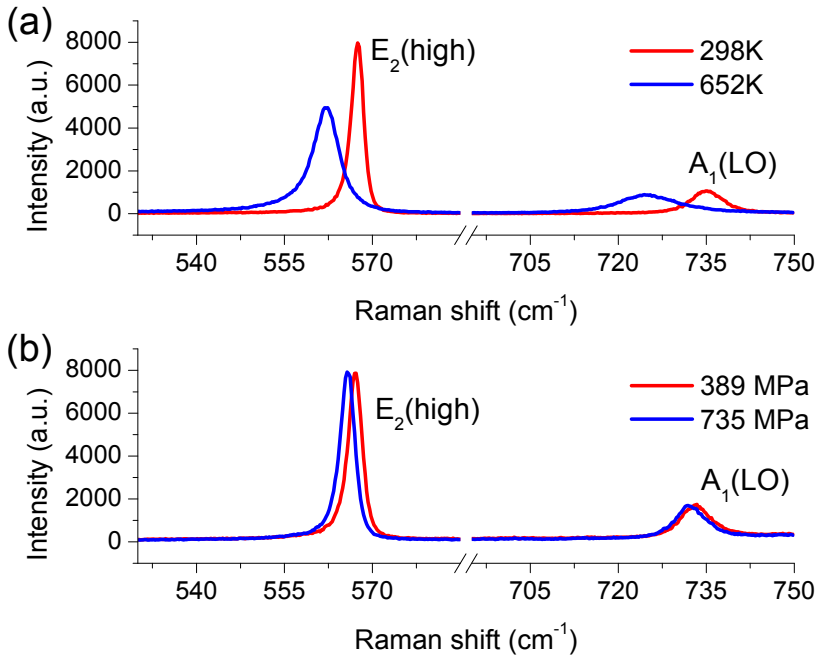

Fig. 7. GaN's Raman response to (a) temperature rise and (b) application of biaxial stress. In (a), a bulk GaN substrate was measured while isothermally heated up to known temperatures. Generally, temperature elevation leads to red shift, broadening, and decrease in intensity of Stokes Raman peaks. Measurements in (b) were taken at room temperature (25 °C) where different levels of tensile stress were applied to a GaN/6H-SiC template.

The typical method to measure temperature using Raman spectroscopy is to utilize the Stokes Raman peak shift. Operating temperature measurement of AlGaN/GaN HEMTs using Raman spectroscopy was first performed in [51] utilizing the temperature dependent E_2(high) phonon frequency shift. However, since as discussed previously phonon frequency is also sensitive to the lattice strain, the accuracy of this technique is subject to errors arising from stresses that stem from sources including thermo-elastic and inverse piezoelectric effects that develop during device operation. In addition to the temperature induced shift in phonon frequencies, mechanical stress also alters the frequencies of the vibrational modes. Elongation of the interatomic bonds due to applied

tensile strain in parallel to them results in relaxation of the corresponding interatomic force constants. As a consequence a red shift in the vibrational frequency takes place. Compressive stress affects bonds in the parallel direction in an opposite manner. Semiconductor devices generally consist of composite layers that possess different coefficients of thermal expansion. In addition, under normal operating conditions, local heat generation occurs. Thus during operation, thermo-mechanical coupling takes place due to lateral as well as vertical temperature gradients formed in the device which is revealed by compressive thermo-elastic stress at that local hot region. Thus the difference of phonon frequencies at operating conditions from a reference state, e.g., at room temperature, is a superposition of both temperature and stress effects. In case for non-centrosymmetrical crystal classes, electro-mechanical coupling, i.e., the converse piezoelectric effect, also contributes to the deviation of phonon frequencies between those for an operating (or electrically biased) state and a reference state.

In contrast to the Stokes peak shift method, the Stokes to anti-Stokes intensity ratio provides means to measure temperature independent of stress since this ratio solely depends on the phonon population that can be explained by Bose-Einstein statistics (under thermal equilibrium situations and within the harmonic regime). The ratio of anti-Stokes to Stokes intensities increases with temperature since sufficient thermal energy in the system excites a larger fraction of electrons to reside in their first vibrational state rather than the ground state. This results in higher probability of anti-Stokes Raman scattering to occur (refer to Fig. 5). However, in practice it is not easy to implement this method because of the typically very weak anti-Stokes signal intensity, long acquisition time, and requirement of a holographic notch filter which is of high cost and has limited

lifetime. Due to the limitation in spectral range for single scan Raman measurements, this method requires more than twice of experimental time compared to the peak shift based method as observation of both the higher and lower energy side of the excitation laser line is required.

Former work has shown that utilizing the change in linewidth of the E_2(high) phonon mode of GaN between the Raman spectra of the powered state and the pinch-off reference state (at same V_{ds} as the powered state) provides means to perform stress-independent Raman thermometry for AlGaN/GaN HEMTs under operation with the speed of the Stokes peak position measurement [52]. This method was shown to give accurate temperature estimates with values comparable to results from the Stokes to anti-Stokes intensity ratio method and three dimensional finite element simulations. The linewidth of the Raman peak for a measured phonon mode originates from the laser line (coherence length), spectrometer optics, and measured specimen (phonon damping rate). The former two contributions are relatively invariable or independent of temperature of the specimen thus taking the difference between two different states (operating state at elevated temperature vs. reference state) of the specimen cancels out those portions affecting linewidth. Then only line broadening from the crystal due to temperature rise is detectable. As mentioned above, temperature induced phonon line broadening is a consequence of increased scattering of the zone-center phonon that is investigated. Scatterings of the phonon with microstructural defects or material boundaries are rather temperature independent. In contrast, phonon-phonon scattering is strongly dependent on temperature as the phonon population increases with elevation of lattice temperature. Thus it is likely that linewidth will be rather insensitive to moderate levels of stress when

the lattice temperature is fixed. This is confirmed by experiments displayed in Fig. 8. However, for applications such as AlGaN/GaN HEMTs where piezoelectric materials are involved and large internal electric fields occur under operating conditions, a non-negligible electrical portion contributes to the line broadening as well. Thus in similar cases, appropriate choice of the reference state that will be compared to the operating state is crucial for obtaining correct temperature results. In [52] the pinch-off state was employed instead of an unbiased state to take into account of this electrical effect on the phonon linewidth.

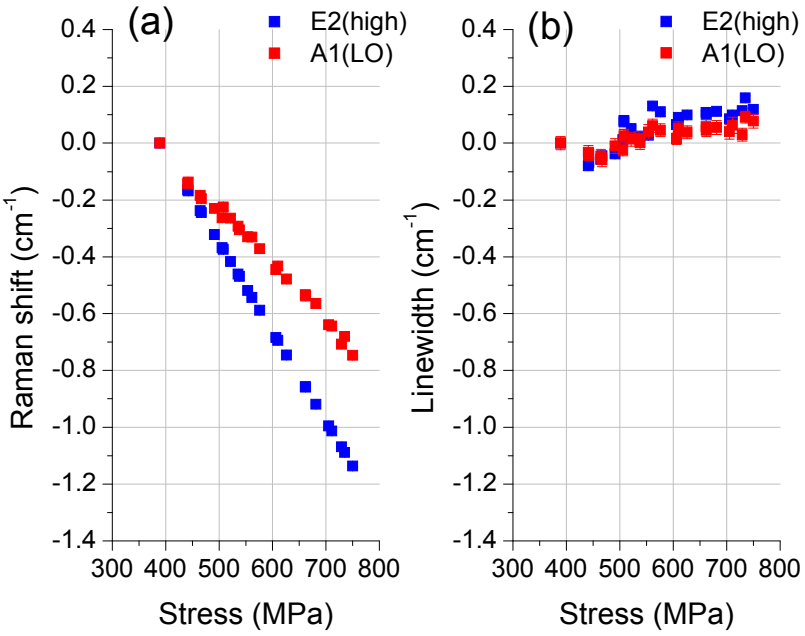

Fig. 8. (a) Shift in Stokes Raman peak position and (b) linewidth of the E_2(high) and A_1(LO) phonon mode of GaN due to application of biaxial tensile stress. Measurements in were taken at room temperature (298 K) by bending a GaN/6H-SiC template.

Utilizing shifts in frequencies of both the E_2(high) and A_1(LO) modes between the

operating (powered) state and the reference pinch-off state offers means to assess operational thermo-elastic stress and temperature simultaneously provided that the evolved stress is biaxial in the c-plane of GaN [53]. This is feasible since there are two factors of interest or 'unknowns' (temperature and stress) that contribute to shifts in two phonon modes that are measurable using Raman spectroscopy.

The temperature dependence of first-order Raman scattering of hexagonal GaN was investigated by conducting Raman measurements on single crystalline GaN films grown on sapphire substrates [49]. Down-shifts of phonon frequency and broadening accompanied by temperature rise was observed for five Raman active phonon modes: E_2(high), A_1(LO), A_1(TO), E_1(LO), and E_1(TO). These phenomena were explained by adding up the contributions from thermal expansion, three- and four-phonon decay processes. A similar study was conducted on undoped single crystalline bulk AlN where the temperature dependence of the E_2(high) and A_1(LO) phonon modes were discussed [54]. The measurement of operating temperature of AlGaN/GaN HEMTs using Raman spectroscopy was first performed in [51] utilizing the temperature dependent E_2(high) phonon frequency shift. Raman temperature measurements utilizing ultraviolet and visible laser excitations on operating AlGaN/GaN HEMTs based on the E_2(high) phonon frequency or peak position shift were conducted to reveal through-thickness variation of temperature in the device [55]. The origin of the Raman signals (or probing volume) detected is based on the laser penetration depth in the material. While GaN is transparent to visible lasers with sub-band gap photonic energy, laser light absorption takes place at the incident surface of GaN when UV lasers are utilized as excitation sources. Thus differing the excitation laser light frequency allows through thickness thermal analysis of

the specimen. However, one should take cautions when conducting such UV Raman measurements on electrically biased devices since the incident laser light can significantly alter the electrical response of the device due to generating electron-hole pairs in the conductive channel. It was shown that peak shift based Raman temperature measurement on operating AlGaN/GaN HEMTs result in an under-prediction of temperature due to complex stresses which arise during device operation from both the thermo-elastic and inverse piezoelectric effects. In accord with this, a Raman technique capable of removing errors in AlGaN/GaN HEMT thermometry arising from the stress dependency of the Raman peak position shift was developed [52]. The validity of this method was confirmed by comparing results with both finite element simulation and temperatures deduced from the Raman thermometry method using the Stokes to anti-Stokes intensity ratio. Electro-thermal simulations on AlGaN/GaN HEMTs grown on different substrates (SiC, Si, and sapphire) were performed and compared with experimental I-V characteristics as well as Raman temperature measurement results [19]. Difference in current saturation levels for each structure was explained in terms of the self-heating effect.

2.2 Photoluminescence Spectroscopy

2.2.1 Theory

Photoluminescence is an optical emission effect caused by the excitation and subsequent relaxation of electrons within a material brought about by the absorption of photons. Photoexcitation promotes electrons to permissible excited states. These

electrons release the excess energy as they thermalize to their equilibrium state either by emission of photons, i.e., radiative processes (fluorescence, phosphorescence), or nonradiative processes (vibrational relaxation, internal/external conversion, intersystem crossing). The favored deactivation route to the equilibrium or ground state is the one that minimizes the lifetime of the excited state. The energy of the emitted light corresponds to the difference in energy between the excited state and the equilibrium state involved in the electronic energy transitions.

Photoluminescence processes in semiconductors are illustrated in Fig. 9, which plots the E-k diagrams for direct band gap semiconductors and indirect band gap semiconductors. Here E and k are the kinetic energy and wave vector of the electron or hole, respectively. When a semiconductor is illuminated with light, electron-hole pairs are created as photons are absorbed. As the electron-hole pairs undergo recombination, emission of photons takes place with a random direction phase, and polarization. The most common radiative transition in semiconductors is between states in the conduction and valence bands, where this energy of interband transition is known as the band gap energy. Here it is assumed excitation is carried out with a photonic energy beyond the band gap of the material. Thus photoluminescence spectroscopy gives a direct measure of the band gap of semiconductors. It should be noted that the phonon energy (~0.01 eV) is much smaller than the energy of emitted photons in the photoluminescence process. Thus rough estimation of the band gap of indirect band gap semiconductors is also possible. Special features of photoluminescence spectroscopy on semiconductors other than band gap determination are impurity level/defect detection, recombination mechanism analysis, and material quality measurement, etc.

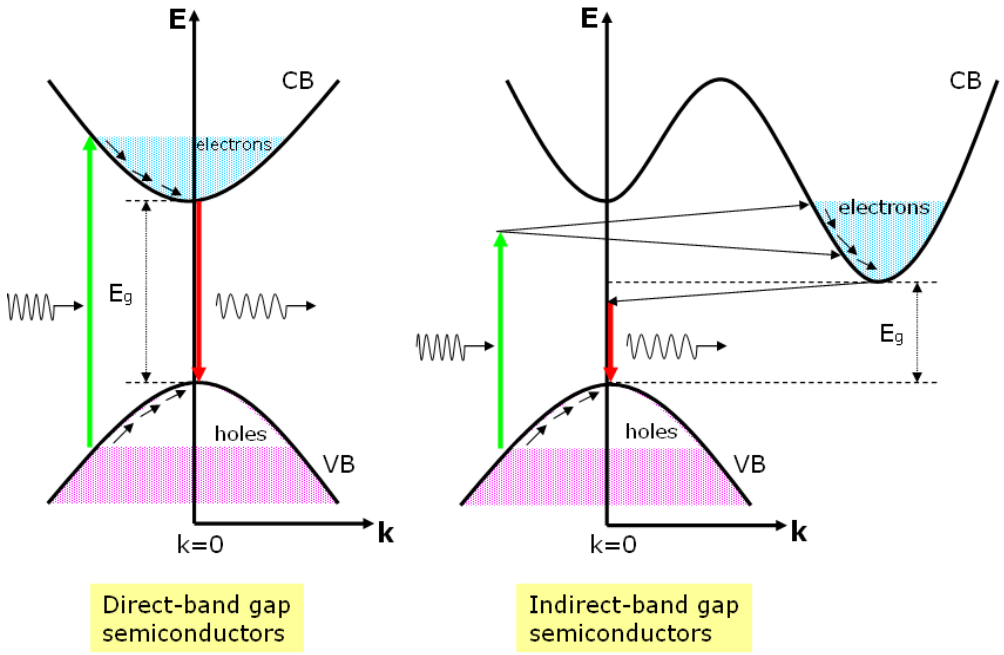

Fig. 9. Photoluminescence processes in direct band gap and indirect band gap semiconductors. Electrons and holes created by absorption of photons are represented as the shaded states near the bottom of the conduction band and the empty states near the top of the valence band, respectively. Photon absorption and emission processes are represented by vertical arrows on the E-k diagrams according to energy and momentum conservation since momentum of the photon is negligible compared to that of the electron. Transitions within the conduction and valence bands represent rapid thermalization processes of the excited electrons and holes via phonon emission. For indirect band gap semiconductors, photon absorption process must be assisted with either phonon absorption or emission and photon emission requires phonon emission to conserve momentum.

2.2.2 Stress Measurement using PL

PL is another optical characterization technique that measures the variation of strain level in GaN since the energy band gap is strongly sensitive to the state of strain. Alteration of interatomic distances as well as relative positions of atoms by mechanical

strain alters the band structure of semiconductors and changes the band gap energy. In fact, strain engineering in semiconductor thin films has been employed to obtain desired physical and electronic properties. Biaxial tensile strain in the basal plane of GaN decreases the energy band gap of GaN and compressive strain increases it. It was shown by experiments followed by ab-initio calculation that for wurtzite GaN, under biaxial tensile stress, the valence-band maximum (VBM) and the conduction-band minimum (CBM) offset to lower energies while the VBM offset is smaller than the CBM offset resulting in a decrease in the energy band gap [46]. The effect of applied stress to the room temperature PL peak of GaN epifilms is plotted in Fig. 10. A brief overview of past relevant publications was given in section 2.1.2 and will be further introduced in Chapter 3.

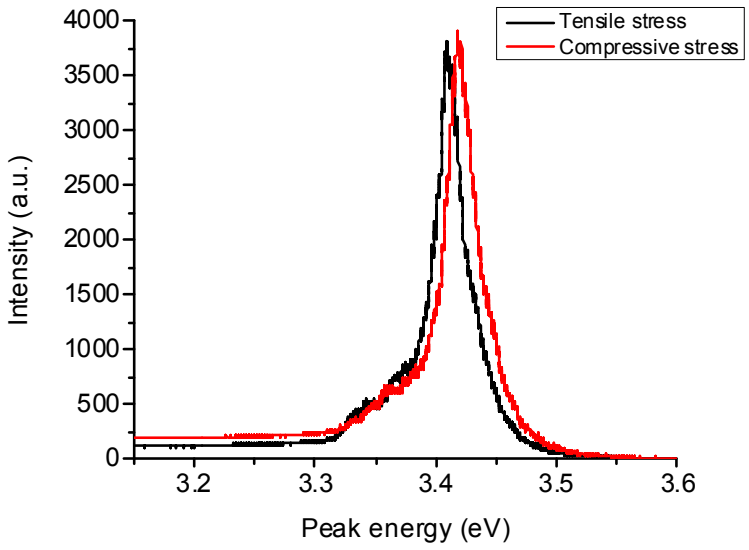

Fig. 10. Room temperature PL spectra for GaN epifilms under tensile (GaN/6H-SiC) and compressive (GaN/4H-SiC) stress. The choice of substrate material as well as processing technology, details of buffer transition layer affects the residual stress in the GaN layer. Tensile stress induces a red shift in the PL peak position from a 'stress free' value (will be discussed in detail in Chapter 3).

CHAPTER 3

DEVELOPMENT OF OPTICAL STRESS METROLOGY FOR THIN GAN EPI-LAYERS

3.1 Overview and Motivation

Stress in GaN is not directly measured by Raman and PL spectroscopy. Rather, measured strain is translated into stress and this requires an ideal strain-free reference and knowledge of the elastic properties of the material under consideration, i.e., GaN. The degree of biaxial stress in GaN is known to have a linear relationship with both the E_2(high) phonon frequency and the luminescent band gap shift at a given temperature (for moderate stress ranges, e.g., from -1.5 to 0.5 GPa [17]). With Raman and PL measurements, an accurate assessment of the slope of strain or stress versus frequency or energy shift is feasible but the absolute magnitude of strain or stress depends on the choice of the strain-free reference. Unfortunately, the strain-free E_2(high) mode frequency and energy band gap of GaN at room temperature are reported in literature over a wide range [11], [15], [16], [17]. This variation may stem from difference in the choice of GaN samples that would represent a strain free perfect GaN crystal, details of the initial spectrometer calibration, and excitation laser power conditions utilized which have potential to locally heat the sample, especially for PL measurements because the pump wavelength is strongly absorbed. Stress is estimated by utilizing the slope of biaxial stress versus frequency or energy shift and these stress conversion factors solely depend on the choice of elastic stiffness constants which suffer from a large scatter in

published values [12], [16], [17], [28], [29]. Therefore, studies attempting to correlate biaxial stress with Raman and/or PL measurements show contradictory results. Therefore to apply these stress measurement techniques to actual devices, it is highly desirable to use suitable parameters and accurate stress-strain relations to correlate a known stress state (i.e., uniaxial, biaxial, hydrostatic, etc.) to phonon frequency and/or band gap energy shift.

A unified framework incorporating x-ray diffraction (XRD), Raman spectroscopy, and PL was conducted to obtain the E_2(high) Raman peak and the PL band-edge emission peak representing zero-strain reference values of fully relaxed GaN as well as Raman and PL biaxial stress conversion factors. The relationships between optical phonon frequencies, band gap with biaxial stress were precisely determined.

3.2 Experimental Methodology

3.2.1 Quantification of film stress in GaN templates

To determine the relationships between optical phonon frequencies, band gap energy, and biaxial stresses in the c-plane of unintentionally doped GaN films, a range of commercial MOCVD and HVPE GaN films (bare epi) were explored. The films had a nominal thickness in the range of 0.5-5 μm and were grown on different substrates (two GaN/sapphire, one GaN/6H-SiC, one GaN/4H-SiC, and two GaN/Si templates) with epitaxial relationships described in Table. 1. The samples were characterized using x-ray

diffraction (XRD), micro-Raman spectroscopy, and micro-photoluminescence (PL). Representative samples are displayed in Fig. 11. In Table. 1, lattice mismatch is defined as

$$(d_{GaN} - d_{substrate}) / d_{substrate} \times 100(\%) \quad (1)$$

where d_{GaN} and $d_{substrate}$ are the inter-planar spacings of the GaN film and substrate along the in-plane direction, respectively. Details of calculations are shown in [56].

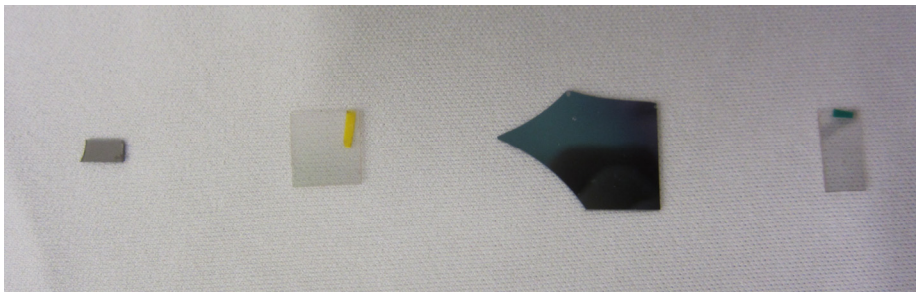

Fig. 11. Representative GaN samples characterized via XRD, Raman spectroscopy, and photoluminescence. GaN/Sapphire, GaN/4H-SiC, Si_3N_4/GaN/Si, and GaN/6H-SiC samples displayed from the left side.

Table 1. Room temperature properties of substrate materials for epitaxy of GaN

Material	Crystal structure	Epitaxial relationship	In-plane direction GaN//Substrate	Lattice constant (Å)		Lattice mismatch (%)[a]	Thermal expansion coefficient (10^{-6} K^{-1}) at 300 K	
				a	c		∥a-axis	∥c-axis
GaN	Wurtzite	-	-	3.1878[b]	5.1850[b]	-	4.33[c]	3.87c
AlN	Wurtzite	(0001)/(0001)	$[10\bar{1}0]//[\bar{1}0\bar{1}0]$	3.1106[d]	4.9795[d]	2.41	4.35[e]	3.48[e]
Sapphire	Rhombohedral	(0001)/(0001)	$[2\bar{1}\bar{1}0]//[01\bar{1}0]$	4.7650[d*]	12.9820[d]	-22.65	6.25[f]	7.05[f]
6H-SiC	Hexagonal	(0001)/(0001)	$[10\bar{1}0]//[10\bar{1}0]$	3.0806[d]	15.1173[d]	3.48	3.36[g]	3.25[g]
4H-SiC	Hexagonal	(0001)/(0001)	$[11\bar{2}0]//[11\bar{2}0]$	3.0730[d]	10.0530[d]	3.50	3.30[g]	3.16[g]
Si	Diamond	(0001)/(111)	$[11\bar{2}0]//[1\bar{1}0]$	5.4310[d*]		-16.99	2.616[d]	

[a]Reference [56].
[b]Reference [57].
[c]Reference [58].
[d]Reference [59].
[e]Reference [60].
[f]Reference [61].
[g]Reference [62].
[*] Due to rotation of GaN to substrate unit cells, $4.7589\times\sqrt{3}/2$ and $5.4309\times\sqrt{2}/2$ are the relevant lattice parameters respectively.

X-ray diffraction (XRD) measurements were carried out to measure lattice constants of the GaN samples using a PANalytical X'Pert Pro system equipped with a Cu Kα x-ray source. The c-axis lattice constants were measured by examining the symmetric reflections from the (0002) and (0004) planes. Then this together with the asymmetric reflections from the $(10\bar{1}1)$ and $(20\bar{2}2)$ planes, the a-axis lattice constants were calculated. The strains along the a and c axes were given by

$$\varepsilon_a = (a - a_0)/a_0 \qquad (2)$$
$$\varepsilon_c = (c - c_0)/c_0$$

where a and c are the lattice spacing along the a and c axes and a_0 and c_0 are the relaxed, unstrained true lattice constants of pure GaN which must be known a priori. Bulk GaN crystals grown under high pressure have been utilized to represent strain-free GaN for a number of studies (a_0=3.1880 Å and c_0=5.18561 Å [11], a_0=3.1890 Å and c_0=5.1864 Å [63], a_0=3.1912 Å [64]). However such bulk crystals may contain high concentrations of oxygen (unintentionally doped) affecting lattice parameters (hydrostatic stress-expansion) thus they are inappropriate as strain-free reference samples [65]. Also residual strain can build up in bulk GaN crystals as the Ga-face and N-face have different growth rates and different dopant incorporation rates [66]. Instead, relaxed lattice constants (a_0=3.1878 Å and c_0=5.1850 Å) estimated from homoepitaxial layers grown on bulk GaN [57], [65] were suggested to be representative of the true lattice parameters of a hypothetical perfect crystal of GaN. Lattice parameters (a_0=3.1876 Å and c_0=5.1846 Å) of bulk crystals grown from solutions containing Mg with low Mg and O concentrations below 10^{-19} cm^{-3} were shown to approach these ideal lattice constants [65]. Therefore, in this study the true lattice constant for pure GaN was assumed to be a_0=3.1878 Å and c_0=5.1850 Å.

To relate strain to stress, the elastic constants of GaN must be known. A critical comparison of elastic stiffness constants as well as related moduli and coefficients of GaN in the literature was reported by comparing values determined by measurements and ab initio calculations [45]. Elastic stiffness constants in [67] (C_{11}=390±15 GPa, C_{33}=398±20 GPa, C_{44}=105±10 GPa, C_{66}=123±10 GPa, C_{12}=145±20 GPa, and C_{13}=106±20 GPa) obtained by Brillouin scattering measurements were employed as the elastic constants of wurtzite GaN. In case of wurtzite GaN films under homogeneous biaxial stress in the c-plane (σ_a=σ_b, σ_c=0), the biaxial relaxation coefficient R^B and the

Poisson ratio v are expressed in terms of elastic stiffness coefficients as follows.

$$\nu = \frac{C_{13}}{C_{11} + C_{12}} \tag{3}$$

$$R^B = -\frac{\varepsilon_c}{\varepsilon_a} = \frac{2C_{13}}{C_{33}} \tag{4}$$

The biaxial stress is related to the in-plane strain ε_a by

$$\sigma_a = Y\varepsilon_a \tag{5}$$

where the biaxial modulus Y is defined as

$$Y = C_{11} + C_{12} - 2C_{13}^2 / C_{33} \tag{6}$$

The relationship between the in-plane biaxial stress and the c-axis strain can be easily derived as

$$\sigma_a = -(Y / R^B)\varepsilon_c \tag{7}$$

In general, thin films having a wurtzite crystal structure exhibit an anisotropic behavior. Fortunately, however, the relation $C_{11}+C_{12}\approx C_{13}+C_{33}$ holds well for wurtzite GaN [46], [45], [68]. This renders a quasi-cubic or isotropic elastic assumption valid for GaN [46], [43] whereas this relation does not hold for other wurtzite structured nitrides such as AlN and InN [69]. For elastically isotropic materials under homogeneous biaxial

stress in the c-plane, the Poisson ratio ν along [0001] is related to the biaxial relaxation coefficient or strain ratio R^B by

$$R^B = -\frac{\varepsilon_c}{\varepsilon_a} = \frac{2\nu}{1-\nu} \tag{8}$$

The biaxial stress is expressed in terms of the Poisson ratio ν, Young's modulus $\hat{E}$ (we use this notation to distinguish Young's modulus from the luminescent band gap energy E), in-plane strain ε_a, and out of plane strain ε_c by

$$\sigma_a = -\frac{1}{2\nu}\hat{E}\varepsilon_c = \frac{1}{1-\nu}\hat{E}\varepsilon_a \tag{9}$$

Since the elastically isotropic approximation holds for wurtzite GaN under the in-plane biaxial stress case under consideration, the biaxial modulus Y and Young's modulus $\hat{E}$ are related as

$$\hat{E} = \frac{2\nu}{R^B}Y = \frac{C_{33}Y}{C_{11}+C_{12}} \tag{10}$$

The elastic stiffness constants employed in this study yield R^B=0.533±0.10, ν=0.198±0.039 (0.210±0.032 from (8)), Y=479±33 GPa, and $\hat{E}$=356±46 GPa.

3.2.2 Experimental setup

Micro-Raman spectroscopy and PL measurements were performed through the use of Horiba Jobin Yvon LabRAM HR800 (Fig. 12). A 532 nm diode-pumped solid-state laser and a 325 nm He-Cd laser were used as excitation sources for Raman and PL measurements, respectively. The spectrometer had a focal length of 800 mm and equipped with a back-illuminated-UV coated liquid N_2 cooled 2048×13.5 μm^2 pixels charged-coupled device (CCD) detector. A 1800 groove/mm diffraction grating was used and the confocal hole size was adjusted to 100 μm. This setup was established to obtain high enough spectral resolution suited for stress measurements while having a reasonable acquisition time and spectral range for each measurement. Raman measurements using 532 nm excitation had a spectral resolution of 0.83 cm^{-1}/pixel of CCD defined following the rule that it takes 3 pixels minimum to define a peak. For PL measurements utilizing the 325 nm laser, a spectral resolution of 4.75 cm^{-1}/pixel (5.89×10^{-4} eV/pixel) of CCD was obtained. It should be noted that the typical peak widths were 2~3 cm^{-1} or larger for the E_2(high) modes and higher resolution using our 2400 groove/mm grating did not improve seeing a sub-wavenumber shift. Software curve fitting algorithms provide sub pixel peak position resolution thus the precision to peak shifting is more than an order higher than the resolution mechanically limited by the spectrometer. Experiments were carried out with the laser light perpendicular to the basal plane of GaN in a 180° backscattering configuration and un-polarized detection. The E_2(high) mode was investigated among the Raman active modes observable for this configuration, namely, two E_2(TO) and the A_1(LO) modes [9]. The 532 nm and 325 nm laser powers incident on

the GaN samples were adjusted via neutral density filters to ~25.2 mW (except for GaN/Si samples where 0.2 mW was used to prevent substrate heating) and ~0.003 mW, respectively. The sub-band gap laser wavelength (532 nm) used for Raman measurements prevents localized heating of GaN by laser light absorption. The 325 nm laser power used for PL measurements was determined by taking into account of minimized local heating, reasonable acquisition time, and prevention of material damage. A 50X LWD objective (NA=0.5) was used for Raman measurements. 40X and 39X NUV objectives (NA=0.5) were employed to focus the laser on the sample surface and collect the PL signatures. The theoretical diffraction limited laser focused spot sizes (diameter) were 1.3 μm and 0.79 μm for the Raman and PL measurements, respectively using the relation $d = 1.22\lambda / NA$ where d is the spot diameter, λ is the laser wavelength, and NA is the numerical aperture. Before conducting Raman and PL measurements, the system was calibrated at 25°C with a 4H-SiC piece to 776.599 cm^{-1} which was equivalent to 520.46 cm^{-1} for high quality single crystal silicon. Si is a common Raman calibration source especially good for GaN investigation utilizing a 488 nm laser. However, for lasers used in this study (532 and 325 nm), acquiring a Si Raman peak with a reasonable intensity or signal to noise ratio at a reasonable acquisition time is not easy when laser powers are properly adjusted not to induce localized heating in Si. Therefore 4H-SiC together with a plasma line of a fluorescent light source was used instead of Si. The long focal length offers higher spectral resolution, but also renders the spectrometer more susceptible to thermal drift. To correct for the drift, the plasma lines of the external fluorescence source was employed as an additional reference during sample measurement. The shift from its initial peak value (482.215±0.005 cm^{-1}) in the Raman spectra provided means to track the drift (systematic

error) of the spectrometer itself in real time with each measurement which allows a much more time efficient measurement compared to the standard method of calibrating the spectrometer using Si before and after every sample measurement. In order to determine the peak position and full width at half maximum (FWHM), Raman and PL spectra were fitted using a linear combination of Gaussian–Lorentzian line-shapes. The spectral range for PL measurement was 3.15-3.6 eV. In order to determine the peak position of the near band-edge peak at room temperature, the PL peaks for each sample were resolved into two peaks, namely, the principal line (zero-phonon line) and its phonon replica line. The energy spacings between two peaks were close to a predicted value of 53.5 meV at 298 K estimated from the temperature dependence of the energy spacing between the 1LO phonon sideband and its principal line [70]. Best estimates and uncertainties (95% confidence bounds) were calculated based on at least 20 measurements for each sample or condition. Data acquisition times were adjusted to obtain consistent Raman (~8000) and PL peak (~4000) intensity counts. Samples were measured at room temperature while mounted on a heating stage (INSTEC HCC324S) maintained at 25°C (±0.06°C) to isolate stress measurement results from temperature effects, namely, shift in peak position and line-broadening.

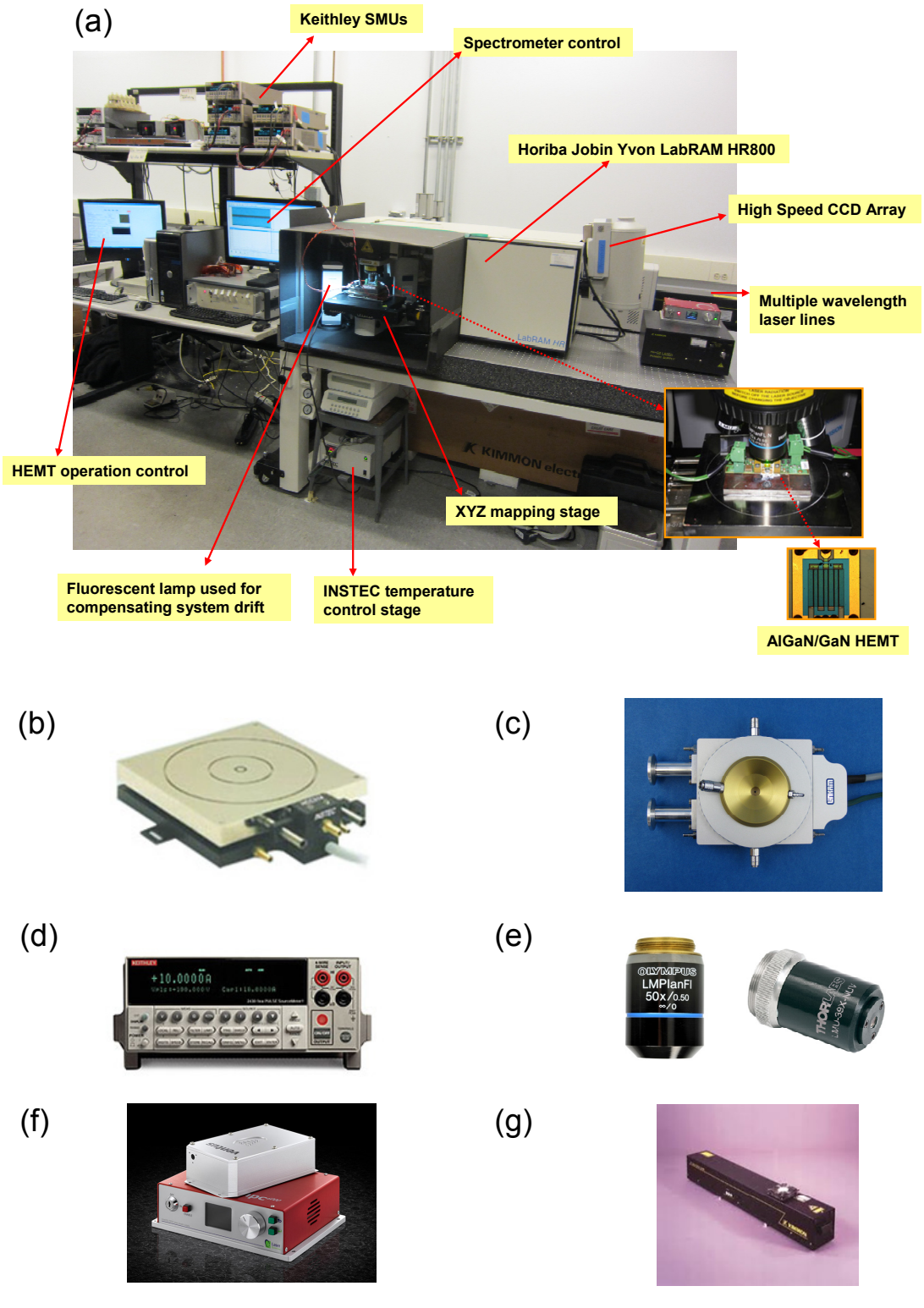

Fig. 12. Schematic of experimental apparatus including spectrometer and peripherals used for characterizing AlGaN/GaN HEMTs. (a) Overall test station. (b) INSTEC HCC314S thermal chuck system used to maintain measured specimen's temperature. (c) Linkam TS1200 temperature controlled stage implemented to acquire the calibration of a

material's Raman response to temperature. (d) Keithley source meter units capable of DC / pulse operation. Models 2400, 2410, 2420, 2425, 2430, 2602A selectively used for different measurement purposes (high power / high voltage / pulse). (e) Olympus LMPlanFl 50x objective (50X, NA=0.50, WD=10.6 mm) used for visible Raman measurements (left), THORLABS LMU-39X-NUV objective (39X, NA=0.50, WD=2 mm) used for UV laser spectroscopy measurements (right). (f) Ventus LP 532nm, 100 mW laser used for visible Raman measurements. (g) Kimmon IK5551R-F Dual Wavelength HeCd Laser (15 mW at 325 nm, 60 mW at 442 nm) used for photoluminescence and UV Raman measurements. Images (b)-(g) adapted from each vendor's website.

3.3 Results and Discussion

3.3.1 XRD measurement

The relationship between and lattice constants of the GaN epifilms are displayed in Fig. 13. The linear relationship between the lattice parameters means the epitaxial layers are elastically deformed by the built-in stress. Also shown are the lattice parameters of a 350 μm thick free-standing GaN sample. Its lattice parameters are indeed larger than the assumed strain-free lattice constants [57], [65] showing the effect of unintentional doping. It is shown in Fig. 14 that biaxial stress is dominant in the GaN films since a nearly constant value of $\varepsilon_c/\varepsilon_a$ (the slope of the plot) is observed. Thus hydrostatic stress introduced by the presence of point defects [43] in addition to biaxial stress induced through the substrate is not considered in the following stress analysis.

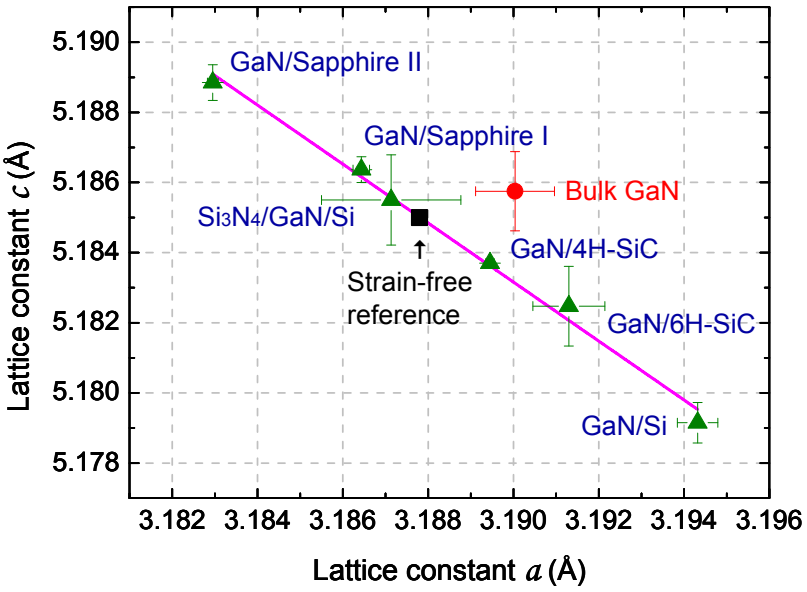

Fig. 13. Lattice constant *a* vs. lattice constant *c*. The triangles indicate the lattice constants of measured GaN templates. The solid line is the fitting result. The circle and square correspond to a GaN substrate and strain-free ideal lattice constants, respectively.

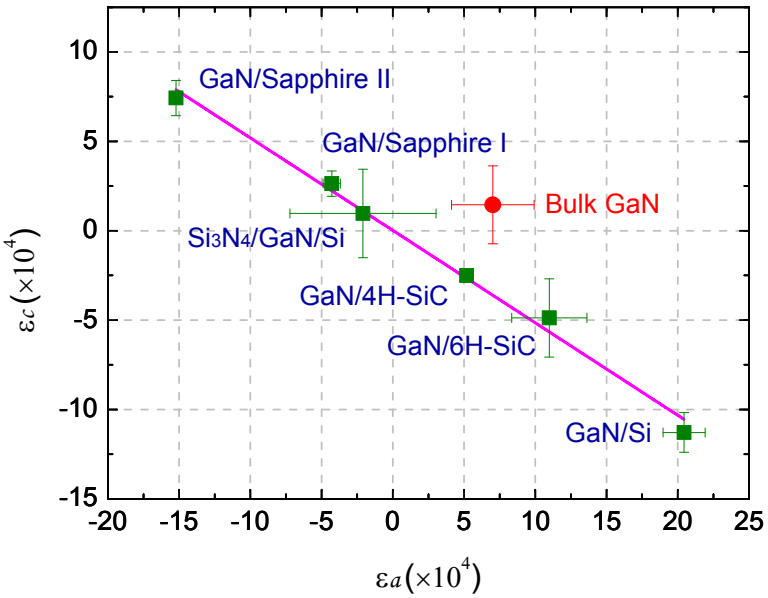

Fig. 14. In-plane strain vs. out-of-plane strain. The squares correspond to the lattice constants of measured GaN templates. The solid line is the fitting result. The circle is indicative of a bulk GaN substrate.

As mentioned above, strain-free lattice constants were assumed to be a_0=3.1878 Å and c_0=5.1850 Å. Strain perpendicular and parallel to the c-axis were obtained using the lattice parameters of the GaN epilayers measured by XRD. The biaxial relaxation coefficient or strain ratio obtained from the slope of the plot in Fig. 14 or (8) is R^B=0.519±0.06 which is close to the theoretically predicted value of R^B=0.533±0.104 according to (4). The experimental Poisson's ratio is determined by (8) to be ν=0.203±0.018. This value agrees well with the theoretical value ν=0.198±0.039 predicted from (3) using the elastic stiffness constants employed in this study as well as a typically accepted value in literature of ν=0.205 [68], [69]. The residual stresses in the GaN epifilms calculated by (4)-(7) are displayed in Fig. 15. Here we adopt the convention that a positive value corresponds to tensile stress. The average of these stress values were assigned to represent the residual stress in each GaN epifilm and were used to extract the biaxial stress conversion factors and estimate the E_2(high) phonon frequency and band-edge peak corresponding to the strain-free case at room temperature. These theoretically determined stress values agree well with stresses calculated from (6) and (8)-(10) which confirms the validity of the XRD experiments and chosen structural parameters. The stress uncertainties in each GaN epifilm were included in the ensuing statistical (error propagation) analysis for calculating the final uncertainties (95% confidence intervals) in the biaxial stress conversion factors and strain-free reference values.

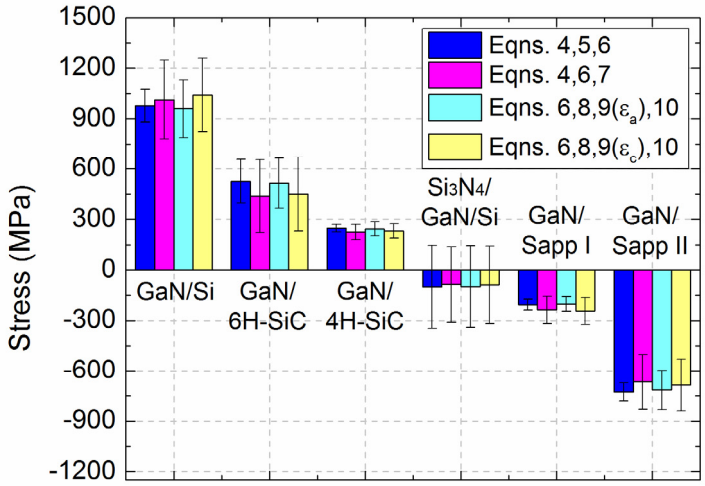

Fig. 15. Biaxial stress in the basal plane of measured GaN epifilms. Stress calculations were performed based on equations listed in the legend. Average of stress values obtained from (4), (5), (6), and (7) (first and second columns for each template) were used to derive the stress conversion coefficients.

The magnitude of the residual biaxial stress in an epitaxial GaN layer depends on type of substrate, thickness of buffer layer and epitaxial film, growth temperature, generation of misfit dislocations, material relaxation by cracking, etc. The different magnitude of biaxial stress in GaN epilayers (Fig. 15) can be explained by referring to the material parameters in Table. 1. For the GaN/Si sample, the lattice constant of GaN is smaller than that of Si where the atomic spacing on the (111) plane is 3.84 Å (-16.99% lattice mismatch). The thermal expansion coefficient of GaN parallel to the a-axis is larger than that of Si. Thus the lattice of GaN would contract more than that of Si during post-growth cooling. Both of these mismatches lead to a high tensile stress in the GaN epilayer although a buffer layer is implemented. For the sample GaN/6H-SiC, both the lattice

mismatch (+3.5%) and thermal expansion coefficient discrepancy are relatively small compared to GaN/Si. The lattice constant of GaN is slightly larger than that of SiC which is expected to induce a compressive stress in GaN. On the other hand, thermal expansion coefficient of GaN is slightly larger than that of SiC. A tensile residual stress is built in the GaN layer at room temperature when the residual thermal stress built in the GaN layer after cooling from deposition temperature to room temperature over-compensates the influence of lattice mismatch. In case of not implementing a buffer layer in the structure, a relatively large stress value can remain in the epitaxial GaN layer. The lattice mismatch between GaN and sapphire is quite large (-22.65%). However, the sapphire thermal expansion coefficient is much larger than that of GaN which is responsible for the highly compressive residual stress in GaN at room temperature. The residual stress induced by lattice constant mismatch relaxes within less than several nanometers of the film thickness during growth [12], [42]. For all cases measured here (except bulk GaN), the substrate-induced strain would virtually reside in the GaN epitaxial layer (and the buffer layer) since the GaN layer was much thinner than its substrate. The low level of residual stress in the Si3N4/GaN/Si sample exemplifies the significance of both passivation and buffer layers to the residual stress in a GaN epilayer.

3.3.2 Raman measurement

Fig. 16 shows the correlation between room temperature Raman spectra and biaxial stresses of the measured samples. As expected, the E_2(high) phonon mode positions are stress dependent which are mainly caused by the substrate type and growth process. The

linear relationship between the frequency shift of the E_2(high) phonon mode and in-plane biaxial stress σ_a in GaN can be expressed as

$$\omega - \omega_0 = K_{RS}^{E2(high)} \sigma_a \tag{11}$$

where ω is the measured E_2(high) phonon frequency, ω_0 is the strain-free E_2(high) mode frequency, and $K_{RS}^{E2(high)}$ is the Raman biaxial stress conversion factor.

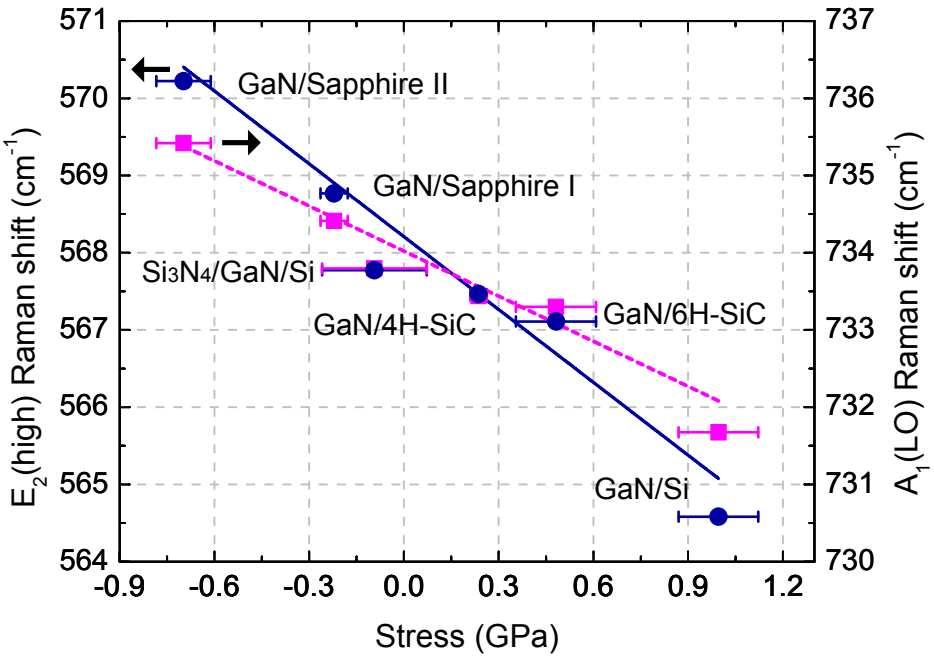

Fig. 16. Room temperature Raman shifts vs. corresponding residual stresses obtained by XRD measurements. Both E_2(high) and A_1(LO) mode relations are displayed as blue circles and pink squares, respectively. The solid line is the fitting of E_2(high) frequencies whereas the dashed line is the result of A_1(LO) frequencies.

A strain-free reference sample plays a crucial role in the determination of the

magnitude of biaxial stress in the GaN layers by Raman spectroscopy. Reference samples used in literature vary, for example, undoped 300 μm thick GaN grown on a sapphire substrate by chloride-hydride vapor phase epitaxy [11], 25 μm thick GaN on a Si substrate [27], the edge of the surface of an undoped ~4.6 μm thick epifilm grown by metalorganic chemical vapor deposition on a sapphire substrate [42], GaN nanorods grown epitaxially on Si(111) substrates with a GaN buffer layer [71], single detached GaN nanocolumn samples on Si(111) and sapphire (0001) substrates [72], 400 μm thick free standing GaN [64], [73], and homoepitaxially grown GaN films by molecular beam epitaxy [43]. Also details of initial spectrometer calibration conditions are rarely elucidated. Therefore it is not surprising that there is a large scatter in published reference room temperature Raman E_2(high) mode peak positions. To illustrate, 566.2 cm^{-1} [43], 567.3 cm^{-1} [42], 567.5 cm^{-1} [64], [73], 567.6 cm^{-1} [14], 567.7 cm^{-1} [71], and 568 cm^{-1} [10]. The E_2(high) response of the GaN templates under study are plotted in Fig. 16 together with the corresponding biaxial stresses lying in the samples obtained from XRD measurements. The strain-free E_2(high) mode frequency ω_0=568.15±0.13 cm^{-1} and the Raman biaxial stress conversion factor $K_{RS}^{E2(high)}$=-3.09±0.41 cm^{-1}/GPa were determined from the intersection with the y-axis and the slope of the plot in Fig. 16, respectively based on the strain-free lattice parameters, elastic stiffness constants, and initial calibration conditions adopted in this study. Here the 95% confidence intervals were deduced based on error propagation form uncertainties in the optical measurements (XRD, Raman, and PL) on each template as well as adopted elastic modulus. The Raman response of the bulk GaN sample was ω=567.402±0.002 cm^{-1} which indicates expansion (not purely biaxial) relative to a hypothetical strain-free crystal or that the crystal is

chemically altered with different bond strengths where impurities are present such as oxygen. This value for bulk GaN agrees well with results (567.5 cm^{-1}) in Refs. [73] and [64] even though their initial calibration conditions were not clearly explained. The unintentional doping effect, i.e., increased free (n-type) carrier concentration, which is responsible for the dilatation is also revealed by its A_1(LO) Raman signature where a blue shift in frequency (ω=735.016±0.007 cm^{-1}) and broadening occurs with respect to the expected strain free peak. Previous work [37] has shown that biaxial stress of one GPa shifts the E_2(high) mode by 2.91 cm^{-1} through loading of a single stack (GaN/6H-SiC) using a four-point bending stage where GaN was assumed to be elastically isotropic and a Poisson's ratio of ν=0.183 and Young's modulus $\hat{E}$=388 GPa were employed. Applying the same elastic assumptions to our XRD data, the biaxial stress conversion factor resulted in $K_{RS}^{E2(high)}$=-2.91±0.23 cm^{-1}/GPa. Our value ($K_{RS}^{E2(high)}$=-3.09±0.41 cm^{-1}/GPa) also shows satisfactory agreement considering the uncertainties of the experimental results with the value ($K_{RS}^{E2(high)}$=-2.7±0.3 cm^{-1}/GPa) in [11] where identical elastic stiffness constants were adopted. Their biaxial stress conversion factor was mentioned to be reliable by comparing with ab-initio calculations [45]. Another published value for $K_{RS}^{E2(high)}$ was -2.9±0.3 cm^{-1}/GPa [74] which was later, by the same authors [75], recalculated to be -3.19 using same elastic stiffness constants employed in our study. They remeasured three GaN on Si(111) samples with various thicknesses using Raman and XRD resulting in $K_{RS}^{E2(high)}$=-2.43±0.6 cm^{-1}/GPa. Both results agree well with our biaxial stress conversion factor considering error margins. Some other reported values are -3.4±0.3 cm^{-1}/GPa [27], -4.2±0.3 cm^{-1}/GPa [43], and -4.3 cm^{-1}/GPa [64], etc. where the main reason for deviation is inconsistency in employing elastic stiffness coefficients. For

example, the elastic constants adopted in our study yields $\hat{E}$=356±46 GPa under an elastically isotropic assumption while the Young's modulus used in [43] is $\hat{E}$=290 GPa [45]. When elastic stiffness constants used in our study are applied to their data, the biaxial stress conversion factor turns out to be -2.9 cm^{-1}/GPa. In [76], the biaxial strain dependence of the E_2(high) mode was investigated using room temperature Raman and XRD measurements on GaN films MOVPE-grown on sapphire and 6H-SiC substrates. If the elastic stiffness constants used in our study are applied to their data, a biaxial conversion factor of -2.82 cm^{-1}/GPa is obtained which agrees well with our value.

Conducting a similar approach illustrated above, the relationship between biaxial stress in GaN and the A_1(LO) Raman shift was investigated and is displayed in Fig. 16. The strain free mode frequency and the Raman biaxial stress conversion factor were determined to be ω_0=733.94±0.09 cm^{-1} and $K_{RS}^{A1(LO)}$ =-2.14±0.28 cm^{-1}/GPa, respectively. Since the longitudinal optical polar phonon frequency is affected by free carrier concentration or different doping levels, a single GaN/6H-SiC template was individually tested under uniaxial bending on the basal plane with a setup using a pivot pin and press screws similar to that described in [77] to confirm the aforementioned results. The E_2(high) and A_1(LO) modes were measured simultaneously. The stress in the GaN layer was estimated from the E_2(high) mode frequency and its corresponding biaxial stress conversion factor assuming that the stress conversion factors for uniaxial and biaxial loading on the basal plane differ by a factor of 2. The relationship between stresses in the layers (0.75-1.46 GPa, uniaxial) and the A_1(LO) mode frequency shifts resulted in ω_0=733.88±0.34 cm^{-1} and $K_{RS}^{A1(LO)}$ =-1.91±0.62 cm^{-1}/GPa. The nice agreement between results from two different methods provides confidence in the analyzed results. Again the derived biaxial

stress conversion factor shows an excellent agreement with the theoretically calculated value $K_{RS}^{A1(LO)}$=-1.91 cm^{-1}/GPa using same elastic stiffness constants [45]. The value in [74] $K_{RS}^{A1(LO)}$=0.8±0.4 cm^{-1}/GPa suffers from a large imprecision and was derived using elastic stiffness constants which were pointed out that their usage should be avoided [45]. Recalculation made by authors of [74] adopting the same elastic stiffness constants used in our study resulted into $K_{RS}^{A1(LO)}$ =-0.88 cm^{-1}/GPa where they explained high unintentional n-type doping and low carrier mobility in the GaN layers investigated were responsible for obtaining this erroneous value. By remeasuring three GaN on Si(111) samples, they deduced $K_{RS}^{A1(LO)}$=-1.91±0.58 cm^{-1}/GPa [75]. As seen in Fig. 6, the A_1(LO) phonon mode corresponds to atomic oscillations along the c-axis. Tensile in-plane biaxial stress causes an increase in the a-lattice constant. In this case, the three bond lengths (L_1) nearly perpendicular to the c-axis of the four bonds in the tetrahedron shown in Fig. 17 and the α-bond angles increase as well. This effect of force constant softening is revealed by the red-shift in the E_2(high) mode frequency. Counter-intuitively, the A_1(LO) mode frequency also shifts to a lower value when tensile biaxial stress is present. This phenomena is understood based on the fact that the decrease of the c-lattice constant ensuing from tensile biaxial stress is accompanied by an increase in the bond length (L_2) along the c-axis since the bond angle β decreases [46], [45].

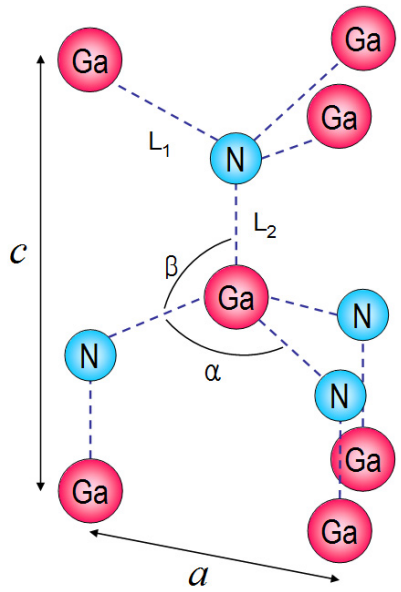

Fig. 17. Tetrahedral atomic bonding arrangement for wurtzite GaN.

3.3.3 PL measurement

Fig. 18 shows a set of room temperature PL spectra for the six samples analyzed by XRD. The residual stress in each GaN film reveals itself by the shift in the energy band gap which is represented by the PL peak position. A linear dependence of energy band gap on biaxial stress is observed.

$$E - E_0 = K_{PL}\sigma_a \tag{12}$$

Here E is the measured PL peak, E_0 is the strain-free PL peak, and K_{PL} is the PL biaxial stress conversion factor. E_0 and K_{PL} are found to be 3.4180±0.0008 eV and -

0.0176±0.0025 eV/GPa, respectively.

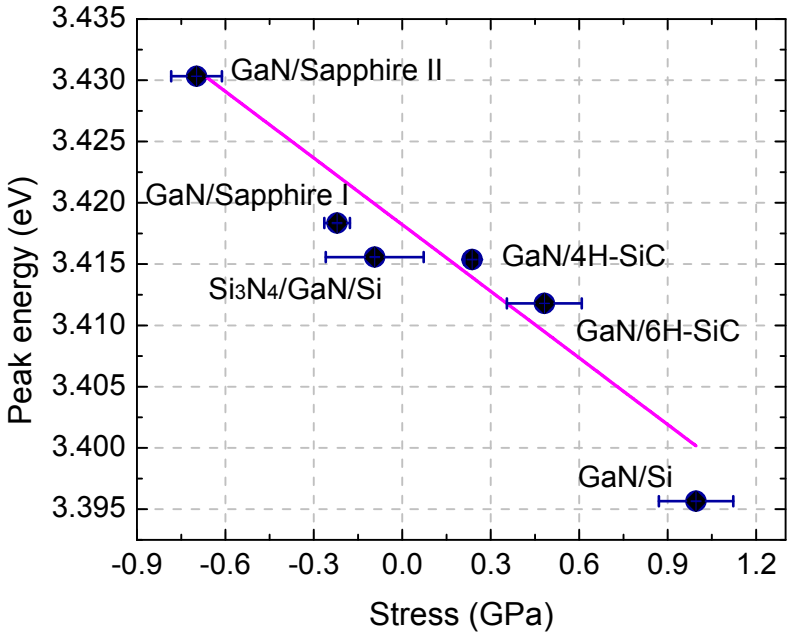

Fig. 18. Room temperature near band edge peaks of GaN templates vs. corresponding residual stresses obtained by XRD measurements. The solid line is the fitting result.

The laser power incident on the samples in our study was 0.003 mW to minimize laser induced local heating. Even at this excitation power, minimal heating was unavoidable. When E_0 and K_{PL} derived here were used with a laser power of 0.3 μW (10% of the laser power used in this work), an offset of stress of ~50 MPa (compressive) would result. However, using such a low laser power (0.3 uW) is impracticable in terms of device measurement due to prolonged accumulation time (more than 20 minutes for one measurement) which makes the experiment more susceptible to drift in measurement location. As the additional shift of the PL peak induced by local heating is rather a

constant value, this portion is included in E_0 thus using the derived E_0 and K_{PL} together with the suggested laser power (3 μW) can still be regarded as appropriate. However, one should take precautions that this condition may not hold for stress measurement on devices under voltage bias since the level of carrier induced heating would vary with bias conditions. A study [42] combining room temperature cathodoluminescence (CL) and Raman spectroscopy and another study [10] employed 3.42 eV as a strain-free reference at room temperature but this was not based on rigorous experiments. The PL biaxial stress conversion factor K_{PL}=-0.020±0.003 eV/GPa reported in [11] where XRD, Raman, and low temperature PL measurements were correlated meets with our value within the error-bar ranges. [43] and [78] report K_{PL}=-0.027±0.002 eV/GPa and K_{PL}=-0.023 eV/GPa, respectively using a Young's modulus of $\hat{E}$=290±20 GPa under isotropic assumptions relating stress determined by room temperature XRD to low temperature PL measurements. Their Young's moduli are mainly responsible for higher values of biaxial stress conversion factors. When recalculation is made using the elastic stiffness constants adopted in this study, K_{PL} for [43] becomes -0.019 eV/GPa. In [75], the authors made correction on a reported value of K_{PL}=0.0155 eV/GPa by employing the same elastic constants used in our study. As a consequence K_{PL}=0.0175 eV/GPa was obtained. K_{PL}=0.0211±0.0032 eV/GPa and E_0=3.4285 eV were reported in [44]. The discrepancy of E_0 with our corresponding value may have stem from making use of a different laser power (40 mW) from us and utilizing a different procedure to assign the stress in each of their PL measured specimens.

3.3.4 Unification and Verification

It should be noted that Raman and PL measure local stress (beam diameter of ~1 μm) whereas XRD measures stress over a larger area (0.2 mm×0.2 mm). As mentioned before, PL measures the surface of GaN (penetration depth is 80-90 nm) whereas Raman spectroscopy and XRD probe a depth of more than several microns thus measure or average strain throughout the whole of the layer [12]. A significant lateral or vertical strain gradient within the GaN layer will cause adverse effects on the correspondence of results obtained by each technique. To validate the fundamental study correlating XRD, Raman spectroscopy, and PL under the foregoing limitations, a group of high quality GaN templates were investigated. The three measurement sets in Fig. 19 show the nice correspondence of biaxial stresses measured on random high quality GaN/SiC samples utilizing the Raman E_2(high), A_1(LO) mode, and PL peak shifts. Reasonable agreement is observed which ensures the validity of the developed stress measurement method itself. The linear fit shown in Fig. 13 intersects the point corresponding to the assumed strain-free lattice constants. Moreover, the calculated dimensionless parameters such as R^B, v as well as the derived biaxial stress conversion factors show consistency with acceptable literature values obtained by theoretical calculations or experimental investigation using individual techniques or a combination of two or more of them. The obtained values for strain-free reference phonon frequencies and luminescent band gap are logically explainable. Thus stress in thin GaN epifilms under biaxial stress can be estimated with confidence by utilizing the stress conversion factors and strain free reference values for phonon frequencies and luminescent energy band gap derived in this study. A number of

AlGaN/GaN heterostructures grown on SiC and sapphire substrates were examined via XRD, Raman spectroscopy, and PL to see if the developed technique could be implemented as a tool for measuring stress in the GaN layer of AlGaN/GaN HEMTs. The Al contents of these samples were controlled to be 25-40%. Up to AlGaN thickness of ~20 nm, a reasonable agreement in the stress results from each optical technique was observed. Two representative results are displayed in Fig. 19. In addition, PL peaks for AlGaN/GaN heterostructures before and after depositing AlGaN were analyzed. For structures with larger AlGaN thickness, e.g., beyond 40 nm, a slight blue shift in the PL peak position indicating compressive stress induced in the GaN layer close to the heterointerface, for instance, ~150 MPa for 40 nm AlGaN with Al content of 40%, occured compared to the PL peak position measured prior to AlGaN deposition. However, for all cases investigated, no remarkable change in the shape of the PL spectrum was observed. The influence of band bending at the AlGaN/GaN heterointerface and existence of the 2-DEG to the GaN PL spectrum was shown to be weak and only observable at low temperatures below 120 K [79]. These arguments suggest that such effects are ruled out in case of utilizing 325 nm laser excitation (penetration depth is 80-90 nm) for PL measurements at room temperature whereas strain induced effects are still detectable. This provides confidence for applying the Raman and PL stress measurement techniques developed in this section to AlGaN/GaN HEMTs having typical AlGaN thickness of 20-25 nm and Al content of ~25%.

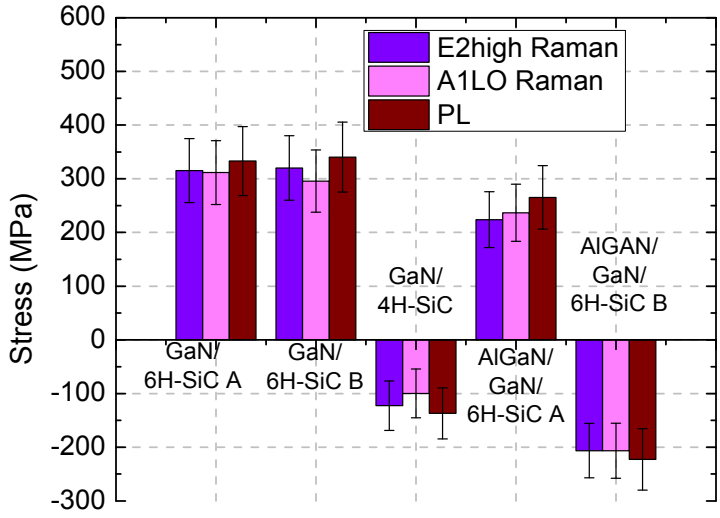

Fig. 19. Biaxial stress of arbitrary GaN samples measured by Raman spectroscopy and PL based on stress conversion parameters derived in this study.

3.4 Summary and Conclusions

From XRD measurements, biaxial residual stresses present in various GaN films were determined using lattice constants for unstrained GaN and elastic stiffness constants from literature. Room temperature Raman and PL measurements on same samples allowed correlating biaxial stress with the E_2(high) and A_1(LO) phonon frequency shifts as well as energy band gap of GaN. It has been observed that biaxial stress has a linear relationship with the Raman E_2(high), A_1(LO) mode and the luminescent band gap of GaN. This linear relationship holds for the modest and realistic strain range considered in this study. At much higher strain levels, i.e., ranges of strain of about two orders of magnitude

higher, nonlinear behavior of change in band gap energy with strain as well as structural phase transition is predicted by density functional theory simulations [80]. Derived Raman and PL biaxial stress conversion factors ($K_{RS}^{E2(high)}$ =-3.09±0.41 cm^{-1}/GPa, $K_{RS}^{A1(LO)}$ =-2.14±0.28 cm^{-1}/GPa, K_{PL} =-0.0176±0.0025 eV) showed consistency with reliable values reported in literature. Strain-free reference E_2(high) and A_1(LO) phonon frequencies as well as luminescent band gap ($\omega_{0,E2(high)}$ =568.15±0.13 cm^{-1}, $\omega_{0,A1(LO)}$ =733.94±0.09 cm^{-1}, E_0 =3.4180±0.0008 eV) were obtained under explicit initial spectrometer calibration conditions (4H-SiC, 776.599 cm^{-1}) and assumptions for elastic behavior of the GaN crystal. Based on this framework presented in this study, Raman spectroscopy and PL can provide efficient means of process feedback in terms of stress monitoring between fabrication steps in the test and development stage of GaN devices.

CHAPTER 4

ANALYSIS OF THE RESIDUAL STRESS DISTRIBUTION IN ALGAN/GAN HEMTS

4.1 Overview and Approach

A comparative analysis of the residual stress distributions across the conductive channel of Ga-face AlGaN/GaN high electron mobility transistors (HEMT) is presented. Stress was measured by means of micro-Raman spectroscopy and micro-photoluminescence (PL). The shift in the E_2(high) phonon mode frequency and the near band-edge emission peak were utilized to extract stress information for each optical technique. Raman measurements probed the volume average of the stress through the GaN layer whereas the stress near the GaN surface (AlGaN/GaN heterointerface) was acquired via PL. By combining Raman, PL, and x-ray diffraction (XRD), a self-consistent method was developed to accurately determine the variation in magnitude of stress throughout the thickness of the GaN layer. Based on this framework, it is observed in AlGaN/GaN HEMTs that the residual stress of GaN near the heterointerface exhibits a tensile shift compared to the bulk average value close to the gate and ohmic electrodes. Across the conductive channel, the bulk average stress and the stress near this interface remain nearly identical showing little evidence of a vertical gradient. It is expected that the induced tensile strain at the drain side gate edge will have an impact on device reliability by contributing to the elastic energy built in the AlGaN barrier in addition to

the inverse piezoelectric contribution at operating conditions which may lead to formation of crystallographic defects.

4.2 Motivation

Passivation and metallization structures can also impose strain in the AlGaN layer in AlGaN/GaN HEMTs. It has been shown that deposition and annealing of the ohmic contacts can induce tensile strain in the AlGaN layer [81]. Stress induced by the gate metal film which forms a Schottky contact can have an impact on device performance and reliability. It has been reported for MOSFETs that there exists stress induced by the gate metal electrode which acts as a controlling factor for device performance [82] and for GaAs MESFETs the additional strain and piezoelectric charge dipoles at the edges of the gate metallization has been modeled [83]. These local induced strains in the AlGaN layer at the edges of the metal electrodes may have an impact on device performance by influencing the 2-DEG local sheet charge density. Furthermore, if there exist a significant amount of induced strain at the drain end of the gate which adds up the elastic energy in the AlGaN barrier at this region, a variation in critical voltage bias conditions to degrade the device under pinch-off or ON-state conditions is expected [8].

To investigate the residual stress distribution in the conductive channel of AlGaN/GaN HFETs at room temperature, comparative analysis by means of micro-Raman spectroscopy and PL was done. Stress introduced by metallization structures is discussed.

4.3 Experimental Methodology

GaN with its energy band gap of about 3.4 eV at room temperature is transparent to visible laser sources. Thus in utilizing a sub-band gap laser for Raman measurements, Raman data represents a volume average of the stress through the GaN layer (with thickness commonly in the order of 1-2 μm). On the other hand, micro-PL with a He-Cd 325 nm laser source shows the stress near the surface of the GaN since the photon penetration depth for 325 nm is of the order of 80-90 nm [84], [85], [86]. The combination of two techniques offers complementary information to reveal the through-thickness variation of stress in the GaN epilayer (Fig. 20). The direct measurement of the residual strain in the AlGaN layer which is of high importance in terms of device performance and reliability is not simple due to its thickness (on the order of 25 nm). Instead, observation of the through-thickness variation of residual strain in the GaN layer allows a first order estimation of the imposed strains in the AlGaN layer.

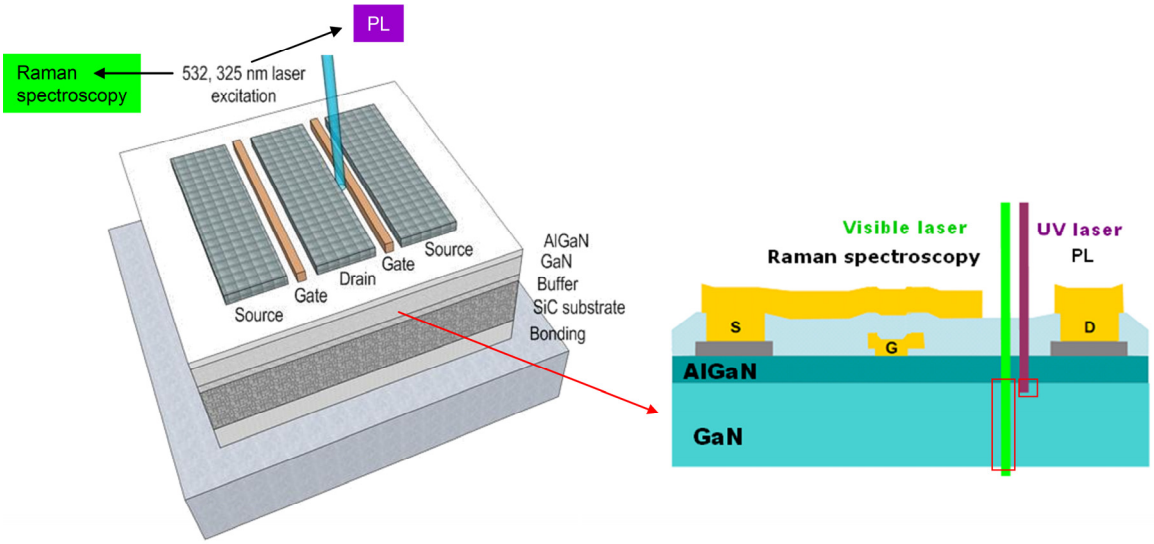

Fig. 20. Laser penetration through a typical AlGaN GaN HEMT structure.

The basic spectrometer setup was similar to that described in Chapter 3. For Raman measurements, 532 nm laser excitation was utilized with a laser power incident on the sample of 25.2 mW. A 50X LWD objective was used to focus the laser spot and collect the Raman signals. The laser spot size was 1.3 μm. For spectrometer initial calibration, spectrometer calibration parameters were adjusted so that the mean value of the E_2 planar optic phonon frequency of 4H-SiC based on at least 50 measurements was 776.599±0.001 cm^{-1}. The 4H-SiC specimen was maintained at 25°C. Again, the widely used method of calibrating the system based on the Si Raman peak of ~520.5 cm^{-1} would also suffice precisely calibrating the spectrometer. However, here 4H-SiC was utilized since dealing with Si using 532 nm and 325 nm lasers is uneasy as stated in Chapter 3. The plasma line frequency (~482.2 cm^{-1} away from the 532 nm Rayleigh scattered line) of an external fluorescence source was used to compensate the thermal drift of the spectrometer with time. These two steps are crucial in determining the absolute magnitude of stress in the measured layer (GaN). PL measurements were carried out with

325 nm UV laser excitation and a 39X quartz NUV objective. Spectrometer calibration was done using 4H-SiC at 0.75 mW incident laser power. This condition was ensured not to induce local heating in the focused region by observing broadening of the 4H-SiC E_2 planar optic phonon linewidth in response to increasing the sample incident laser power starting from 0.3 μW. Even though significant photon absorption occurs (4H-SiC has an indirect bandgap of ~3.2 eV at 300 K), the high thermal conductivity of 4H-SiC effectively spreads the heat away from the laser spot that had a spot diameter of 0.79 μm. Spectrometer drift compensation using an external light source was unnecessary since the PL peak of GaN is much broader than ordinary Raman peaks.

4.4 Results and Discussion

With the stress metrology framework developed in Chapter 3, the stress profiles in electronic devices can be understood. A comparative analysis between the Raman and PL measured stresses in AlGaN/GaN HEMTs was performed in order to investigate the potential of vertical strain gradient formation in the device due to patterned structures. This was done by examining the residual stress (of the GaN layer) at the center points between the gate and drain of fourteen AlGaN/GaN HEMTs from a same sub-reticle with different gate to drain channel spacings. The gate to drain spacings ranged from 1-18 μm and the substrate used in these devices was 6H-SiC. Results are displayed in Fig. 21. As the gate to drain spacing decreases below 5 μm, a tensile shift of the stress near the heterointerface or GaN layer surface is observed whereas the average value of stress through the entire thickness of the GaN layer remains rather constant.

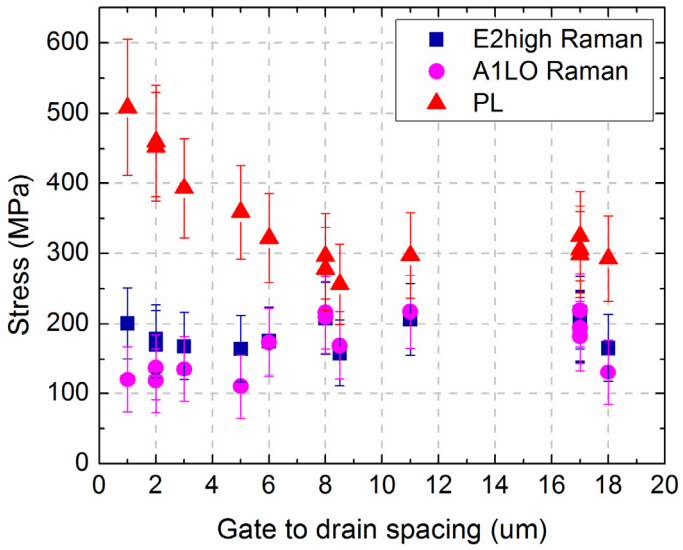

Fig. 21. Residual stress at the center point between the gate and drain of devices with various gate to drain distances measured by Raman spectroscopy and PL.

To assure that the stress shift is induced near the metallization structures, residual stress distributions across the conductive channels of two types of non-field plated devices having same structure (gate to drain and source to gate spacings of 9 μm) but fabricated on different GaN wafers (GaN/6H-SiC) were investigated. Raman spectroscopy and PL measurements were made at intervals of 1 μm between the source and drain metallizations. In Fig. 22, it is observed that for both device types, close to the metal contact edges, the residual stress of GaN near the heterointerface exhibits a significant tensile shift compared to the bulk average value. The residual stresses built in each device type exhibit an opposite sign. Across the conductive channel, the bulk average stress remains rather unchanged. This shift in residual stress near patterned structures may originate from both the stress present in ohmic/Schottky gate electrodes [81], [82] and the stress concentration at the edge of discontinuities of the passivation

overlayer as it basically delivers a force load to the edges of the film or edges of the metal electrodes [17].

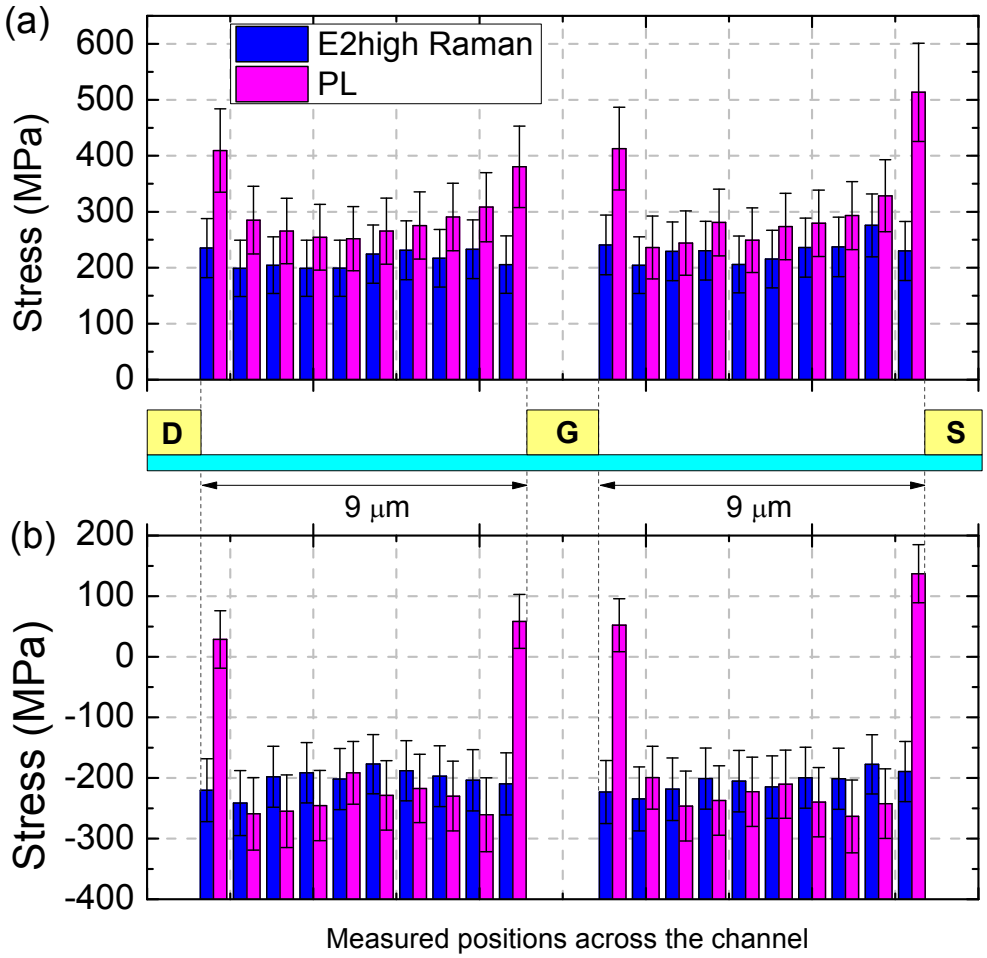

Fig. 22. Residual stress distributions across the conductive channels of AlGaN/GaN HEMTs measured by Raman spectroscopy and PL.

A slight deviation between the Raman and PL measured stresses away from the metallization structures is observed (Fig. 22). In spite of this offset, the Raman and PL

measured stresses tend to fall close into the error bar range of each other. This small offset is believed to be caused by random errors in the experiments.

Similar results, i.e., tensile residual stress shifts in the GaN layer close to the heterointerface compared its bulk average value near metallization structures, were also observable in AlGaN/GaN HEMTs built on Si (Fig. 23). The center points between their gate to drain openings were measured where these devices had gate to drain spacings of 0.5-1 μm. Another observation is that the substrate induced residual stress is highly tensile in GaN/Si devices compared to GaN/6H-SiC devices discussed above.

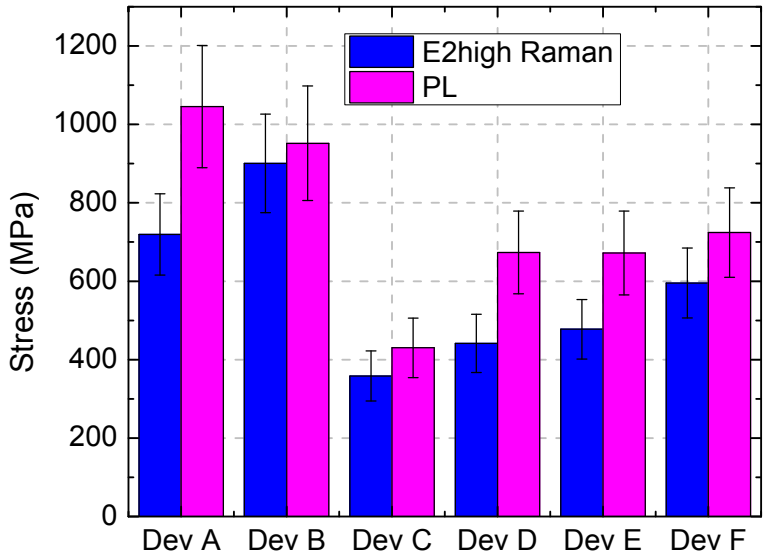

Fig. 23. Tensile shift in the residual stress near the AlGaN/GaN heterointerface caused by patterned structures in AlGaN/GaN/Si devices.

From the discussions done so far, it is obvious that the gate, source, and drain metallization patterns induce tensile stress in the GaN nearest the surface. This is thought

to be an extension from the thin AlGaN layer deposited over the GaN layer. Although the induced stress near the metallization patterns is most likely approximately uniaxial (but probably nonuniform because the ohmic metallizations on AlGaN/GaN are typically morphologically nonuniform), the Raman and PL signatures manifest that an induced tensile strain exists. As the gate pattern induced tensile strain increases the elastic energy built in the AlGaN barrier in addition to the inverse piezoelectric contribution under operating conditions [8], the potential for defect formation may significantly increase. Also, stress related reliability concerns in GaN/Si devices may be more pronounced compared to GaN/SiC devices as the sum of substrate induced residual stress and the gate metal induced tensile stress near gate edge is much higher than that for GaN/6H-SiC devices.

4.4 Summary and Conclusions

In the AlGaN/GaN HEMTs observed, a tensile strain was induced on the AlGaN layer near the edge of metallization structures. The room temperature residual stress in GaN wafers prepared for fabricating HEMT structures can be easily estimated using the discussed optical methods or other techniques such as wafer curvature measurement. However, anticipation of the impact of residual stress on device performance or lifetime solely based on wafer level residual stress without considering the contribution of patterned structures may impart a false sense of such predictions.

Under operating conditions, the tensile strain induced on the AlGaN barrier at the drain side gate edge adds up to the substrate induced residual stress as well as the inverse

piezoelectric stress. Such increase in elastic energy built in the AlGaN barrier will have an adverse effect on device reliability by leading to formation of crystallographic defects which may result in performance degradation such as current collapse and eventually device failure. This means metallization schemes that result in an induction of compressive strain in the AlGaN layer or proper passivation overlayer deposition that results in less tensile strain induced at its edge will be beneficial in terms of device reliability.

CHAPTER 5

THERMOMETRY OF ALGAN/GAN HEMTS USING MULTI-SPECTRAL RAMAN FEATURES

5.1 Overview and Approach

In this work, we utilize micro-Raman spectroscopy to measure temperature and stress in state-of-the-art AlGaN/GaN HEMTs. A rigorous discussion on the physical accuracy, precision, and precautions for diverse Raman thermometry methods is developed. Thermometry techniques utilizing shifts in a single Raman Stokes peak position under-predict the channel temperature due to induction of operational thermo-elastic stress in operating devices. Utilizing the change in phonon linewidth by employing a proper reference condition gives true temperature results. Making use of frequency shifts in both the E_2(high) and A_1(LO) phonon mode offers accurate and time-efficient means to determine the state of temperature and thermal stress in operating AlGaN/GaN HEMTs presuming that linear relations between phonon frequencies and temperature/stress are well determined. Useful applications of this method such as monitoring stress in GaN wafers between fabrication steps and Raman thermography on AlGaN/GaN HEMTs are demonstrated.

5.2 Motivation

The typical method to measure temperature in microelectronics or microelectromechancial systems (MEMS) using micro-Raman spectroscopy is to convert the frequency shift of a single phonon mode from a reference state to an operating state into the corresponding amount of temperature rise. However, as shown in the previous Chapters 3 and 4, the stress dependence of the phonon frequency hinders accurate lattice temperature estimation using this conventional method for practical applications due to stress evolution accompanied by temperature rise arising from the thermo-elastic effect. Temperature measurement of operating AlGaN/GaN HEMTs independent of stress effects was demonstrated in [52] using the linewidth based Raman thermometry method. However, for this phonon linewidth based method, higher uncertainty levels compared to those resulting the single peak position based thermometry method are inevitable. Typical temperature uncertainties resulting from the linewidth based method and the single peak position based method are ±6 K and ±1.5 K, respectively. In addition, determination of the phonon linewidth becomes difficult when multiple Raman peaks coming from different layers of the device overlap. For example, in GaN on Si devices, the GaN E_2(high) mode peak (~568 cm^{-1}) overlaps with the dominant Si Raman peak (~520 cm^{-1}) that comes from the Si substrate. When multiple zone-center phonon modes are detectible for a material under interest, stress and temperature contributions to the phonon frequency shifts between an operating state and a reference state can be readily separated. Recently, a thermometry method utilizing both shifts in the E_2(high) and A_1(LO) mode (of GaN) peak positions was proposed [53]. The Raman signatures of these phonon

modes were shown in Fig. 7. This method is most time efficient among the Raman thermometry methods discussed so far since the temperature calibration process for the specimen is not required. Also it offers relatively low uncertainty in the temperature results compared to the linewidth based method. The key for implementing this technique is precise knowledge of the relationships between the shift of the phonon frequencies with temperature rise and induced stress. Unfortunately these relations reported in literature lack of consistency thus the practical use of this technique was limited.

In this study, we develop a Raman thermometry method (linear 2-peak fit method) which has advantages such as short experiment time and simplicity in data handling compared to previously developed techniques [52], [53]. A framework to determine stress / temperature-phonon frequency relations is developed (stress relations were established in Chapter 3 and briefly revisited in this chapter). Then the validity of using this technique is checked by comparing obtained temperature and stress results to those deduced from different Raman thermometry techniques and 3-D finite-element thermo-mechanical simulation. A thermography map of the full channel of a custom AlGaN/GaN HEMT (standard in every way except for the source-gate and gate-drain spacing) was constructed using the developed Raman thermometry technique.

5.3 Devolopment of Thermometry Technique

5.3.1 Derivation of Stress / Temperature – Phonon Frequency Relations

The method proposed in [53] utilizing shifts in frequencies of both the E_2(high) and A_1(LO) mode between the powered state and the pinch-off state offers means to assess operational thermo-elastic stress and temperature simultaneously provided that the evolved stress is biaxial in the c-plane of GaN. This method can be furthermore simplified as linear temperature/stress-phonon frequency relations hold for practical ranges of temperature and biaxial stress, e.g., from room temperature to ~500 °C and from -1 to 1 GPa, respectively. In [53], a nonlinear empirical expression for the temperature dependence of the E_2(high) and A_1(LO) modes was adopted. The temperature rise ($\Delta T=T-T_0$) from a reference state (pinch-off, T_0) of an operating device can be extracted by observing the alteration of the Raman shifts of the E_2(high) and A_1(LO) modes of GaN between an operating state (ω) and a reference condition (ω_0). In assessing the magnitude of induced operational thermo-elastic stress (σ_a), it is assumed that elastic deformation takes place between the two states.

$$\begin{aligned} (\underbrace{\omega-\omega_0}_{\Delta\omega})_{E2(high)} &= A_{RS}^{E2(high)}(\underbrace{T-T_0}_{\Delta T})+K_{RS}^{E2(high)}\sigma_a \\ (\Delta\omega)_{A1(LO)} &= A_{RS}^{A1(LO)}\Delta T+K_{RS}^{A1(LO)}\sigma_a \end{aligned} \tag{13}$$

For AlGaN/GaN HEMT measurement, the pinch-off state (at same base plate temperature as the ON-state) is chosen as the reference condition since then the electrical contribution

to shift in phonon frequencies is cancelled out which stems from the inverse piezoelectric effect. The inverse piezoelectric stress induced in the device channel is not strictly biaxial [87], thus cannot be analyzed using the Raman thermometry method discussed here.

This linear '2-peak fit method' is advantageous over the single peak position or linewidth based techniques in terms of experimental time and accuracy provided that the induced stress in the GaN layer between two states is biaxial. Other methods require a temperature calibration process to generate a map that records the change in Raman signal as the device is uniformly heated up to known temperatures. Then the relative change in the Raman response acquired during device operation from that taken at a reference (pinch-off) condition is converted to 'operating temperature' based on this calibration map. When measuring multiple locations within a device, one has to build calibration maps for all individual measurement points to get best results. This calibration process is not only time consuming but also can be a major source of errors in the derived temperatures. Fluctuation in the thermal environment surrounding the device during calibration is mainly responsible for these errors. The 2-peak fit method does not require this calibration process since it solely relies upon the intrinsic character of the material, i.e., shift in phonon frequency in response to temperature elevation or applied stress. However, employment of this technique requires precise determination of the relations between temperature/stress and the frequency shifts of the E_2(high) and A_1(LO) phonon modes of GaN. The temperature-frequency relations are relatively easy to deduce. But the (biaxial) stress-frequency relations that exist in literature are lacking of consistency. With recent improvement in processing technology and development of high quality GaN epi-layers, there is opportunity to revisit these relations. This procedure was shown in

Chapter 3 and briefly repeated below.

Raman spectroscopy and x-ray diffraction (XRD) measurements were conducted on commercial unintentionally doped (UID) MOCVD or HVPE grown GaN templates employing diverse substrate materials. Lattice constants of the GaN epi-layers were determined by X-ray diffraction (XRD) measurements using PANalytical X'Pert Pro system equipped with a Cu Kα x-ray source. Strain in each layer was calculated based on true lattice constants of GaN (a_0=3.1878 Å and c_0=5.1850 Å) suggested in [57]. Stress-strain relations for the relevant case for thin layers having homogeneous biaxial stress in the c-plane and being stress free in the growth (c-axis) direction are well described in [45]. Elastic stiffness constants of GaN listed in Table. 2 [67] were adopted.

Table 2. Structural properties of materials.

Material	Stiffness matrix (GPa)					Young's modulus (GPa)	Poisson's ratio
	C_{11}	C_{12}	C_{44}	C_{13}	C_{33}		
GaN [67]	390	145	105	106	398	-	-
Sapphire* [88]	491	167	146	115	491	-	-
6H-SiC [89]	501	111	163	52	553	-	-
Si_3N_4 [90]	-	-	-	-	-	195	0.25
Au [91]	-	-	-	-	-	97	0.421
CuW(15:85) [92]	-	-	-	-	-	390	0.3
AuSn Solder	-	-	-	-	-	30	0.4

* For Sapphire, C14=-23 GPa

Raman measurements were performed on each sample (at the same location where XRD measurements were conducted) to correlate the Stokes Raman frequencies to the degree of biaxial stress within each GaN epi-layer. Raman spectroscopy measurements were performed using Horiba Jobin Yvon LabRAM HR800. A 532 nm sub-band gap

laser excitation was utilized. Incident laser power was adjusted (2.4-25.2 mW) to prevent local heating in the GaN layers as well as the substrate materials. The focused laser spot diameter was 1.3 μm. Measurements were carried out with the laser light perpendicular to the c-plane and incident on the Ga-face of GaN in a 180° backscattering configuration and un-polarized detection. Samples were mounted on a heating stage (INSTEC HCC324S) maintained at 25 °C (±0.06 °C) during measurement. Linear relations were observed and the stress conversion factors for each phonon mode were determined from the slope of the fitting line of the data shown in Fig. 16. This entire process to derive Raman stress conversion coefficients was explained in detail in Chapter 3.

Temperature-phonon frequency relations were derived by performing *in situ* Raman measurements while heating a bulk high quality HVPE GaN substrate to known temperatures (25-300 °C). Derived stress and temperature conversion factors are summarized in Table. 3 and are in nice agreement with values reported in [11] ($K_{RS}^{E2(high)}$=-2.7±0.3 cm^{-1}/GPa) and [75] ($K_{RS}^{A1(LO)}$=-1.91±0.58 cm^{-1}/GPa). Here the 95% confidence intervals were deduced based on error propagation from uncertainties in all optical measurements (XRD and Raman) as well as adopted elastic modulus.

Table 3. Linear stress / temperature conversion coefficients.

Coefficient	Units	Best estimate	95% confidence interval
$K_{RS}^{E2(high)}$	cm^{-1}/GPa	-3.09	±0.41
$K_{RS}^{A1(LO)}$	cm^{-1}/GPa	-2.14	±0.28
$A_{RS}^{E2(high)}$	cm^{-1}/°C	-0.015	±0.0001
$A_{RS}^{A1(LO)}$	cm^{-1}/°C	-0.0281	±0.0001

5.4 Results and Discussion

5.4.1 Verification of Developed Thermometry Scheme

To check validity of utilizing the 2-peak fit method with the derived linear conversion coefficients, Raman measurements were conducted on a GaN/Sapphire epi-stack subject to diverse known temperatures ranging from 25 to 300°C. The thickness of the GaN and sapphire layers were 10 μm and 340 μm, respectively. A 3-D finite-element model (COMSOL using *Solid Mechanics* module) including the full geometry of the epi-stack (length and width of 5190 and 3230 μm, respectively) but taking into account of quarter symmetry was built using elastic stiffness matrices and temperature-dependent anisotropic thermal expansion coefficients listed in Table. 4. The input parameter was temperature of the epi-stack (known) and thermal stress induced in the GaN layer at a heated state from a zero-stress reference condition (T_0=25°C) was the model output. The (known) epi-stack temperatures and stress results from the model were compared with experimental values deduced from the linear 2-peak fit Raman thermometry method using (13). Very nice agreement is observed in Fig. 24 which gives confidence in utilizing the derived linear stress/temperature conversion coefficients along with the 2-peak fit method. The average deviations from the model outputs within the studied temperature range are less than 5% when using the derived coefficients whereas an average deviation of 20% and 40% for temperature and stress, respectively, results by using linear coefficients previously reported in literature, for example, using the best estimates of stress coefficients derived in [75]. This experiment is of prominent

importance since it suggests the capability of utilizing the 2-peak fit method to accurately estimate the stress variation in GaN wafers during post-growth cooling to room temperature.

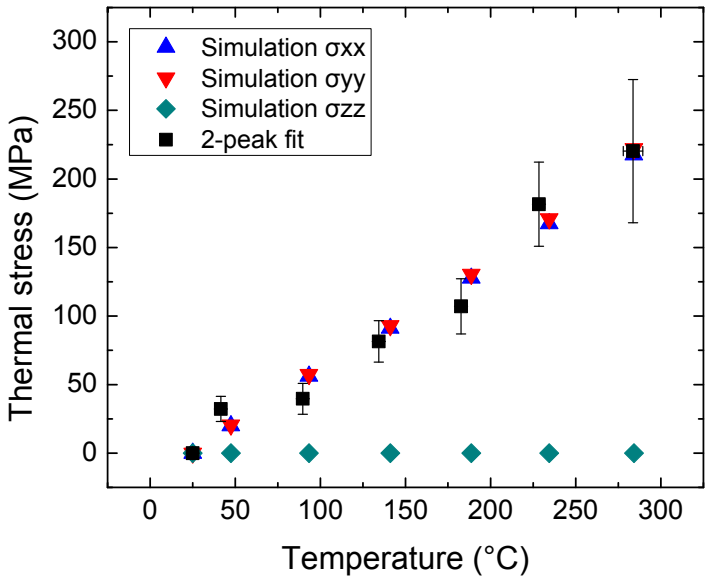

Fig. 24. Evolution of the thermo-elastic stress in a GaN epi-layer grown on top of a Sapphire substrate as temperature increases. Simulation results show the induced stress is biaxial in the c-plane of GaN, i.e., $\sigma_{xx} \approx \sigma_{yy}$ and $\sigma_{zz} \approx 0$. σ_{xx} and σ_{yy} are the normal stress components in the c-plane of GaN whereas σ_{zz} is the normal stress along the c-axis. Both temperature and stress are estimated from the 2-peak fit Raman thermometry method by observing shifts in the E_2(high) and A_1(LO) mode frequencies

Table 4. Thermal properties of materials.

Material	Coefficient of thermal expansion ($\times 10^{-6}$ K^{-1})	Thermal conductivity (W/mK)
GaN [58], [93]	α_a=-1.44×10^{-5}T^2+1.7×10^{-2}T+0.553 α_c=-1.39×10^{-5}T^2+1.64×10^{-2}T+0.216	150×(T/300)$^{-1.4}$
Sapphire [61]	α_a=-4.64×10^{-8}T^2+4.05×10^{-3}T+5.04 α_c=-5.35×10^{-8}T^2+4.2×10^{-3}T+5.8	41.9
6H-SiC [94], [95]	α_a=-1.36×10^{-6}T^2+3.99×10^{-3}T+2.28 α_c=-8.51×10^{-7}T^2+2.94×10^{-3}T+2.44	387×(T/293)$^{-1.49}$
Si_3N_4 [96], [97]	1.5	4.5
Au	14.2	317
CuW(15:85) [92]	7	204-2.51×10^{-2}T-7.62×10^{-5}T^2
AuSn Solder	24	49.8

Temperature should be input in Kelvin scale.
All temperature dependent properties are valid within the range of 300-550 K.

5.4.2 Application to Characterizing Devices

5.4.2.1 Operating Temperature and Thermal Stress in the Channel

The operating temperature of a six-finger non-field plated AlGaN/GaN HEMT was examined using the aforementioned Raman thermometry techniques and finite-element thermo-mechanical simulation. The gate width and gate to drain channel spacing were 370 μm and 3 μm, respectively. The thickness of the GaN buffer was ~2 μm and semi-insulating (SI) 6H-SiC was used as the substrate material. The process technology was similar to that described in [98]. Raman thermometry was conducted at the drain side gate edge at the midpoint along the third channel from the device edge. The Raman

spectrometer configuration was identical to the setup for GaN template measurements (section 5.3.1). The incident laser power (25.2 mW) was chosen after confirming minimal effect of the laser on device operation by conducting measurements at diverse laser powers. Temperature calibration which is required for the single peak position and linewidth based Raman thermometry was performed by collecting Raman Stokes signals of the device uniformly heated (without voltage applied) to known temperatures (25-300°C) using a LINKAM TS1500 temperature controlled stage (temperature stability: ±1°C). Then the device was examined under operating conditions. Rise in channel temperatures from reference pinch-off states (V_{gs}=-8 V, V_{ds} same as corresponding ON-state condition, T_0=85°C) were deduced from Raman measurements and are shown in Fig. 25. Device output power was varied from 1.26 to 11.69 W (0.57-5.27 W/mm) at fully opened gate conditions (V_{gs}=2.55 V). The device base temperature under the package was maintained at T_0=85±0.2°C using an INSTEC HCC324S temperature controlled stage. Uncertainties (95% confidence bounds) in resulting temperatures were determined based on error propagation from uncertainties in the temperature calibration process, uncertainties in the stress/temperature conversion coefficients, and statistical random errors from multiple Raman measurements.

A 3-D Finite-element thermo-mechanical model was constructed using COMSOL's *Heat Transfer* and *Solid Mechanics* modules to simulate the thermo-mechanical behavior of the device. The entire structure of the device module was considered in the model including the HEMT structure constructed on the center portion of an AlGaN/GaN/AlN/SiC die attached to a CuW package by a thermal die attach material. Patterned structures such as metal electrodes and the Si_3N_4 passivation over-layer were

also included. Physical dimensions of the simulated device were similar to those described in [99]. Material properties summarized in Table. 3 and 4 were carefully chosen to take into account of the anisotropic character of certain materials, temperature dependence in specific properties, and dependence on processing methods (e.g., low temperature PECVD grown Silicon Nitride passivation with thickness of ~0.5 μm used instead of properties from 'bulk' Si_3N_4 fabricated using different techniques). For simplicity the metal electrodes were assumed to have material properties of a thin gold film. The AlGaN layer was excluded in the simulation. This thin layer (~20 nm) with low thermal conductivity (~30 W/mK [100]) would not significantly affect the channel temperature under situations with natural convection boundary conditions imposed on the device surface [101]. For structural analysis, excluding this layer could be justified by its thinness since the degree of thermal stress induced in the much thicker GaN layer would not be affected by the thin AlGaN layer on top of it. The bottom and sides of the CuW package were held at 85°C while other boundaries including the surface of the package and sidewall of the device module were exposed to natural convection (h=5 W/m^2K). The heat generation in each channel was approximated by a boundary heat source at the GaN surface below the passivation layer and between the source and drain ohmic contacts. This is a reasonable approximation only for bias conditions where the gate is fully opened. In such case with low voltage bias, an electric field spike is not formed below the gate edge which would occur at high bias conditions where a 'hot spot' forms near the drain side gate edge as a result of normal FET operation (carrier depletion under the gate) as well as complex phonon interactions and ballistic transport effects driven by the intense local electric field [26]. For high bias conditions, the use of

Fourier's law assuming the heat generation region as a uniform source along a fixed area near the gate for predicting operational junction temperatures cannot be strictly justified. For the structural side regarding thermo-elastic effects, the package was fixed by two screws (bottom clamped, top surface fixed in one lateral direction) and other boundaries were set free to move except the symmetry boundaries. Thus the effects of the extension of the die outside of the HEMT structure as well as package mounting conditions were all considered. Effective thermal boundary resistance between GaN and SiC was assumed to be 6×10^{-8} m^2K/W which is on the same order in magnitude with values reported in [102]. Also the thermal boundary resistance occurring between the CuW package/ZnO-thermal grease/Cu mount interface was assumed to be 8.93×10^{-6} m^2K/W according to [103]. The continuum heat transfer equations were first solved then the resultant temperature distribution throughout the entire structure was used to obtain the thermal strain. Finally, linear elastic equations were solved to calculate the thermo-elastic stress induced in the device. Modeling results displayed in Fig. 25 represent an average over a volume similar to the micro-Raman probing volume at the same location in the channel where Raman measurements were conducted.

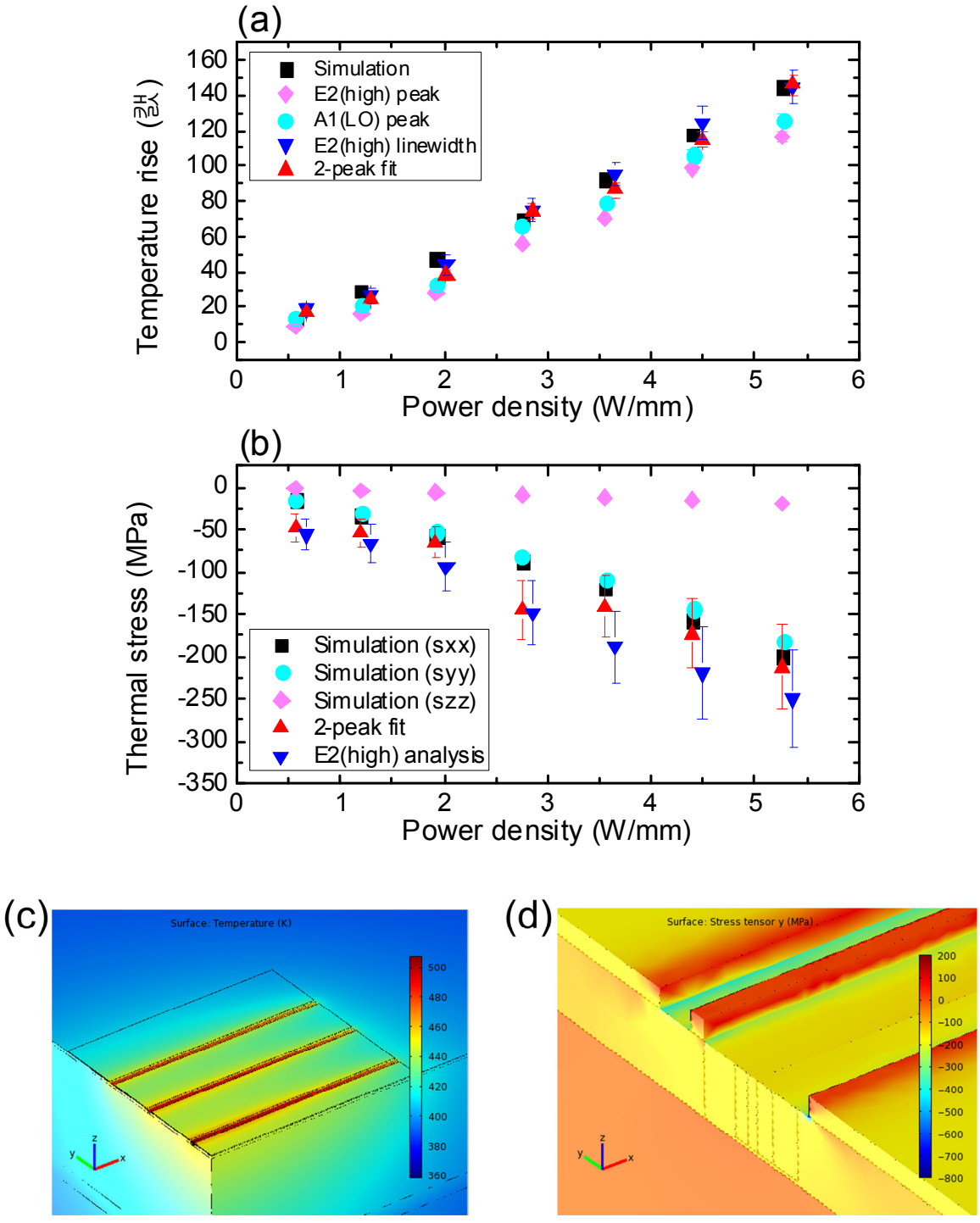

Fig. 25 (a) Channel temperature at various power conditions deduced from the thermo-mechanical simulation as well as diverse Raman thermometry techniques; 2-peak fit method, linewidth based method, and techniques based on single peak positions. (b) Operational thermo-elastic stress induced at diverse power conditions. Simulation results show the stress is closely biaxial and agree well with values obtained from the 2-peak fit method. Also shown is stress derived from analyzing the peak shift and broadening of the

E_2(high) mode. Some data points including their error bars are offset for clarity. (c) and (d) show temperature and y-direction normal stress results, respectively, from the simulation at 4.5 W/mm power dissipation (V_{gs}=2.55 V and V_{ds}=7 V).

Temperature deduced from the 2-peak fit method, linewidth based method, and simulation show reasonable agreement within error bar ranges as shown in Fig. 25 (a). Single peak position based methods using either the E_2(high) or A_1(LO) mode significantly underestimate the channel temperature due to evolution of compressive operational thermo-elastic stress. The A_1(LO) frequency based temperature is closer to the true channel temperature compared to the E_2(high) frequency based temperature due to lower sensitivity to c-plane biaxial stress ($K_{RS}^{A1(LO)} < K_{RS}^{E2(high)}$). The A_1(LO) phonon mode corresponds to atomic oscillations along the c-axis whereas the E_2(high) mode of GaN corresponds to the atomic oscillation in the c-plane which has a non-polar character and is therefore more sensitive to the lattice strain in the c-plane. Agreement between the thermal stress acquired via 2-peak fit method and simulation is reasonable. The other stress (σ_a) plot in Fig. 25 (b) was obtained by analyzing the peak shift and broadening of the E_2(high) mode and using the following equation.

$$(\omega - \omega_0)_{E2(high)} = A_{RS}^{E2(high)}(T_\Gamma - T_0) + K_{RS}^{E2(high)}\sigma_a \tag{14}$$

Here T_Γ is the channel temperature deduced from the line-broadening of the E_2(high) mode linewidth or FWHM, T_0 is the base plate temperature or device temperature at pinch-off (85°C). Other terms have same meaning as those in (13). The slight overestimation in the magnitude of thermal stress resulting from (14) is mainly caused by

the difference in the temperatures deduced from the 2-peak fit method and linewidth based method which may have come from errors in the temperature calibration process. Again in (13) and (14), measurement results taken at two different states, i.e., open channel (ON-state) and pinch-off (reference state), were considered to extract temperature and stress information.

5.4.2.2 Thermal Imaging of an Operating Device

Different from other thermometry techniques such as IR thermography, Micro Raman spectroscopy is a local point-to-point measurement technique with high spatial resolution mainly limited by the wavelength of the laser excitation source (diffraction limited optics). However, there are occasions when spatial temperature distributions with high precision are required, for example, when examining location of local hotspots formed due to nonuniformity in the fabrication or by device degradation. The variation of local temperature calibration maps is unpredictable though the variation may not be significant. Thus in order to obtain best thermometry results, performing calibration on each measurement point under interest is necessary. This hinders Raman thermometry for being implemented as a tool for conducting spatial mapping on a broad region within a device. Since the 2-peak fit method relies on intrinsic attributes or predetermined temperature/stress-phonon frequency relations, it doesn't require a temperature calibration process. Therefore this method has extraordinary merits with regards to high resolution thermography of AlGaN/GaN HEMTs. Thermal drift of the spectrometer (mainly caused by room temperature change) during prolonged mapping measurements

can be compensated if an additional peak from an external light source, for example, neon or fluorescent lamps, is intentionally introduced in the Raman spectral window monitored. Fig. 26 is a result of performing Raman spatial mapping on one entire channel of a 2-finger device built based on similar epitaxial processing as the previously studied 6-finger device except dimensions of the patterned structures. Channel width was 196 μm and gate field plate length was 3 μm. Gate to drain and source to gate spacings were 8 μm. The Raman setup used was identical to that described in the former subsection. Mapping step size was 1 μm along the channel width and 0.5 μm across channel length. The bottom of the device package was maintained at 50°C. The device was under DC operation at 2.16 W (5.4 W/mm) sustained by adjusting V_{gs} and keeping V_{ds} at 20 V. For the reference pinch-off state, the device was biased at V_{gs}=-8 V and V_{ds}=20 V. Temperature conversion was performed using (13) and results are displayed in Fig. 26. Peak temperature occurs in the vicinity of the drain end of the gate where electric field concentration occurs. Low electron density or high electric resistance at this local region results in concentration in electron joule heating.

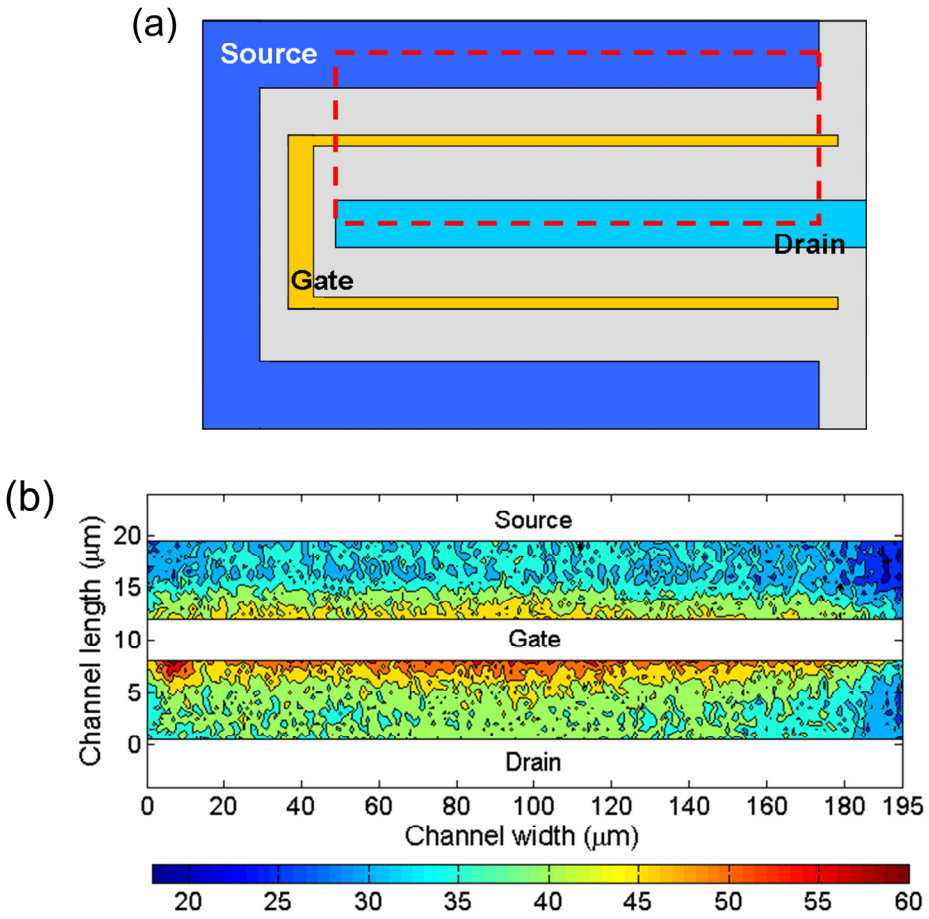

Fig. 26 Full map of temperature rise in one channel (from the base temperature of 50°C) of a 2-finger device obtained from the Raman thermography using the 2-peak fit method. The actual measured channel area corresponding to the temperature map in (b) is indicated in (a). The result in (b) shows that the channel is hotter between the drain and gate than the source-gate opening where peak temperature occurs at the drain end of the gate due to electric field concentration.

5.5 Summary and Conclusions

In this work, we utilized micro-Raman spectroscopy to measure temperature and operational thermo-elastic stress in state-of-the-art AlGaN/GaN HEMTs. An accurate and time-efficient method was developed based on work in [53] but using simplified linear

equations. Linear coefficients that relate biaxial stress ($K_{RS}^{E2(high)}$=-3.09±0.41 cm^{-1}/GPa, $K_{RS}^{Al(LO)}$ = -2.14±0.28 cm^{-1}/GPa) and temperature to the phonon frequency shifts of GaN ($A_{RS}^{E2(high)}$=-0.015±0.0001 cm^{-1}/°C, $A_{RS}^{Al(LO)}$ = -0.0281±0.0001 cm^{-1}/°C) were determined for realization of this technique. This method is very useful in characterizing GaN based MEMS and microelectronic thin film devices since the state of stress in them is commonly biaxial. Through the use of this thermometry method, obtained channel temperatures were similar to those deduced from the linewidth based Raman thermometry technique [52] but with uncertainty levels lower by ~40% as shown in Fig. 25. Operational thermo-elastic stresses obtained from this method also possessed lower uncertainty (~20% less). Techniques utilizing single peak shifts do not separate stress effects thus underestimate the channel temperature. Shorter experiment time and potential higher accuracy is also expected for the 2-peak fit method since it does not require a temperature calibration process. However, one should notice that the 2-peak fit method is only valid when the evolved stress is biaxial in the c-plane of GaN. Thus in case of measuring temperature in GaN based devices where three dimensional stresses are expected, e.g., below patterned structure edges (this effect was clearly observable via the model developed in this study), one should take precautions for utilizing this method. The linewidth based method gives more flexibility to the experimentalist in such cases. For symmetry-conserving stress situations [104] such as c-plane biaxial stress, c-axis uniaxial stress, and hydrostatic stress, no splitting of phonon frequencies occur and the stress effect on the Raman signature is revealed by only a frequency shift [22]. Under such situations but other than a biaxial stress case, the linewidth based method is recommended if proper reference states can be defined.

CHAPTER 6

THE IMPACT OF BIAS CONDITIONS ON SELF-HEATING IN ALGAN/GAN HEMTS

6.1 Overview and Approach

The thermal response of AlGaN/GaN high electron mobility transistors (HEMTs) directly correlates with the overall performance, reliability, and lifetime of these devices. In general, a hot spot develops near the drain end of the gate electrode during power dissipation. The device channel temperature was examined via micro-Raman thermometry under various bias conditions where power dissipation levels were identical. Under these bias conditions, difference in internal states (sheet carrier density and electric field distribution) within the device alters the heat generation profile across the channel. High V_{ds} conditions lead to significantly higher channel temperature compared to that for low V_{ds} conditions although the power dissipation is kept constant. Experimental results show ~13°C deviation between V_{ds}=45 V and V_{ds}=7 V cases when the power dissipation is 4.5 W/mm. This suggests that bias conditions may have a relatively significant impact on device reliability and that this effect must be considered when building thermal models of devices under operation or undergoing accelerated life testing.

6.2 Motivation

It was reported through simulation [105] and experiments [106] that bias conditions alter the ratio of power dissipated in the pinch-off region to that dissipated in the rest of the device thus having an influence on device peak temperature. However, this bias dependent self-heating effect has not been explored yet in order to determine the potential magnitude of the variation in temperature rise over a wide enough range including both practical operating conditions, for example, V_{ds}=28 or 48 V, and open channel conditions which are frequently used to assess the thermal response of operating HEMTs.

Comparison of open channel conditions to practical operating conditions where V_{ds} is high (e.g., V_{ds}=28 V, 48 V) is very important in terms of device lifetime prediction. Key reasons are enumerated below:

1. Variation in device peak temperature (due to different bias conditions) although the dissipated power is same can lead to wrong derivation of the activation energy for predicting mean time to failure (MTTF) of devices via accelerated lifetime tests. Thus the bias condition used in the three temperature accelerated life test has to be considered seriously.

2. People are often not careful about the bias conditions used to get a thermal resistance. They may use whatever bias condition is more convenient for measuring the temperature rise and then relate it to a life test runs at different conditions.

3. Given an activation energy (from literature), since the max temp within the device varies with bias conditions, the MTTF of the device is closely related with the operating bais conditions. When comparing a fully opened device and a highly

biased device (e.g., V_{ds}=48 V), their MTTF can vary by an order of magnitude.

The channel temperature of a 6-finger non-field plated AlGaN/GaN HEMT was examined via micro-Raman spectroscopy under various bias conditions (combination of V_{gs} and V_{ds}) while the power dissipation level was kept constant (4.5 W/mm). First the E_2(high) phonon linewidth based Raman thermometry method from [52] briefly discussed in Chapter 5 was utilized to assess the true lattice temperature. Channel temperatures deduced from single phonon frequency shifts are compared with the obtained results and discussed. Then the linear 2-peak fit method developed in Chapter 5 was used to reproduce the trend of the dependence of operating temperatures on bias conditions. Finally these results were compared with electro-thermal simulations.

6.3 Experimental Methodology

6.3.1 Experimental Setup and Tested Conditions

Raman spectra were recorded using a confocal Raman microscope Horiba Jobin Yvon LabRAM HR800. A 532 nm diode-pumped solid-state laser was used as the excitation source. A 1800 groove/mm diffraction grating was used and the confocal hole size was adjusted to 100 μm. This setup was established to obtain high enough spectral dispersion (0.28 cm^{-1}/pixel CCD) suited for temperature measurements, reasonable acquisition time (~13.5 sec for a single measurement), spectral range adequate for

examining multiple phonon modes (300 – 820 cm^{-1}), and for obtaining reasonable signal-to-noise ratio (~70:1 for the E_2(high) peak) for each measurement. Data acquisition times were adjusted to obtain consistent Raman intensity counts (~8000) of the GaN E_2(high) peak. Measurements were carried out with the laser light perpendicular to the basal plane of GaN in a 180° backscattering configuration and un-polarized detection. The E_2(high) and A_1(LO) modes were primarily investigated among the allowed zone-center optical phonon modes detectable for this configuration [9]. The E_2(low) mode (~143 cm-1) was not examined due to overlap with the folded transversal acoustic mode (E_2 symmetry) [107] of the 6H-SiC substrate. The 532 nm laser power incident on the devices was adjusted via neutral density filters to ~25.2 mW and ~2.4 mW. The sub-band gap laser wavelength (532 nm) used for Raman measurements prevents localized heating of GaN by laser light absorption. For devices under electrical bias, negligible carrier induced local heating at this setup was confirmed by comparing the Raman response acquired from the aforementioned two excitation power levels. A 50X LWD objective (NA = 0.5) was employed to focus the laser on the sample surface and collect the Raman signatures. The theoretical diffraction limited laser focused spot diameter was 1.3 μm. Before conducting Raman measurements, the system was calibrated at 25°C with a 4H-SiC piece to 776.599 cm^{-1} which was equivalent to 520.46 cm^{-1} for high quality single crystal silicon. Pinch off state measurements were conducted before and after every ON-state temperature measurement to take into account of the drift (systematic error) of the spectrometer. In order to determine the peak position and full width at half maximum (FWHM), Raman spectra were fitted using a linear combination of Gaussian–Lorentzian line-shapes.

Six-finger AlGaN/GaN HEMTs fabricated on 6H-SiC with a gate width of 370 μm and gate to drain channel spacing of ~3.5 μm were examined. The thickness of the GaN layer was ~2 μm. These devices employed T-gates but not source connected field plates which would hinder optical access to the channel. This allowed temperature observation close to the drain end of the gate. Processing technology used to fabricate the devices was similar to that described in [108].

Raman thermometry was conducted 0, 1, and 2 μm away from the drain side gate edge at the midpoint along the third channel from the device edge. Device output power was controlled to 10 W (4.5 W/mm) at various V_{ds} conditions ranging from 7 to 80 V by adjusting V_{gs}. The device base temperature under the package was maintained at 85°C (±0.2°C) while mounted on a heating stage (INSTEC HCC324S).

To calibrate the device Raman response, i.e., peak shift and line broadening, to temperature rise, Raman Stokes signals were collected (20 spectra for each condition) while the device was isothermally heated to known temperatures (25.0, 45.8, 89.0, 135.0, 181.0, 229.5, and 278°C) without voltage applied using a LINKAM TS1500 temperature controlled stage with a temperature stability of ±1 °C. Fig. 27 shows the down shift and broadening of the GaN E_2(high) and A_1(LO) modes in response to elevated device temperature. A linear fit was used to describe shifts in phonon frequencies with respect to change in temperatures. A second order polynomial did suffice to represent the relation between change in linewidths and change in temperatures from the reference condition (25°C).

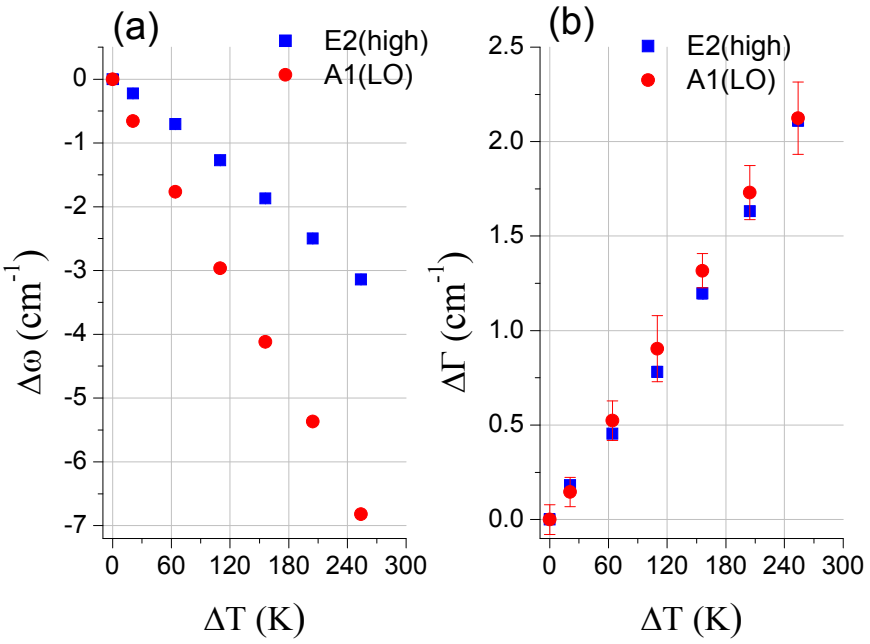

Fig. 27. Temperature calibration results relating the change in temperature to change in Raman responses (peak position and linewidth). (a) Degree of red shift in the E_2(high) and A_1(LO) mode frequencies in response to temperature rise. (b) The line broadening of respective phonon modes caused by temperature elevation.

Then the actual device temperature measurements for each bias condition were carried out by conducting a total of 60 measurements; 20 measurements at a pinch-off condition (V_{gs}=-8 V) for a given V_{ds} to be investigated, then 20 measurements for that ON-state condition at that V_{ds}, followed by 20 more measurements at the previous pinch-off condition. This pinch-off condition is chosen because it is electrically similar to the corresponding ON-state condition (especially at higher V_{ds}) but with negligible power dissipation. Briefly, this method is discussed in detail elsewhere [52] but involves separating the voltage induced changes in the device that affect Raman from the thermal changes we want to measure; it is not sufficient to simply measure the change in the Raman signal at ON-state from an unbiased reference state (at a certain base plate

temperature) and ascribe all of the change to heating. Pinch-off state measurements were conducted before and after every ON-state temperature measurement to take into account of the thermal drift or systematic error of the spectrometer due to change in room temperature.

The amount of line-broadening between the ON-state and the reference pinch-off state (V_{gs}=-8 V, V_{ds} same as corresponding ON-state) is converted to channel temperature rise based on the obtained device temperature calibration map. Then the operational thermo-elastic stress (σ_a) arising due to channel temperature rise between the two measured states can be estimated using the following equation.

$$\omega - \omega_0 = A_{RS}^{E2(high)}(T - T_0) + K_{RS}^{E2(high)}\sigma_a \tag{15}$$

where ω is the measured E_2(high) phonon frequency at ON-state, ω_0 is the E_2(high) mode frequency at pinch-off, T is the channel temperature deduced from the change in the E_2(high) mode linewidth, T_0 is the base plate temperature (85°C) or device temperature at pinch-off, and $K_{RS}^{E2(high)}$ is the Raman biaxial stress conversion factor derived in Chapter 3. $A_{RS}^{E2(high)}$ is a linear coefficient expressing the E_2(high) mode frequency shift of bulk GaN in response to temperature rise. This coefficient was determined to be -0.015±0.0001 cm^{-1}/°C by heating a high quality HVPE GaN sample at known temperatures and performing in situ Raman measurements (also shown in Chapter 5).

Experiments for each 'set' of measurements for each bias condition (here one 'set' consists of one powered state measurement in between of two pinch-off condition measurements) were conducted at least twice to assure the results were reproducible. Best

estimates and uncertainties (95% confidence bounds) for temperatures were obtained by conducting statistical analysis.

Special care has been taken in experiments not to be confused by the problematic sources at high or low V_{ds} conditions to ensure that we observed the bias dependence described in this study. The issues are outlined below:

1. Higher V_{ds} related issues:

    a. Non-uniformity within the device (hot spots) that can show up at higher drain biases that may ruin the meaningfulness of the comparison on the experimental side.

    Solution) Measured multiple locations (different channels within the device) and confirmed this bias dependence even at the coldest part of the device active region. Also confirmed the uniformity of the power dissipation along the gate width and from one finger to the next using thermal infrared microscopy.

    b. Real-time degradation while collecting the data

    Solution) The data presented in this manuscript came from devices that did not undergo performance degradation during testing as verified by electrical measurements.

    c. Laser induced heating and impact on I_{ds}

    Solution) To ensure laser induced heating was prevented, we tried Raman measurements with multiple laser wavelengths (442, 488, 532 nm) at different laser power levels. 488 and 532 nm lasers were better for reducing local laser induced current as their energies are lower than 442 nm. Raman temperature conversion results were consistent when using 532 nm laser with sample incident

laser powers of 25.2 mW (as described in manuscript) and 2.4 mW. 488 nm laser with sample incident laser powers of 5 mW gave similar results as well.

2. Low V_{ds} related issues:

   a. Wrong power output reading

   Solution) Care was taken to use force-sense biasing at source and drain to account for and remove the resistance of the bias networks up to the Au wire bond leads (connected to the electrode pads), determined to be ~0.28 Ω at 85°C, so that the reported power is the actual power dissipated in the device.

6.3.2 Automation of HEMT Operation

A HEMT operating program was developed using the NI LabVIEW software. This program was targeted for fully automated device control for short-term operation as well as long-term reliability studies. Constant DC power operation was achievable with ±0.001 W precision by controlling V_{gs} at a specifice V_{ds} condition. Simultaneous operation of four devices was possible while collecting electrical data (V_{gs}, I_{gs}, R_{gs}, V_{ds}, I_{ds}, R_{gs}, power density, etc.) during testing. For long-term electrical stress tests, an automatic periodic performance check (I-V sweep) function was added. Also the program would inform the operator if certain criterions indicating device degradation, e.g., 5% power reduction for a given bias condition, were met. As provision against worst case scenarios such as unexpected device failure, emergency warning/shut-down functions were developed and implemented. The front panel of the developed program is shown in Fig. 28.

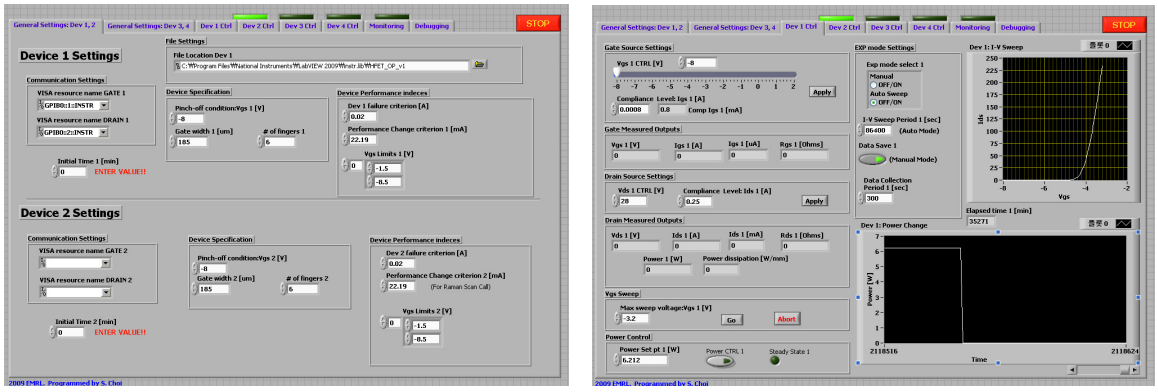

Fig. 28. LabVIEW program developed to control devices.

6.4 Results and Discussion

6.4.1 Bias Dependence of Gate Edge Temperature Observed From Conventional Raman Thermometry Methods

Under negative gate bias, a depletion region is formed beneath the gate and the sheet carrier density reaches a minimum at the drain side gate edge which in turn causes an electric field concentration. Thus power delivery by the electrons to the lattice takes place primarily in this narrow region of the channel. Among the bias conditions, i.e., combination of V_{gs} and V_{ds}, with identical power dissipation, a lower carrier concentration is achieved for bias conditions with more negative V_{gs}, i.e., higher V_{ds} at this local region under the gate since the depletion region extends further down towards the GaN layer. The requirement for current continuity results in a higher longitudinal electric field and higher carrier velocity at the gate edge near the drain. Therefore the

distribution of Joule heating within the device varies with bias conditions even though the amount of power dissipation is identical. Under high V_{ds} conditions (more negative V_{gs}), a higher portion of the applied V_{ds} drops near the drain side gate edge with remainder of the voltage dropping across the rest of the 2-DEG and at source and drain ohmic contacts. The concentration of the heat generation region results in a higher channel temperature as shown in Fig. 29. As the channel is opened by applying a less negative gate bias, the voltage drop across the channel becomes more uniform. Under conditions where the channel is fully opened (positive gate bias), there is not a strong electric field region beneath the gate electrode which results in a lower channel temperature. Operational thermal stresses at different bias conditions (compared to their corresponding pinch-off states) are shown in Fig. 30. The local channel temperature rise becomes higher at higher bias conditions. As a result, larger compressive thermo-elastic stress is induced at that location.

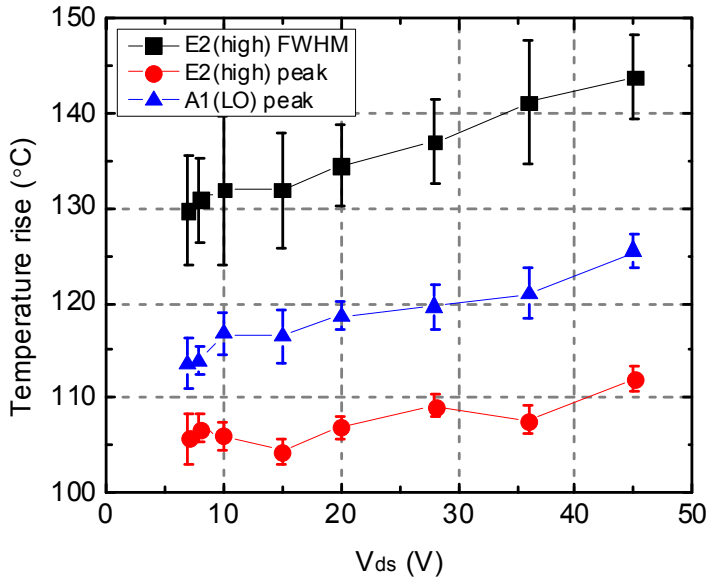

Fig. 29. Temperature at the drain end of the gate obtained from diverse Raman thermometry techniques; From the line broadening of the E_2(high) mode and from single

peak position shifts in the E_2(high) and A_1(LO) modes. The Stokes linewidth or FWHM based temperatures (black squares) represent the true channel temperatures. Considerable under-prediction is shown for the Stokes peak position based temperatures due to their stress dependence. Power dissipation levels were maintained at 10 W (4.5 W/mm) while bias conditions were varied.

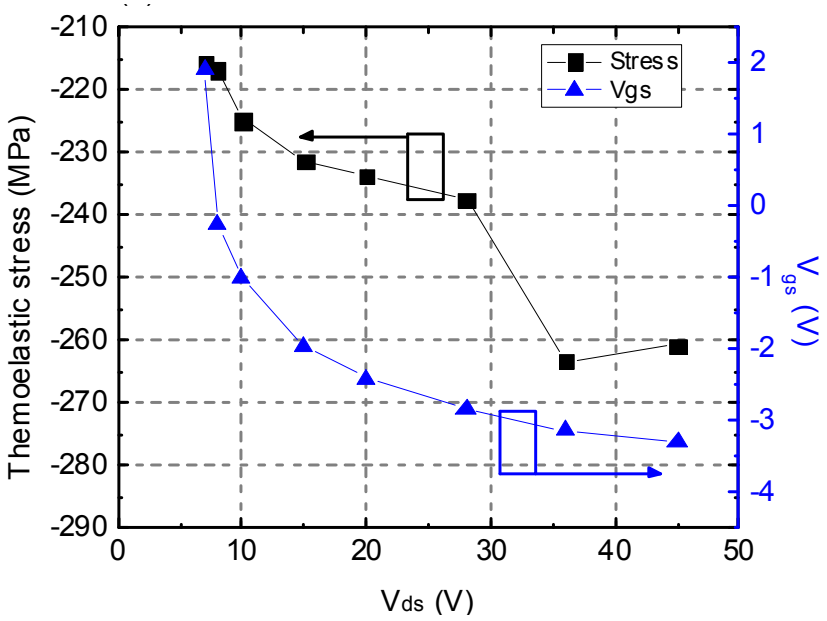

Fig. 30. Corresponding electrical bias conditions for the temperature results shown in Fig. 29. To retain the power dissipation level (10 W or 4.5 W/mm), V_{gs} was adjusted to less negative values when V_{ds} was decreased. V_{gs} is positive for V_{ds}=7 V when 10 W is dissipated. Also shown is the thermal stress induced by local temperature rise in the device. 95% confidence intervals for the stress results were ~±38 MPa of the best estimates.

Fig. 29 also shows the systematic error that comes from not properly separating the effect of mechanical stress on the Raman peak position shift to acquire temperature information. Foremost, the Stokes linewidth based temperatures represent the 'true' lattice temperatures of GaN as described in [52]. This fact was confirmed by comparing the results obtained from this method with results from the Stokes to anti-Stokes intensity

ratio based method and 3D finite-element simulation. Compressive thermo-elastic stress causes a blue-shift in the Raman frequency whereas increased temperature red-shifts it. . This results in an under-prediction of lattice temperature when performing Raman temperature measurement using only one Stokes Raman peak. The E_2(high) mode of GaN corresponds to the atomic oscillation in the c-plane which has a non-polar character. Its mode frequency is therefore more sensitive to the lattice strain in the c-plane than the A_1(LO) phonon mode which corresponds to atomic oscillations along the c-axis [12]. This was revealed in Chapter 3 (derived stress conversion coefficients). A graphical illustration of these phonon modes was given in Fig. 6. Fig. 29 shows the channel temperature extracted by the A_1(LO) peak position is closer to the 'true' channel temperature due to its lower sensitivity to mechanical stress. Utilizing line broadening of the A_1(LO) mode also gives reasonable estimates for the true lattice temperatures (not displayed in Fig. 29) but is impractical due to its large error bar range. 95% confidence intervals were ~±26°C of best estimates. Low signal-to-noise ratio of the A_1(LO) mode signal is responsible for the large error bars.

This bias dependence of the thermal resistance may promote localized damage to occur near the drain side gate edge depending on bias conditions even though thermal aging tests do not show thermal degradation occur at ambient temperatures close to operational junction temperatures predicted by conventional modeling results utilizing Fourier's law assuming the heat generation region as a uniform source along a fixed area near the gate. This bias-dependent self-heating effect should be even more pronounced for devices grown on top of Sapphire or Si substrates due to their low thermal conductivities and for devices with longer channels. When setting up experimental and

control groups for reliability test experiments to investigate certain failure mechanisms (for example, see [109] where hot electron induced degradation was examined), the effect of bias-dependent self-heating should be taken into account, i.e., one should not assume the channel temperature to be invariable among devices under different bias conditions although the amount of power dissipations are identical. Control of the electric field distribution across the channel can be performed through the implementation of source connected field plates, T-gates, etc. The reduction in the peak electric field in these devices will change the distribution of the heat generation region and may reduce the effect seen here slightly but is not expected to eliminate it. In fact, additional field plating will make the effect we have observed harder to see and may impart a false sense of security when thermal resistance measurements are made without considering the possibility of bias dependence [110].

6.4.2 Application of Linear 2-Peak Fit Method and Comparison with Electro-Thermal Simulation

Uncertainty levels ensuing from the linewidth based method were ±6°C while experimental results showed ~11°C deviation between V_{ds}=45 V and V_{ds}=7 V cases when the power dissipation was 4.5 W/mm. Raman data conversion to temperature was performed using the linear 2-peak fit method developed in Chapter 5 since this method offers lower uncertainty than the linewidth based method which would be beneficial in terms of examining not only the gate edge temperature but also the temperature distribution across the channel. Presuming that more meaningful best estimates would be

obtained from the 2-peak fit method, these results were compared with bias dependent operating temperatures obtained from electro-thermal simulation. Uncertainties (95% confidence bounds) in measured temperatures were less than ±4°C.

The temperature at the gate edge determined by Raman spectroscopy at a fully open channel condition (V_{gs}=1.92 V, V_{ds}=7 V, P=10 W) was 206.2°C. This value agrees well with the value obtained from the linewidth based method within uncertainty ranges (also temperatures for other bias conditions do agree in this sense). The temperature at this location increases as higher V_{ds} is applied even the power dissipation is kept constant as shown in Fig. 31.

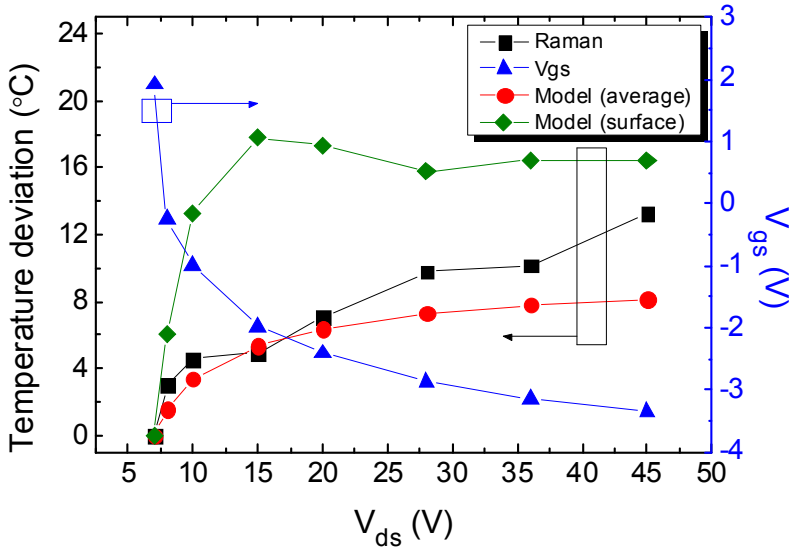

Fig. 31. Deviation of the gate edge temperature at different bias conditions from a fully open channel case (206.2°C). Also shown are tested bias conditions to retain the power dissipation level at 10 W (4.5 W/mm) and electro-thermal simulation results. Simulation results are displayed for different integration volumes (GaN peak temperature along the channel vs. its depth average). Solid lines are guides to the eye.

A coupled 3-D electro-thermal finite element model [99] was utilized to validate the

experimental results from Raman thermometry. Device heat generation primarily from Joule-heating within the 2-DEG region was obtained from a small scale 2-D electro-thermal model using ISE Sentaurus Device by solving hydrodynamic equations for electron transport and the thermal diffusion equation for heat transport. This coupled solution was then linked to a large scale 3-D thermal model solving the thermal diffusion equation using ANSYS. To mimic the Raman measurement and enable a realistic comparison, the model data was averaged over the first 0.5 μm of channel optically visible and through the thickness of the GaN. Excellent agreement with experiments at low bias conditions in Fig. 31 gives confidence to the selected modeling parameters. Hot phonon build up at high bias states may have caused the deviation between simulation and experimental results since such nanoscale thermal physics was not included in the model. Resulting trends of the gate edge temperature are consistent with former observations revealed by thermoreflectance CCD imaging [33] and by using a similar experimental approach for two operating conditions (V_{ds}=25 and 50 V) [106]. Similar bias dependent trends were observed at other locations on this device and for other devices. This bias dependence of operating temperature was consistently observable throughout the active region of the device. Close to the edge of the channel farthest from the device center, the temperature rise at V_{ds}=7 V was 82.5°C whereas V_{ds}=45 V resulted in a temperature rise of 90.5°C.

As the channel is opened by applying a less negative gate bias, the voltage drop becomes more uniform across the channel. Under conditions where the channel is fully opened (positive gate bias, e.g., V_{gs}≈2 V), there is not a strong electric field region beneath the gate electrode. This results in a lower channel temperature and lower

temperature gradient across the channel. Electric field concentration near the drain side corner of the gate at high V_{ds} conditions reveals itself as higher channel temperature and larger inverse piezoelectric stress induced near this region [87]. The results for the foregoing discussion are shown in Fig. 32. Details of simulation results regarding electric field distribution, temperature distribution, and heat generation rate along the channel can be found in [110].

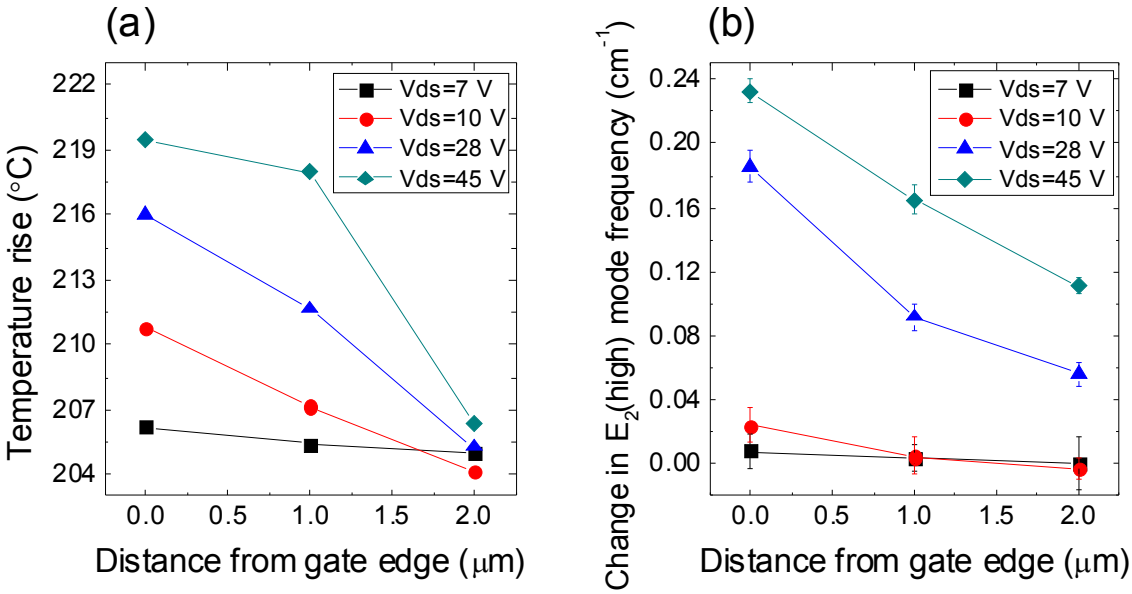

Fig. 32. (a) Temperature at measured locations between the gate and drain for representative bias conditions. (b) Change in E_2(high) phonon frequency at pinch-off conditions (V_{gs}=-8 V) from the unbiased state. Larger shift in phonon frequency at higher V_{ds} conditions indicates larger compressive in-plane stress induced by the inverse piezoelectric effect. Measurements were taken at 25°C. Solid lines in the graphs are guides to the eye.

The peak lattice temperatures are expected to be much higher than values obtained by Raman spectroscopy using sub-band gap laser excitation since this probes the depth-average temperature of the GaN layer whereas the hot spot dimension is on the order of

10-100 nm [25], [26]. For this same reason it is also believed that a lower bound for the magnitude of the bias dependence of the thermal resistance was observed in this work. When setting up experimental and control groups for reliability tests to investigate certain failure mechanisms, the effect of bias-dependent self-heating should be taken into account. One should not assume the channel temperature to be invariable among identical devices under different bias conditions even though the total power dissipation is identical. While the amount of bias dependence to the channel temperature is expected to vary with channel and epi-stack dimensions, substrate choice, total power, etc., and the intent here is not to be exhaustive, the bias dependence of the channel temperature reported in this study leads to MTTFs that can differ by about an order of magnitude for a commonly reported thermal activation energy of ~ 2 eV [111]. In addition, very careful and low noise measurements or electro-thermal modeling (not just thermal and based on a fixed heat generation region) are required to quantify this effect.

6.5 Summary and Conclusions

The bias-dependent self-heating was examined from a thermal analysis using micro-Raman thermometry. Under bias conditions where V_{ds} is higher and V_{gs} is more negative, the heat generation region becomes more concentrated into a nanoscale region under the drain end of the gate electrode. Consequently a higher channel temperature results compared to that for conditions with lower V_{ds} and less negative V_{gs} even though the total power dissipation in the device is identical. This effect exerts local peculiarity in the device and should be taken into account in fundamental reliability studies and

implementation of AlGaN/GaN HEMTs.

CHAPTER 7

THE IMPACT OF STRESS ON THE DEGRADATION OF ALGAN/GAN HEMTS

7.1 Summary

Coupled 2-D electro-thermo-mechanical simulation and Raman thermometry were utilized to analyze the evolution of mechanical stress in AlGaN/GaN high electron mobility transistors (HEMTs). This combined analysis was correlated with electrical step stress tests to determine the influence of stress on the degradation of actual devices under diverse voltage bias conditions. It was found that the total stress as opposed to one dominant stress component correlated the best with the degradation of the HEMT devices. These results suggest that minimizing the total stress as opposed to the inverse piezoelectric stress in the device is necessary in order to avoid device degradation that can be accomplished through various growth methods.

7.2 Introduction

There have been significant advances in the development of novel wide bandgap III-V compound semiconductor devices in recent years. This is especially true for GaN based amplifiers, i.e., AlGaN/GaN high electron mobility transistors (HEMTs), which breakdown at far higher peak electric fields compared to GaAs and Si used to build

modern solid state devices. This allows power switches and RF amplifiers to operate at higher voltages and power densities, thereby simplifying circuit design, reducing system weight, and improving efficiency. AlGaN/GaN based HEMTs have demonstrated superior performance and are available in the marketplace commercially. However, a physical understanding of the various reliability limiting mechanisms is lacking in subject literature and is a topic of debate in the GaN community. For example, the role and relative contribution of the various intrinsic material factors, such as physical stress and strain has not been clearly understood.

Intensive efforts have been made to reveal the degradation mechanisms of these devices operating under diverse electrical bias conditions. Approaches have included simulations using coupled multi-physics simulations [112], [113] and electrical testing [8], [114] along with surface science or electron microscopy [7], [115].

In considering electrical testing of devices in the OFF-state it was reported that the inverse piezoelectric effect drives a degradation or failure mechanism as a result of the peak electric field forming in a device exposed to high voltage bias [8], [116], [117]. It was postulated that the field induced tensile strain in the AlGaN layer leads to formation of electronic traps and/or mechanical damage in this layer, especially, near the drain side corner of the gate. This study was extended to relate this field-driven degradation to structural (gate and channel geometry) [118] and thermal effects [119]. The previously mentioned studies imply that mechanical stress is involved in the relevant degradation modes of the devices [8], [48], [18]. In AlGaN/GaN HEMTs, the brittle AlGaN layer is pseudomorphically grown on a thick GaN buffer and thus possesses high tensile stress.

This makes this layer susceptible to mechanical failure when exposed to additional tensile loads [120] induced from different physical origins.

Stress or strain induced in operating AlGaN/GaN HEMTs are a superposition of the following physical effects (assuming linear elastic deformation). Residual stress is inherently present in these heteroepitaxialy grown devices where its magnitude depends on the substrate material, processing details, and any patterning of the devices [121]. As AlGaN/GaN HEMTs are aimed for high power applications, the high voltage bias conditions induce the inverse piezoelectric stress effect in the GaN and AlGaN layers due to their high ionicity and non-centrosymmetric nature. This effect is especially pronounced near the drain side corner of the gate where a peak vertical electric field along the c-axis is formed. In operating devices (ON-state), temporally and spatially nonuniform self-heating results in a large temperature gradient across the channel and within the device leading to occurrence of thermo-elastic stress. While there are three major components of stress (residual, inverse piezoelectric, and thermo-elastic), it is not clear if one of these stress components dominates the degradation of the devices or if there is simply a critical value of total stress that must be obtained in order to see device degradation.

In this work, we investigate the impact of stress on the degradation of AlGaN/GaN HEMTs grown on Si and SiC. Through the use of coupled electro-thermo-mechanical simulation and Raman spectroscopy, the totals stress and magnitudes of each stress component were determined. The stress measurements and calculations were correlated with electrical characterization of the devices to determine its role in device degradation.

7.3 Experimental

7.3.1 Device Description

Six-finger AlGaN/GaN HEMT test structures fabricated on a 100 μm thick 6H-SiC substrates via metal organic chemical vapor deposition (MOCVD) were investigated. The AlGaN/GaN heterostructure composed of a 2 μm thick GaN layer and an unintentionally doped AlGaN barrier layer [122]. Processing technology was similar to that described in [108]. Devices employed standard Schottky and ohmic contacts. Silicon nitride passivation was deposited by low temperature plasma enhanced chemical vapor deposition (PECVD). The gate length and width were 0.5 μm and 370 μm, respectively. Devices employed a gate field plate (GFP) or T-gate. It should be noted that these test devices did not employ source connected field plates (SCFP), one of the main features distinguishing them from relevant commercial devices, for the purpose of degradation study. For the current test structures, larger internal electric fields [20], [123] as well as higher peak channel temperatures [124] are expected to occur that would render devices more prone to degradation compared to optimized commercial parts. Nonetheless, the impact of stress on device degradation can still be determined through the use of these test structures. The distance between the GFP edge and drain was ~3 μm. Fig. 33 illustrates an abbreviated cross-sectional schematic of the investigated devices (only one channel displayed). Experimental as well as computational analysis was performed to assess the role of total stress occurring in the AlGaN 'critical region' shown in Fig. 33 for different device structures.

GaN-on-Si devices from [125] were also studied, having a similar 2-D cross-sectional geometry or dimensions as the GaN-on-SiC devices except employing a SCFP (Fig. 33). The GaN-on-Si devices had a gate to drain spacing of 3 μm and gate length of 0.5 μm similar to those for the GaN-on-SiC devices. The gate to source distance and the AlGaN composition were also similar for both of the devices grown on Si and SiC.

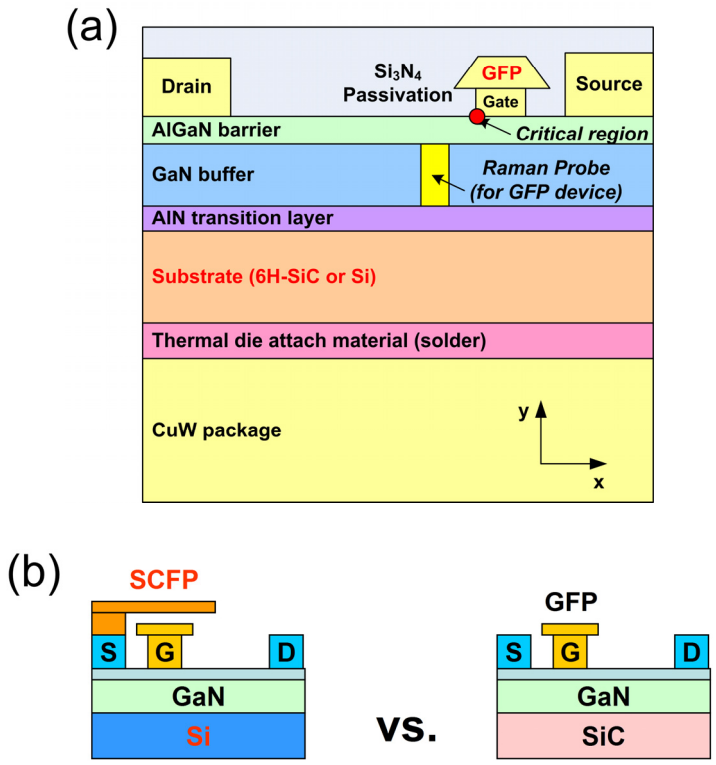

Fig. 33. Schematic of examined AlGaN/GaN HEMTs. Dimensions are not in scale. (a) Raman measurements were performed at a location closest to the drain end of the gate where optical access was allowed. The AlGaN surface under the drain side corner of the gate was investigated via simulation as this location is the critical region where peak stress values are induced. The y-axis in was taken to be parallel to the growth direction (c-axis) and pointing from the N-face towards the Ga-face of the GaN layer. The x-axis was taken parallel to the length direction of the device channel. (b) Two type of devices were investigated. The devices from [125] employed a Si substrate and SCFP (left). The GaN-on-SiC devices did not have a SCFP structure (right).

7.3.2 V_{ds}-step stress tests

To test the response of devices to electrical stress testing, tests were performed in both the ON-state and OFF-state. To be closer to real device operating conditions, the primary variable in the electrical step stress tests [8] was drain-source voltage (V_{ds}) rather than applying very large negative values of V_{gs} to induce localized electric field concentration. The GaN-on-SiC devices were stressed at pinch-off conditions (V_{gs}=-8 V, V_{ds}=28/48/84/105/144 V) as well as ON-state (P=4.5 W/mm, V_{ds}=28/48/60/70/75 V) at various V_{ds} levels. The highest stress voltage (V_{ds}=144 V) was selected to be three times of the nominal operating voltage for relevant commercial devices. Performance degradation was tracked using a benign post stress electrical characterization procedure similar to that described in [8] to monitor degradation through gate leakage current, transconductance I_{dmax}, and I_{dss} [8]. All tests were conducted in a dark environment. The baseplate temperature (T_{base}) for OFF-state stress tests was 25 °C. For ON-state stress tests, T_{base} was set to 85 °C to raise the overall device channel temperature to pronounce thermo-mechanical effects. Devices were stressed for prolonged periods, at least 20 hours for each step condition, to take into account of the time-dependent behavior of AlGaN/GaN HEMTs undergoing the high field induced degradation [126].

7.3.3 Micro-Raman Spectroscopy

Raman spectroscopy measurements were conducted using a Horiba Jobin Yvon LabRAM HR800 spectrometer equipped with a 532 nm diode-pumped solid-state laser

excitation source. The frequency shifts in the GaN E_2(high) and A_1(LO) modes were investigated. The laser power incident on the samples was adjusted to 25.2 mW for GaN-on-SiC devices and 2.4 mW for GaN-on-Si devices, respectively, to prevent laser induced heating, especially due to respective substrate materials. Since a sub-bandgap visible laser was utilized, the obtained signals represent a volumetric average value across the beam spot (diameter was ~1 μm) and through the entire thickness of GaN.

To estimate the residual stress in the AlGaN layer, Raman measurements were performed on the GaN-on-SiC devices as well as GaN-on-Si devices studied in [125] to quantify the GaN residual stress in each device type [121] at room temperature (25 °C). Also GaN residual stresses at the elevated baseplate temperature (85 °C) for ON-state tests were quantified using the Raman method suggested in [124]. Here the GaN residual stress is presumed to be biaxial in the c-plane which is a reasonable assumption for a thin epitaxial layer clamped on a much thicker substrate. The in-plane strain ε_a in the GaN layer is determined based on the a-lattice constant (a_{GaN}) and the strain-free a-lattice constant of GaN ($a_{GaN,0}$=3.1878 Å [57]) as seen in (16):

$$\varepsilon_a = (a_{GaN} - a_{GaN,0}) / a_{GaN,0} \tag{16}$$

The biaxial stress is related to the in-plane strain ε_a by Hooke's law.

$$\sigma_a = Y\varepsilon_a \tag{17}$$

where the biaxial modulus Y is defined as

$$Y = C_{11} + C_{12} - 2C_{13}^2 / C_{33} \tag{18}$$

The elastic stiffness constants of GaN can be found in [67] [121]. In-plane a-lattice constants of the device GaN layers were estimated from the stress measurements via Raman spectroscopy along with (16)–(18).

The thin AlGaN layers were pseudomorphically grown on the GaN/substrate template. Thus it is reasonable to assume the AlGaN a-lattice constant is the identical as that for the GaN layer ($a_{AlGaN} = a_{GaN}$). The ideal room temperature strain-free lattice constant ($a_{AlGaN,0}$) of $Al_xGa_{(1-x)}N$ was determined to be 3.1670 Å using Vegard's law based on the AlGaN composition (x=27% Al) and the strain-free a-lattice constants of GaN ($a_{GaN,0}$=3.1878 Å [57]) and AlN ($a_{AlN,0}$=3.1106 Å [59]).

$$a_{AlGaN,0} = x \cdot a_{AlN,0} + (1-x) \cdot a_{GaN,0} \tag{19}$$

The resultant intrinsic in-plane elastic strain in the AlGaN layer was determined by

$$\varepsilon_{a,AlGaN} = (a_{GaN} - a_{AlGaN,0}) / a_{AlGaN,0} \tag{20}$$

Finally, the residual stress in the AlGaN layer was calculated using (17) with the elastic stiffness coefficients of AlGaN (C_{11}=393.4 GPa, C_{12}=142.5 GPa, C_{13}=104.7 GPa, and C_{33}=395.2 GPa) estimated by linear interpolation between GaN [67] and AlN [127] elastic stiffness matrices.

In addition to the residual stress measurements, the devices were characterized via Raman spectroscopy to determine the channel temperature and operational thermo-elastic stress. This was performed to see the validity of the 2-D electro-thermal simulation. The laser probe was located at the drain side edge of the GFP at the midpoint of the device where the temperature was expected to be highest in the ON-state. Device output powers were controlled between 0.57 and 5.27 W/mm at fully open channel conditions (V_{gs}=2.55 V, V_{ds}=2–8 V). The device base temperature was maintained at T_{base}=85 °C using a temperature controlled stage. To convert the Raman signals to thermal stress and temperature, a method introduced in [124] and [53] was used.

7.4 Modeling

The main purpose of the computational analysis was to quantify the thermo-elastic and inverse piezoelectric stresses induced in the AlGaN barrier under the drain side corner of the gate for different HEMT structures subject to diverse bias conditions. These physical quantities are not observable using Raman spectroscopy (utilizing visible laser) due to the limitation in optical access and the weak signal intensity of AlGaN. Combined with the AlGaN residual stress estimated from Raman stress measurements, the total stress at the 'critical region' in each type of device was derived.

First, 2-D electrostatic potential distributions and heat generation profiles within AlGaN/GaN HEMTs subject to different bias conditions were obtained using a hybrid electro-thermal model [99]. This model was built using a combination of the ISE Sentaurus Device software package [128] and ANSYS [129]. Hydrodynamic equations

for electron transport were fully coupled to the diffusion equation for conduction heat transfer. The model adopted realistic geometries for all metal and passivation layers in the channel as were seen in transmission electron microscopy images for representative devices from the same process, including accurate values of radii of curvature at the corners of all metal layers facing the channel, including the gate metal. This is a crucial point in order to mitigate localized singularities in the solution near sharp edges, and also critical for extracting quantitative values for the electric field close to corners. Simulation parameters were validated by comparing I-V and other DC characteristics with those for actual devices. Further details of this coupled electro-thermal model can be found in [99].

The electrostatic potential and heat source results from the electro-thermal model [99] were then linked to a 2-D coupled electro-thermo-mechanical model developed using COMSOL Multiphysics [130]. Electrical and mechanical physics were one-way coupled thus secondary strain-induced alteration in the electrical characteristics (piezoelectric polarization field) of the device were not considered. Structural and temperature dependent thermal material properties were employed [131] in this model. Material properties for AlGaN were determined via linear interpolation (Vegard's law) between its binary constituents GaN and AlN as a function of mole fraction except where deviations are significant, such as for the thermal conductivity (k=30 W/mK) [100], bandgap, and carrier mobility, etc. [127]. Structural and thermal properties of AlN reported in [127] and [60] were employed. The thermal conductivity of this defective transition layer was deduced from the effective thermal boundary resistance measured in [102] rather than using a value corresponding to bulk single crystalline AlN (k=285 W/mK). Silicon

properties were adopted from [132], [133], and [134]. The piezoelectric coupling matrices and permittivity tensors for relevant materials are listed in Table 5.

Table 5. Electrical properties of materials.

Material	Permittivity matrix			Piezoelectric coefficients (C/m^2)			
	ε_{11}	ε_{33}	Reference	e_{15}	e_{31}	e_{33}	Reference
GaN	8.6	10.5	[135]	-0.41	-0.47	0.84	[135]
AlN	9	9.5	[127]	-0.32	-0.6	1.34	[127]
$Al_{0.27}Ga_{0.73}N$	8.71	10.23	[135], [127]	-0.386	-0.505	0.975	[135], [127]
6H-SiC	9.66	10.03	[136]	-0.198	-0.2	0.398	[137]
Si	11.7			-	-	-	

In order to prevent potential errors caused by simplified model geometry [138], [87], the electro-thermo-mechanical model did not include only the chip itself but also considered the device module up to the device package. It should be noted that this coupled continuum scale analysis does not include failure analysis but only calculates the magnitude of the mechanical stresses induced by the internal (vertical) electric field and temperature gradient within the elastic deformation regime. For clarity, the coupled modeling scheme is illustrated in Fig. 34.

To validate the thermo-mechanical results, the simulation results for the GaN layer were compared with those resulting from the Raman thermometry measurements.

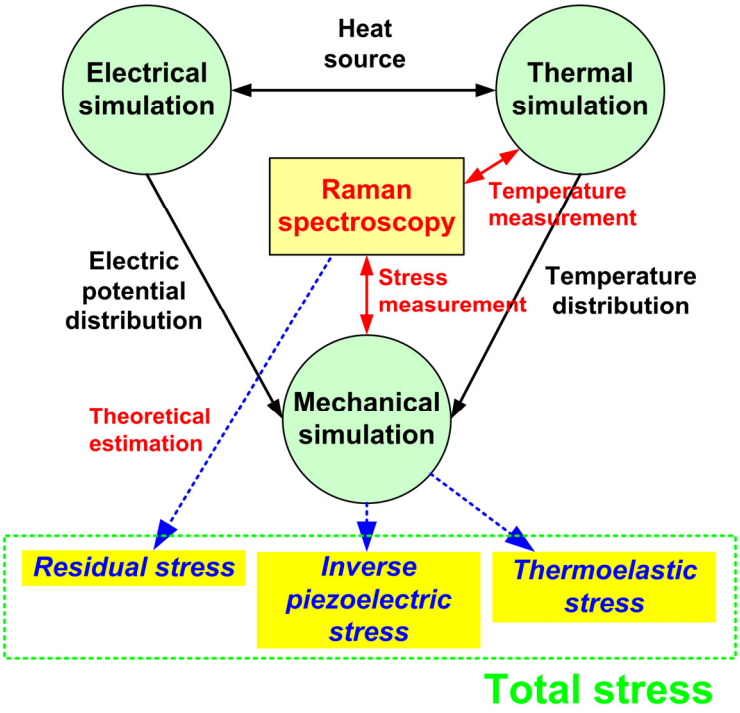

Fig. 34. The approach method used to quantify the total stress in the AlGaN layer under the drain side corner of the gate.

7.5 Results and Discussion

7.5.1 Electrical Step Stress Tests

As shown in section 7.3.2, electrical stress tests in the current work were performed under harsh conditions (high V_{ds}) compared to previous studies [8], [125] to enforce the devices to degrade and relate results to the computational mechanical stress analyses. Notably, virtually no field-driven permanent performance degradation [8] took place in the GaN-on-SiC 6-finger HEMTs (no SCFP implemented) up to a V_{ds} of 144 V for OFF-

state stress tests. In contrast to these results, devices employing Si substrates underwent electrical degradation during OFF-state step stress tests where the critical V_{ds} ranged between 35 and 75 V [125]. The GaN-on-Si devices had similar cross-sectional geometry with the devices tested here but employed SCFPs that would further suppress the peak electric field strength [139], [20]. A typical result for the GaN-on-SiC device where degradation was minimal is shown in Fig. 35 (a). No remarkable changes in gate leakage current, peak transconductance, I_{dmax}, I_{dss} R_{on}, and threshold voltage were observed. Interestingly, at this stress condition (V_{ds}=144 V), induction of a larger tensile inverse piezoelectric stress is expected to occur compared to that formed in the GaN-on-Si devices [125] exposed to the critical bias conditions (V_{ds}=35–75 V) mentioned above.

For ON-state stress tests (P=4.5 W/mm), sudden performance degradation showing typical features described in [8] consistently took place in the tested GaN-on-SiC devices when V_{ds} was stepped up to relatively low values ranging from 70 to 75 V. A representative result is displayed in Fig. 35 (b) where an increase in off-state gate leakage current by an order of magnitude is observed.

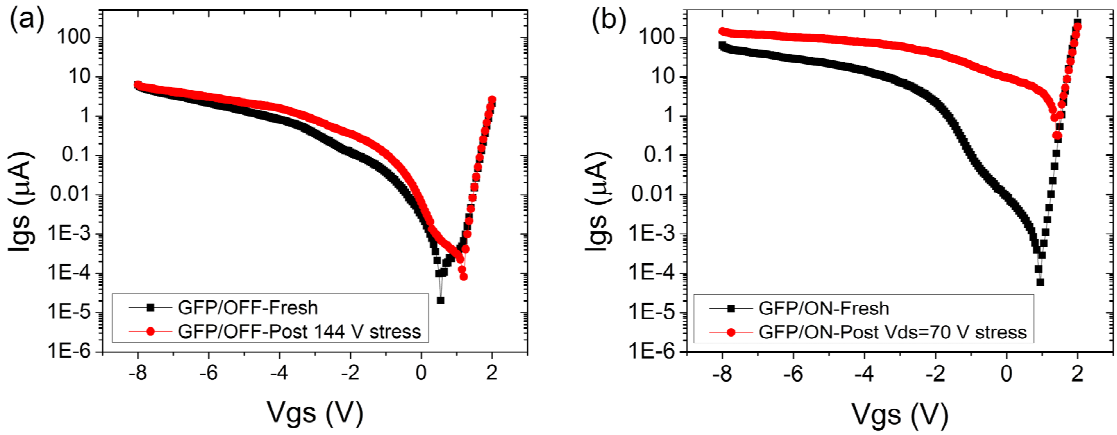

Fig. 35. Gate current characteristics measured before and after V_{ds} step stress experiments for representative electrical stress conditions. Here V_{gs} was swept from -8 to

2 V while V_{ds} was kept at 5 V. Change in device characteristics after pinch-off state (V_{gs}=-8 V) stressing at V_{ds}=144 V is shown for a GaN-on-SiC device in (a). (b) illustrates the change in performance of a GaN-on-SiC device after ON-state stressing (V_{gs}≈-3.58 V, V_{ds}=70 V, P=4.5 W/mm).

7.5.2 Impact of the Inverse Piezoelectric Stress

2-D Electro-mechanical simulations were performed to quantify the magnitude of inverse piezoelectric stress occurring in devices. First, a structure based on the actual GaN-on-SiC device only having a GFP was examined. Then a structure representing the GaN-on-Si devices studied in [125] was constructed by including a SCFP in addition to the GFP structure. The two device types were compared in terms of maximum inverse piezoelectric stress induced in the AlGaN layer. Devices were under pinch-off (V_{gs}=-8 V), T_{base}=25 °C and the electrical stress factor V_{ds} was increased from 28 V to 120 V.

The electrical simulations confirmed that field plates (GFP as well as SCFP) relieve the maximum vertical electric field strength that occurs in the AlGaN compared to no field-plated cases (results not displayed). The peak values all occurred near the drain side gate edge labeled as the ‘critical region’ in Fig. 33. Redistribution of the electric field was observed for field plated structures accompanied by reduction in the maximum field value. For identical voltage bias conditions, both the peak values of lateral and vertical components of the electric field were lowest in magnitude for the GaN-on-Si device employing a SCFP [125]. Electric field results were qualitatively as well as quantitatively similar to those shown in [140]. Fig. 36 illustrates the peak vertical electric field and inverse piezoelectric stress induced in the AlGaN layer where these maximum values

occur at the surface of the AlGaN barrier layer under the drain end of the gate, i.e., the 'critical region' depicted in Fig. 33. Here and in the following analysis we focus on the x-direction normal stress component σ_{xx}. The direction of this stress component is perpendicular to the extension of the AlGaN surface cracks reported in [116] aligned under the gate edge throughout the entire channel width along the gate metal edge that formed after conducting stress tests where V_{ds} values were beyond the critical value [8].

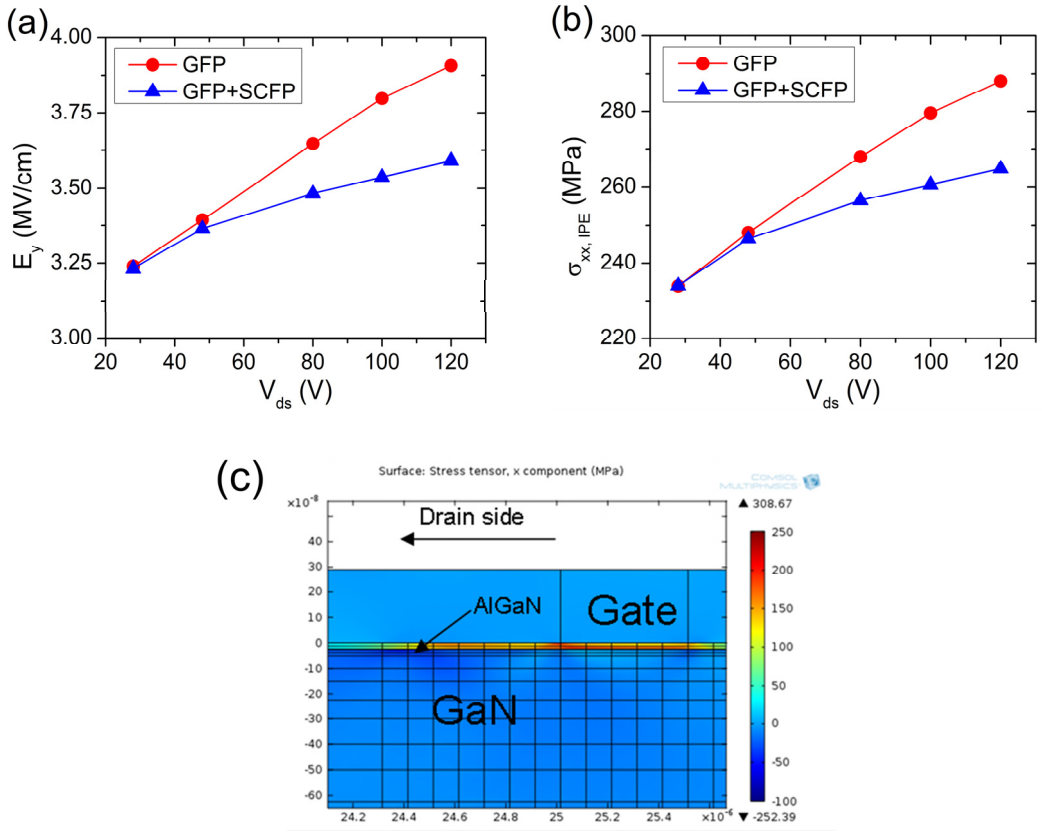

Fig. 36. (a) Maximum vertical electric field strength and (b) tensile inverse piezoelectric stress induced in the AlGaN barrier for different device structures. 'GFP' device refers to the GaN-on-SiC devices whereas 'GFP+SCFP' represents the GaN-on-Si devices from [125]. Solid lines are guides to the eye. (c) Simulation result for the GaN-on-SiC device showing the normal stress component (with a direction in parallel to the gate length) induced by the vertical electric field in the device for a test condition of V_{gs}=-8 V and V_{ds}=28 V (OFF-state).

Difference in AlGaN/GaN quality or trap density between two device types was not rigorously considered in the simulation. However, the actual peak field magnitude would be lower in the GaN-on-Si devices compared to the GaN-on-SiC devices for identical voltage bias conditions since SCFPs were implemented and higher native trap density is expected in the AlGaN barrier under the gate [141]. Therefore, a conservative comparative analysis was developed by referring to the simulation results shown in Fig. 36. It is expected that the maximum inverse piezoelectric stress induced in the GaN-on-SiC devices (having only GFP) biased under high voltages (120 V) would be significantly larger than the corresponding stresses induced in the GaN-on-Si devices [125] biased under their critical V_{ds} conditions (35–75 V). This fact reflects that by solely considering the inverse piezoelectric stress, it is difficult to explain the reason why all measured GaN-on-SiC devices withstood the field induced degradation at OFF-state up to the highest voltage supplied. Even though the role of other degradation assisting mechanisms cannot be overlooked, in a mechanics point of view, it seems worthy of pursuing investigation regarding the role of total stress induced in the AlGaN barrier instead of solely considering the inverse piezoelectric stress. Other contributors that would constitute the total stress in the AlGaN layer are the pre-existing residual stress and the operational thermelastic stress.

7.5.3 The Role of Substrate Induced Residual Stress

It was revealed from Raman measurements that the GaN layer of the 6-finger GaN-on-SiC devices possessed compressive residual stress with an average value of -199±50 MPa at room temperature. These devices did not undergo performance degradation even after harsh V_{ds} (=144 V) OFF-state step stress experiments (Fig. 35).

In [114], AlGaN/GaN HEMTs grown on SiC substrates (no SCFPs implemented) also did not exhibit standard degradation features driven by the inverse piezoelectric effect after pinch-off state step stress tests even though V_{ds} was increased close to device breakdown voltages (100 V). This is consistent with the observations in the current work. The GaN residual stress of the devices used in [114] were examined via Raman spectroscopy and turned out to be similar (-147±24 MPa) to the residual stress in the GaN-on-SiC devices studied here. It was also observed that within our available in-house device pool, randomly selected devices with various channel numbers and length configurations built on compressively stressed GaN from different wafers and lot runs had relatively high critical drain-source voltages (over 80 V) compared to devices with GaN layers having tensile residual stress or did not exhibit the inverse piezoelectric effect driven degradation features [8] up to our test limits. Admittedly, a complicating factor is that different growth processing steps or the use of different substrate/transition layer materials would result in different AlGaN/GaN quality or trap density.

Raman stress measurements [121] were conducted on a number of devices studied in [125] that had a critical drain to source voltage of ~45 V. The average GaN residual stress of these devices was 478±76 MPa (tensile). Both the lattice (not a major contributor) and

thermal mismatches between GaN and Si lead to a high tensile stress in the GaN epilayer as a result of post-growth cooling even though a buffer layer is implemented [56]. The lattice constants of AlGaN are smaller than those of GaN. Therefore, a larger in-plane tensile strain resulted in the AlGaN layer of the GaN-on-Si devices studied in [125] compared to the GaN-on-SiC devices.

Similar degradation in Si-based AlGaN/GaN HEMTs was frequently reported in literature, including [125] and [140], although to be sure it is possible to have high breakdown voltages for latest GaN-on-Si devices with optimized design [142]. In-house GaN-on-Si 10-finger AlGaN/GaN HEMTs shown relatively low critical voltages [8], for example, 28 V, for OFF-state stress tests. The mean value for the GaN residual stress of these devices was 470±76 MPa (tensile), determined from Raman measurements [121].
The room temperature residual stress values in the GaN and AlGaN layers of the tested GaN-on-SiC and GaN-on-Si devices from [125] are displayed in Fig. 37. The residual stresses in the AlGaN layers were calculated based on the measured GaN residual stresses following the procedure introduced in section 7.3.3. Total stresses at the AlGaN 'critical region' regarding two representative conditions for the GaN-on-SiC (no degradation at high voltage bias, V_{ds}=120 V) and GaN-on-Si [125] (onset of degradation, V_{ds}=45 V) devices is displayed in the first and third columns of Fig. 39. It is clearly seen that the magnitude of the total stress at the AlGaN 'critical region' (refer to Fig. 33) is dominated by the AlGaN residual stress rather than the electric field induced stress. Thus, it is likely that the substrate induced residual stress in the AlGaN layer plays a critical role in determining the device behavior in response to high voltage biasing.

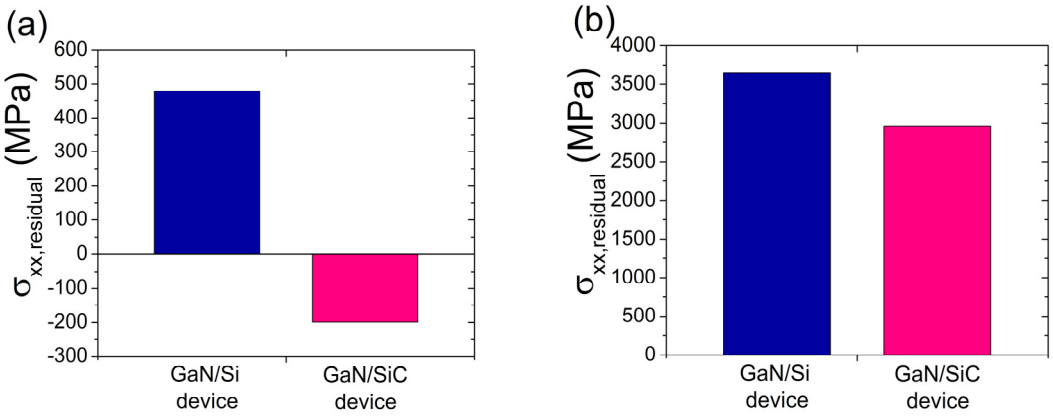

Fig. 37. (a) Room temperature residual stress values in the GaN layers of different devices measured via Raman spectroscopy. (b) AlGaN residual stresses estimated based on the GaN residual stresses.

7.5.4 Thermal Stress Effects

It was shown in previous studies that the operational thermo-elastic stress in the GaN layer under the conductive channel is compressive due to local thermal expansion hindered by the colder regions outside of this heat generating domain [48]. Therefore one may expect the thermo-elastic stress to counterbalance the tensile inverse piezoelectric stress in the AlGaN layer during operation thus devices would be less prone to the inverse piezoelectric effect driven degradation [8] at ON-state conditions [138]. However, a number of reports including [143] demonstrated contrary results to this. References [115] and [119] reinforce the idea that devices may become more likely to experience mechanical damage in the AlGaN layer during high power dissipating situations under sufficiently high bias conditions.

Detailed analysis was performed considering the AlGaN layer using the 2-D electro-thermo-mechanical simulation described in section 7.4. It was found that a large tensile stress or strain along the channel length (x-) direction arises at ON-state conditions in the AlGaN surface right under the drain side corner of the gate mainly due to the thermal expansion coefficient mismatch between the gate metal (Au: 14.2×10^{-6} /K) and AlGaN layer (4.34×10^{-6} /K). As a result, an overall increase in the tensile stress is induced at this location.

To test this finding under simplified fully open channel conditions [124] and ensure the quantitative validity of the stress results obtained from simulation, Raman temperature and stress measurements were conducted on the 6-finger GaN-on-SiC devices. Devices were powered under fully open channel (V_{gs}=2.55 V) at low drain biases (V_{ds} = 2–8 V) as described in section 7.3.3. Raman measurements were taken at the midpoint of the center channels close to the drain side GFP edge. Results were compared with simplified 3-D FEA thermo-mechanical simulation [131], [101] as well as the 2-D simulation used in the current work. To make direct comparison with the Raman results, the modeling data were volume averaged through the entire thickness of GaN similar to the Raman laser probe. Excellent agreement between the experimental results and the 3-D simulation in Fig. 38 gives confidence to the selected modeling parameters. The 2-D modeling results which accounted for 3-D heat spreading effects through the use of solder/package temperature boundary conditions also shown reasonable agreement with results from the other two methods. The overall close agreement among three methods gives credibility to the quantitative analysis performed on the AlGaN layer using 2-D simulation. Though a large tensile stress is observed in the AlGaN near the

gate/AlGaN interface, away from the gate edge and going into the GaN layer, the thermo-elastic stress becomes compressive as expected [48].

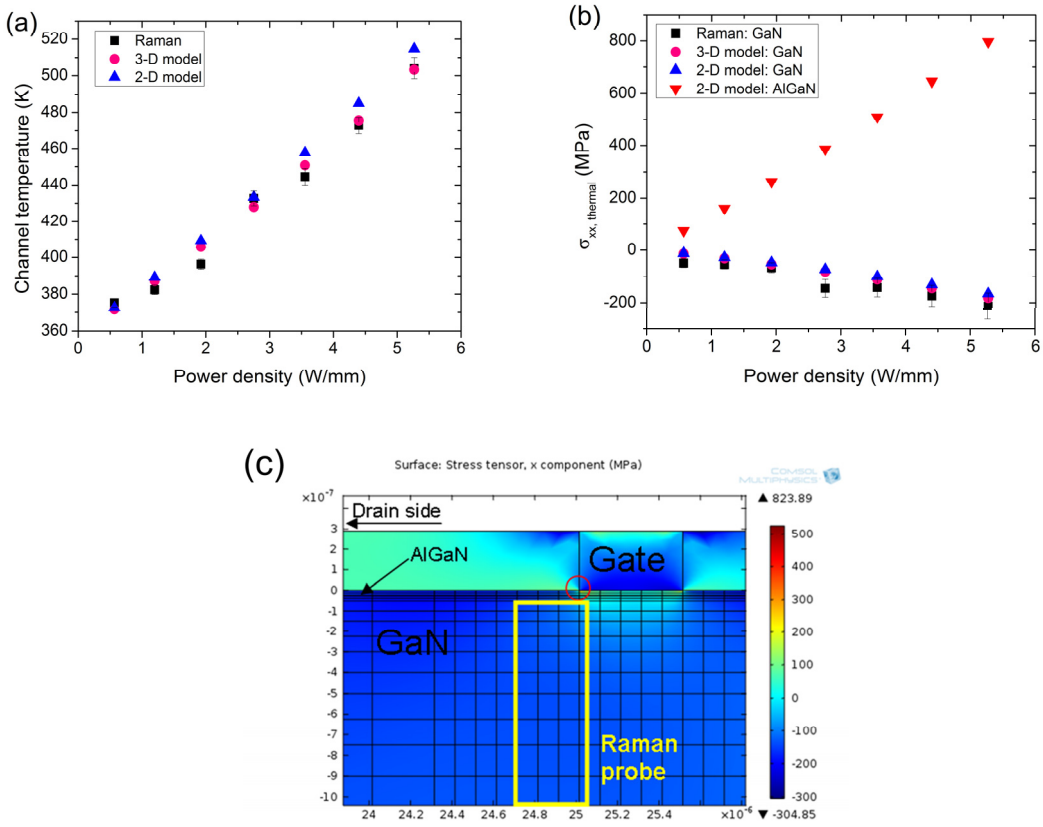

Fig. 38. Model validation of the thermo-mechanical results through the use of Raman spectroscopy measurements. (a) Channel temperature in the GaN layer at various power conditions deduced from thermal simulation as well as Raman thermometry. (b) Operational thermo-elastic stress induced at diverse power conditions. Raman results represent the through thickness average values in the GaN layer. Also shown is the thermal stress at the AlGaN 'critical region' (refer to Fig. 33) deduced from 2-D thermo-mechanical simulations. (c) 2-D simulation results for the thermo-elastic stress induced under operating conditions of V_{gs}=2 V (fully opened channel), V_{ds}=80 V and P=4.5 W/mm. The AlGaN 'critical region' is indicated by the red circle under the drain side gate edge. Data averaging was performed within the domain illustrated as the 'Raman probe' to compare with thermal stress measured via Raman spectroscopy.

7.5.5 Total stress analysis (Pinch-off state vs. ON-state)

Finally analysis regarding the total stress at the AlGaN 'critical region' (Fig. 33) was conducted involving electrical bias conditions where real devices experienced degradation (case 2 and 3) except for case 1 described below regarding the GaN-on-SiC device electrically stressed under pinch-off. The four conditions are summarized in Table 6. Case 3 (third column in Fig. 39) was chosen as a representative condition where the onset of inverse piezoelectric effect driven degradation [8] took place in the GaN-on-Si devices (SCFP implemented) [125] under pinch-off. To assess the role of substrate induced residual stress under pinch-off state, case 1 (GaN-on-SiC device) was selected for the purpose of conservative comparison in terms of the inverse piezoelectric stress where the applied V_{ds} was much higher than that for case 3 and a SCFP was not employed. For this case, degradation features were not observed in the electrical stress tests. Case 2 refers to a condition where the onset of degradation took place at relatively low V_{ds} (70–75 V) during ON-state step stress tests for the GaN-on-SiC test structures. From this case we attempt to see the contribution of operational thermo-elastic stress to performance degradation. As a result of the harsh bias condition [124] and high baseplate temperature (85 °C), the estimated device channel peak temperature (T_{ch}) for the GaN-on-SiC test structure (case 2) was beyond the safety limit for a relevant commercial device. Case 4 was not physically tested but was computationally studied to see the substrate material effect on the maximum total stress in the AlGaN layer of the GaN-on-Si device dissipating identical power as in case 2.

Table 6. Description of analyzed devices and bias conditions.

Case	Device	GFP	SCFP	State	V_{ds}(V)	P(W/mm)	T_{ch}(°C)	Degradation
1	GaN/SiC	Yes	No	Pinch-off[a]	120	0	25	No
2	GaN/SiC	Yes	No	ON[a]	75	4.5	250.6	Yes
3	GaN/Si	Yes	Yes	Pinch-off[a]	45	0	25	Yes
4	GaN/Si	Yes	Yes	ON[a]	45	4.5	340.8	N/A[b]

[a]The base temperature was 25 ˚C and 85 ˚C for the pinch-off and ON-state conditions, respectively.
[b]This case was not physically tested. This is a hypothetical situation considered for the purpose of comparison.

In Fig. 39, respective contributions to the total stress at the 'critical region' (shown in Fig. 33) of the GaN-on-SiC and GaN-on-Si devices are displayed for all cases listed in Table 6. For pinch-off state conditions (the first and third column of Fig. 39), self-heating is negligible thus the thermal stress portion is neglected. In these cases the total stress is the superposition of inverse piezoelectric stress and residual stress. Two bias conditions were compared; V_{gs}=-8 V, V_{ds}=45 V (critical voltage) for the GaN-on-Si device used in [125] (bias condition where the onset of inverse piezoelectric effect driven degradation took place) and V_{gs}=-8 V, V_{ds}=120 V for the GaN-on-SiC device having only a GFP. It is clearly seen that although the GaN-on-SiC device was biased under an extremely harsh condition, the magnitude of the total stress at the AlGaN 'critical region' was much lower than that for the GaN-on-Si device exposed to a relatively low voltage condition.

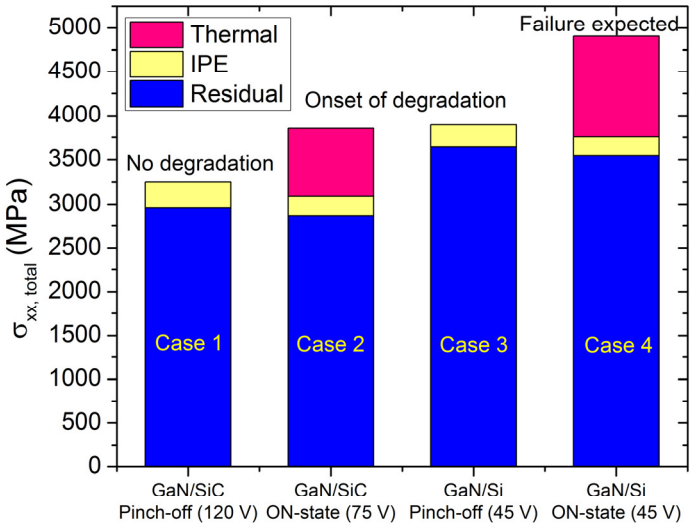

Fig. 39. Total stress induced in the critical region (displayed in Fig. 33) of the AlGaN barrier for different device structures under diverse test conditions. Effects of different baseplate temperatures for the pinch-off and ON-state tests were considered in the calculation of AlGaN residual stresses.

Interestingly, it is shown in Fig. 39 that the magnitude of total stresses in two different devices under different bias conditions where onset of degradation occurred (cases 2 and 3 in Table 6) are comparable. Therefore, in a mechanics point of view, the total stress at the critical region of AlGaN (Fig. 33) seems to be a decisive factor for the degradation mode introduced in [8] to take place. It was observed in a separate group of modified GaN-on-SiC test structures, for example, structures including SCFPs, that onset of degradation would occur at ON-state conditions where a similar value of total stress (~3.9 GPa) was induced.

For the case simulating the GaN-on-Si device under ON-state (V_{ds}=45 V, P=4.5 W/mm), since much higher peak temperature occurs (see Table 6) due to increased thermal resistance mainly originating from the less thermally conductive substrate

material, the magnitude of the thermo-elastic stress is much larger than that induced in the GaN-on-SiC device at this same power level. Therefore, this condition seems to be the most detrimental case where the device is prone to degrade or fail. The negative effect of elevated temperature on device degradation was previously reported in [119].

At ON-state conditions, it is expected that degradation mechanisms other than the inverse piezoelectric effect [8] including the hot electron induced degradation [7] would also play a role in causing reliability problems. Also high junction temperature may degrade the Schottky gate and ohmic contacts, drive thermal diffusion and intermixing processes, and form material defects. However, a similar argument relating ON-state conditions and the inverse piezoelectric effect [8] was made in several studies including [144]. For the devices tested in this work, instead of exhibiting gradual degradation along with increasing V_{ds} (at ON-state, P=4.5 W/mm), an abrupt change in performance indices including the gate leakage current was observed at a certain stress voltage (cirtical V_{ds}) as demonstrated in [8] and as shown in Fig. 35. The discussed results suggest that total stress can be a critical parameter related to the onset of the degradation mechanism formulated in [8] that accompanies defect formation or mechanical damage in the AlGaN barrier.

7.6 Conclusions

2-D electro-thermo-mechanical simulations were conducted to analyze the magnitude dependence of the maximum total stress in the AlGaN layer on operating conditions of

AlGaN/GaN HEMTs. Linear elastic deformation was assumed and wurtzite crystal elastic anisotropy was taken into account. For numerical calculations, continuum scale analysis was performed using credible values of elastic, thermal, and piezoelectric parameters reported in literature. Most AlGaN material properties were estimated using linear interpolation (Vegard's law). Credibility of modeling results were ensured by comparing the results with those obtained from Raman spectroscopy measurements and simplified 3-D modeling for simple bias test cases.

The physical mechanism that induces mechanical damage in the AlGaN layer of devices biased under high voltage conditions [8] is not believed to be a purely mechanical phenomenon [112]. Instead, it is believed that a combined effect of imperfect material growth, impurity diffusion processes (e.g., Ni and O [140]) promoted by tensile strain and/or temperature rise [145], and surface electrochemical reactions [146], [147] weakens the material, i.e., AlGaN, and then mechanical factors including the inverse piezoelectric effect trigger formation of defects/pits/cracks at the AlGaN surface, preferentially near the drain side corner of the gate where a peak electric field occurs [112]. Electrically this type of degradation is observed by an abrupt increase in OFF-state gate current at a certain V_{ds} which is often referred to as the 'critical voltage' in literature [8]. Structural damages in the AlGaN surface along the gate edge on its drain side were revealed by atomic force microscopy (AFM) and scanning probe electron microscopy (SEM) [116].

Modeling results show that by considering solely the electric field induced stress, it is difficult to elucidate the behavior of certain devices that withstand degradation during OFF-state Vds step stress tests conducted at extremely high voltages. In addition to the inverse piezoelectric stress, other stress contributions to the AlGaN total stress, namely,

the pre-existing residual stress in and operational thermo-elastic stress should not be overlooked.

It was seen within the examined device pool that devices were less prone to degrade at high voltage conditions if the GaN residual stress was more compressive or in other words, the AlGaN residual stress was less tensile. A more rigorous analysis would involve analysis of differences in the density or nature of intrinsic defects within the epitaxial layers used in individual devices. However, from the experimental results presented, the substrate (SiC, Si, etc.) induced residual stress in the GaN layer seems to be one of the decisive factors that impact the device reliability under high bias conditions. Caution should be taken because thermal stress obtained from sub-bandgap micro-Raman spectroscopy measurements probes the average value of stress through the thickness in the GaN layer, and may give a false sense that thermal strain reduces the overall elastic energy at the critical region of the AlGaN surface. To discuss the impact of mechanical stress on the defects (in some occasions, also pits and/or cracks) that form at high voltage bias conditions, the AlGaN surface (or Schottky/AlGaN interface) has to be taken into account, not the AlGaN/GaN interface or the GaN layer as considered in previous studies [148]. Under ON-state conditions, the thermal expansion coefficient mismatch between the gate material and AlGaN causes operational thermo-elastic stress to increase the overall tensile stress induced at this location.

CHAPTER 8

OPPORTUNITIES AND CONCLUSIONS

8.1 Summary

8.1.1 Development of Optical Stress Metrology for thin GaN epi-layers

Stress measurement techniques utilizing micro-Raman and micro-PL spectroscopy were developed that allow observation of the lateral as well as vertical (depth) variation of stress in the GaN layer of AlGaN/GaN HEMTs. Raman and PL biaxial stress conversion factors were derived to overcome the inconsistency in values reported in literature. Moreover, precise values for strain-free reference E_2(high) and A_1(LO) phonon frequencies as well as luminescent band gap energy (all at room temperature) were obtained under explicit initial spectrometer calibration conditions and appropriate GaN structural parameters. This work uniquely gives elaborate elucidation for experimental details and assumptions to represent a strain-free GaN crystal among similar studies reported in literature.

The residual stress in GaN wafers prepared for fabricating HEMT structures can be easily estimated using other conventional techniques such as wafer curvature measurement. However, different from those conventional methods, the developed

optical methods offer sufficient submicron spatial resolution that allow observation of the variation of mechanical stress over devices that have microscale characteristic lengths.

8.1.2 Analysis of the Residual Stress Distribution in AlGaN/GaN HEMTs

From the observation of the GaN residual stress distribution and depth variation in the AlGaN/GaN HEMTs examined, it is believed that a tensile strain is induced in the AlGaN layer near the edge of metallization structures. This effect is not unexpected, however, was experimentally confirmed in this work, for the first time in literature.

The tensile strain induced near the drain side corner of the gate adds up to tensile loads from different physical origins including the inverse piezoelectric stress under normal biased/operating conditions. Such increase in local tensile strain in the AlGaN barrier under the drain side corner of the gate may have an adverse effect on device reliability by promoting defect formation and/or crack initiation. Device designers should account for this surface pattern induced stress effect and optimize metallization and/or passivation overlayer deposition schemes to reduce the induced tensile strain in order to improve device reliability.

8.1.3 Thermometry of AlGaN/GaN HEMTs Using Multi-Spectral Raman Features

In this work, an accurate and time-efficient micro-Raman thermometry method was developed based on the work in [53] but using simplified linear equations. This method is

very useful in characterizing GaN based MEMS and microelectronic devices since a device temperature calibration is unnecessary unlike previously reported and widely used Raman thermometry techniques [52]. Elimination of calibration results in accurate temperature results, shorter experiment time, and relatively low uncertainty levels compared to results from different stress-independent Raman temperature measurement techniques utilizing the phonon linewidth or Stokes to anti-Stokes intensity ratio. The limitation of utilizing this linear 2-peak fit method is that the state of the evolved thermal stress in the GaN layer should be biaxial in the basal plane of GaN.

8.1.4 The Impact of Bias Conditions on Self-Heating in AlGaN/GaN HEMTs

Utilizing the developed 2-peak fit Raman thermometry method, the device channel temperature behavior versus drain and gate biases at the same power dissipation was examined. Under bias conditions where V_{ds} is higher and V_{gs} is more negative, the heat generation region becomes more concentrated at a nanoscale region under the drain end of the gate electrode. Consequently a higher channel peak temperature results compared to those for open channel conditions with lower V_{ds} even though the total power dissipation in the device is kept identical.

Even though this subject is not from an unexpected phenomenon, this study possesses usefulness and uniqueness since the bias dependence in high power GaN HEMTs was studied comparing temperatures at open channel conditions to those for practical operating conditions where V_{ds} is high (e.g., V_{ds}=28 V, 48 V). The observed results are

very important in terms of device lifetime or mean time to failure (MTTF) prediction from accelerated life time tests.

8.1.5 The Impact of Stress on the Degradation of AlGaN/GaN HEMTs

A combined analysis including extensive experiments and sumulation was performed to quantify the total stress occurring in the AlGaN layer under the drain side corner of the gate of AlGaN/GaN HEMTs subject to operating conditions where the onset of electrical performance degradation took place. These electrical conditions were found by conducting electrical step stress tests at both pinch-off and ON-state. The Residual stress in the AlGaN was estimated from Raman stress measurements. Inverse piezoelectric and thermo-elastic stresses were quantified via coupled electro-thermo-mechanical simulation. The overall total stress in the AlGaN was determined from the superposition of these three stress components assuming linear elastic deformation.

For the tested device pool, a consistent critical level of AlGaN total stress (~3.9 MPa) was found at operating conditions where device performance degradation started to occur even though the examined devices had different structures (substrate material, implementation of field plates). Although additional analysis involving for example, impurity diffusion and surface electrochemical reactions, is required to obtain a more complete picture of the high voltage induced degradation physics, such link between performance degradation and the evolution of total stress in devices was not reported in literature prior to this study.

8.2 Future Work

The work presented in this dissertation in Chapters 3 to 7 provide a comprehensive methodology to perform micro-Raman and PL to characterize stress and temperature in AlGaN/GaN HEMTs. With the exception of improvements to spatial resolution and temporal resolution, there does not seem to be a great need to further improve the stress and temperature measurement techniques under steady state conditions. However, there are still abundant opportunities to delve into the degradation physics of AlGaN/GaN HEMTs now that these tools are developed.

8.2.1 Extended Study of the Impact of Stress on the Degradation of AlGaN/GaN HEMTs

It was shown in Chapter 7 that the total stress in the AlGaN seems to play a major role in triggering mechanical damage at the AlGaN surface near the drain side corner of the gate having a critical level of ~3.9 GPa. Consistent results were seen in at least three type of devices; GaN-on-SiC devices with only gate field plate (GFP) structure implemented, similar GaN-on-SiC devices also having source connected field plates (SCFPs) (results not published), and GaN-on-Si devices with only GFPs. To gain confidence in the derived conclusions that relate the mechanical driver (total stress in the AlGaN) with the electric field induced degradation mode suggested in [8], we try to further limit the variable among different samples or device types to the pre-existing growth induced residual tensile strain in the AlGaN. For this purpose, AlGaN/GaN

HEMTs with identical structure except the AlGaN composition will be prepared. This method is advantageous over testing identical devices subject to 4-point bending in a number of aspects. First, a relatively large sample die (the longest length of the wafer piece will have to be ~1 inch) needs to be prepared for 4-point bending tests. Even though this condition is met, the samples can easily break since brittle materials compose the device die. Variation of Al% alters the 'effective' AlGaN lattice constants and leads to different levels of tensile strain induced in the AlGaN layer of the devices. Accordingly, the strain variation in AlGaN results in change in electrical characteristics of the device mainly due to the variation in the piezoelectric polarization induced in the AlGaN. Electrical step stress tests will be conducted on these devices but with smaller V_{ds} step sizes (1 V) compared to the investigation described in Chapter 7. Efforts will be made to find a correlation between the Al% (or total stress in the AlGaN near the drain end of the gate) and the critical V_{ds} where onset of electrical performance degradation takes place. Mechanical stresses originating from different origins will be again considered for different voltage bias conditions. One drawback of this experimental scheme is that we are performing comparative analysis not on an identical AlGaN material. As the AlGaN composition varies, the mechanical properties as well as electrical properties such as elastic stiffness matrix and piezoelectric coefficients also changes and will have to be fully accounted for in the stress analysis. Albeit of these demerits, the study will provide insight for AlGaN/GaN HEMT design optimization regarding the trade-off or balance among growth capabilities, device performance, and reliability to GaN HEMT manufacturers.

8.2.2 Required Workload and Expected Outcome

For this extended study, an automated device testing software needs to be developed. Several automated test functions must be developed to perform step stress tests at gradually increased electrical stress conditions (V_{ds}) while benign device electrical characterization should be performed in the middle of different electrical stress conditions to detect post-stress device degradation. Time dependence of the HEMT degradation under high voltage conditions will also be examined thus these automated tests should be conducted at various stress-time durations ranging from several minutes to hundreds of hours. Raman residual stress measurements will be performed to ensure similar levels of residual stress residing in the GaN layer of all samples. The geometry used in the coupled electro-thermo-mechanical model requires modification and especially, for electrical simulation, the data regarding I-V characteristics of real devices need to be collected. At this point, it is expected that higher Al content will lead to lower critical V_{ds} due to higher level of tensile stress resulting from smaller strain-free effective lattice constants of the corresponding AlGaN layers.

8.3 Conclusions

Conventional semiconductor device technologies are hitting their limits in a myriad of applications. Customers push developers to the performance limits given by the intrinsic properties of the materials system employed. For instance, regarding telecommunication systems that are relevant to the devices studied in this work, new

commercial devices such as smart-phones immerge from brilliant ideas and accordingly there occurs a need or push for more powerful and high quality signals so that customers can communicate even at extremely distant or isolated regions. Who would have imagined we would be able to receive calls in the third basement or call 911 on mountains in Colorado? Major phone carriers are under a push to provide customers with high speed internet access with a speed comparable to Gigabit Ethernet meaning higher data transmission rate. Even having these intense technological pushes in the commercial market, it is not surprising that indeed extreme needs will exist for military applications where performance is of upmost importance rather than cost. Therefore, it seems natural that, if conventional materials systems cannot afford the requirements from the customers, a paradigm shift is essential and developers must jump into a totally new technology.

However, as the performance goes up and a new technology is employed, more complicated reliability issues arise. And it becomes more and more difficult to develop commercial level products or obtain optimized design by trial-and-error or reverse engineering without rigorous analysis. Dealing with these reliability problems, an approach based on a single physical domain is not enough and the problems become highly interdisciplinary, i.e., various physics are coupled. Also as the time and length scales of the technology reduces, under the continuum limit, things become even more complicated. Therefore, not only fundamental research in each physical or engineering discipline at small scales has to be conducted but also efforts to see the outcome of fully coupled physical phenomena for an integrated system has to be done. It has become even more important for product developers to keep pace with researchers conducting these fundamental research activities.

In the author's opinion, the work done here may serve as a good example of the previously mentioned statements. The project was conducted through the collaboration of a defense corporation, military research lab, and a university lab. Practical needs or problem statements were made from RFMD and we have collaborated with AFRL to solve those multi-disciplinary problems. Collaborative research was done via engineers and scientists from different fields; materials science, applied physics, physics, and us mechanical engineers. Core ideas did originate from the most well-experienced scientists at AFRL and we served to assist them with our capabilities and for some occasions would address reliability problems in a different perspective. Continuous collaboration was successfully done without time to lie back via the telecon meetings held bi-weekly.

We have developed new and most accurate (to date) stress and temperature measurement techniques that can be applied to GaN based micro electronics or microelectromechancial systems (MEMS). For this work intense efforts were made to find best test samples which finally came from different origins such as Kyma Technologies and AFRL. Rigorous analysis and discussions were made regarding the experimental instruments (spectrometers) with field engineers from Renishaw and Horiba Jovin Yvon to get most precise results. Of course in-depth understanding of the physical origins of the optical responses we utilized to indirectly measure the mechanical quantities was required. Eventually, the developed techniques were applied to find out critical aspects regarding device fabrication and life time prediction that are of primary importance for device manufacturers. In the end, to delve into degradation physics of AlGaN/GaN HEMTs, all of the developed experimental methods were utilized together with coupled electro-thermo-mechancial simulation to quantify or extrapolate important

physical quantities that were not observable through the experimental methods but having paramount importance regarding device reliability. In the beginning different physical effects were investigated separately by AFRL and us and finally the reliable models were unified to quantify mechanical stresses induced from different physical origins involving electro-mechanical coupling, thermo-mechanical coupling, and hetero-epitaxial growth or processing. Derived results were meaningful in both an academic and practical point of view. I do believe this work contributed at least in more one step to move forward the GaN electronics technology closer to its full commercialization.

REFERENCES

[1] O. Ambacher, J. Smart, J. R. Shealy, N. G. Weimann, K. Chu, M. Murphy, W. J. Schaff, L. F. Eastman, R. Dimitrov, L. Wittmer, M. Stutzmann, W. Rieger, and J. Hilsenbeck, "Two-dimensional electron gases induced by spontaneous and piezoelectric polarization charges in N- and Ga-face AlGaN/GaN heterostructures," *Journal of Applied Physics,* vol. 85, pp. 3222-3233, Mar 15 1999.

[2] H. Angerer, D. Brunner, F. Freudenberg, O. Ambacher, M. Stutzmann, R. Hopler, T. Metzger, E. Born, G. Dollinger, A. Bergmaier, S. Karsch, and H. J. Korner, "Determination of the Al mole fraction and the band gap bowing of epitaxial AlxGa1-xN films," *Applied Physics Letters,* vol. 71, pp. 1504-1506, Sep 15 1997.

[3] Aethercomm, "Gallium nitride microwave transistor technology for radar applications," *Microwave Journal,* vol. 51, pp. 106-+, Jan 2008.

[4] T. Kikkawa, K. Joshin, and M. Kanamura, "GaN Device for Highly Efficient Power Amplifiers," *Fujitsu Scientific & Technical Journal,* vol. 48, pp. 40-46, Jan 2012.

[5] M. Kanechika, T. Uesugi, and T. Kachi, "Advanced SiC and GaN Power Electronics for Automotive Systems," *2010 International Electron Devices Meeting - Technical Digest,* 2010.

[6] T. Palacios, J. W. Chung, O. Saadat, and F. Mieville, "GaN and digital electronics: A way out of Moore's law?," *Physica Status Solidi C: Current Topics in Solid State Physics, Vol 6, No 6,* vol. 6, pp. 1361-1364, 2009.

[7] G. Meneghesso, G. Verzellesi, F. Danesin, F. Rampazzo, F. Zanon, A. Tazzoli, M. Meneghini, and E. Zanoni, "Reliability of GaN high-electron-mobility transistors: State of the art and perspectives," *Ieee Transactions on Device and Materials Reliability,* vol. 8, pp. 332-343, Jun 2008.

[8] J. A. del Alamo and J. Joh, "GaN HEMT reliability," *Microelectronics Reliability,* vol. 49, pp. 1200-1206, Sep-Nov 2009.

[9] A. Hushur, M. H. Manghnani, and J. Narayan, "Raman studies of GaN/sapphire thin film heterostructures," *Journal of Applied Physics,* vol. 106, pp. -, Sep 1 2009.

[10] W. Rieger, T. Metzger, H. Angerer, R. Dimitrov, O. Ambacher, and M. Stutzmann, "Influence of substrate-induced biaxial compressive stress on the

optical properties of thin GaN films," *Applied Physics Letters,* vol. 68, pp. 970-972, Feb 12 1996.

[11] V. Y. Davydov, N. S. Averkiev, I. N. Goncharuk, D. K. Nelson, I. P. Nikitina, A. S. Polkovnikov, A. N. Smirnov, M. A. Jacobsen, and O. K. Semchinova, "Raman and photoluminescence studies of biaxial strain in GaN epitaxial layers grown on 6H-SiC," *Journal of Applied Physics,* vol. 82, pp. 5097-5102, Nov 15 1997.

[12] K. Funato, S. Hashimoto, K. Yanashima, F. Nakamura, and M. Ikeda, "Residual strain dependence of optical characteristics in GaN layers grown on (0001) sapphire substrates," *Applied Physics Letters,* vol. 75, pp. 1137-1139, Aug 23 1999.

[13] I. H. Lee, I. H. Choi, C. R. Lee, and S. K. Noh, "Evolution of stress relaxation and yellow luminescence in GaN/sapphire by Si incorporation," *Applied Physics Letters,* vol. 71, pp. 1359-1361, Sep 8 1997.

[14] H. Park, C. Park, S. Yeo, S. Kang, M. Mastro, O. Kryliouk, and T. Anderson, "Epitaxial strain energy measurements of GaN on sapphire by Raman spectroscopy," *physica status solidi (c),* vol. 2, pp. 2446-2449, 2005.

[15] R. Trew, G. Bilbro, W. Kuang, Y. Liu, and H. Yin, "Microwave AlGaN/GaN HFETs," *IEEE Microwave Magazine,* vol. 6, pp. 56-66, 2005.

[16] Y. F. Zhang, I. P. Smorchkova, C. R. Elsass, S. Keller, J. P. Ibbetson, S. Denbaars, U. K. Mishra, and J. Singh, "Charge control and mobility in AlGaN/GaN transistors: Experimental and theoretical studies," *Journal of Applied Physics,* vol. 87, pp. 7981-7987, Jun 1 2000.

[17] J. Bernat, P. Javorka, M. Marso, and P. Kordos, "Conductivity and Hall effect measurements on intentionally undoped and doped AlGaN/GaN heterostructures before and after passivation," *Applied Physics Letters,* vol. 83, pp. 5455-5457, Dec 29 2003.

[18] M. Azize and T. Palacios, "Effect of substrate-induced strain in the transport properties of AlGaN/GaN heterostructures," *Journal of Applied Physics,* vol. 108, pp. -, Jul 15 2010.

[19] B. Benbakhti, A. Soltani, K. Kalna, M. Rousseau, and J. C. De Jaeger, "Effects of Self-Heating on Performance Degradation in AlGaN/GaN-Based Devices," *Ieee Transactions on Electron Devices,* vol. 56, pp. 2178-2185, Oct 2009.

[20] S. Karmalkar and U. K. Mishra, "Enhancement of breakdown voltage in AlGaN/GaN high electron mobility transistors using a field plate," *Ieee Transactions on Electron Devices,* vol. 48, pp. 1515-1521, Aug 2001.

[21] X. B. Zhang, T. Taliercio, S. Kolliakos, and P. Lefebvre, "Influence of electron-phonon interaction on the optical properties of III nitride semiconductors," *Journal of Physics-Condensed Matter,* vol. 13, pp. 7053-7074, Aug 13 2001.

[22] J. M. Hayes, "Raman scattering in GaN, AlN and AlGaN: Basic Material Properties, Processing and Devices," Doctor of Philosophy, Department of Physics, University of Bristol, 2002.

[23] C. Bungaro, K. Rapcewicz, and J. Bernholc, "Ab initio phonon dispersions of wurtzite AlN, GaN, and InN," *Physical Review B,* vol. 61, pp. 6720-6725, Mar 1 2000.

[24] A. Matulionis, "Hot phonons in GaN channels for HEMTs," *Physica Status Solidi a-Applications and Materials Science,* vol. 203, pp. 2313-2325, Aug 2006.

[25] S. Sridharan, A. Venkatachalam, and P. Yoder, "Electrothermal analysis of AlGaN/GaN high electron mobility transistors," *Journal of Computational Electronics,* vol. 7, pp. 236-239, 2008.

[26] A. Christensen and S. Graham, "Multiscale Modeling of Hot Spots in Gan High Electron Mobility Transistors," *Ipack 2009: Proceedings of the Asme Inter Pack Conference 2009, Vol 1,* pp. 535-541, 2010.

[27] I. Ahmad, M. Holtz, N. N. Faleev, and H. Temkin, "Dependence of the stress-temperature coefficient on dislocation density in epitaxial GaN grown on alpha-Al2O3 and 6H-SiC substrates," *Journal of Applied Physics,* vol. 95, pp. 1692-1697, Feb 15 2004.

[28] A. Sarua, H. F. Ji, M. Kuball, M. J. Uren, T. Martin, K. P. Hilton, and R. S. Balmer, "Integrated micro-Raman/Infrared thermography probe for monitoring of self-heating in AlGaN/GaN transistor structures," *Ieee Transactions on Electron Devices,* vol. 53, pp. 2438-2447, Oct 2006.

[29] J. Kuzmik, P. Javorka, A. Alam, M. Marso, M. Heuken, and P. Kordos, "Determination of channel temperature in AlGaN/GaN HEMTs grown on sapphire and silicon substrates using DC characterization method," *Ieee Transactions on Electron Devices,* vol. 49, pp. 1496-1498, Aug 2002.

[30] N. Killat, M. Kuball, T. M. Chou, U. Chowdhury, and J. Jimenez, "Temperature Assessment of AlGaN/GaN HEMTs: A Comparative study by Raman, Electrical and IR Thermography," *2010 International Reliability Physics Symposium,* pp. 528-531, 2010.

[31] J. Park, M. W. Shin, and C. C. Lee, "Thermal modeling and measurement of GaN-based HFET devices," *Ieee Electron Device Letters,* vol. 24, pp. 424-426, Jul 2003.

[32] J. Park, D. Kakovitch, M. W. Shin, and C. C. Lee, "Thermal modeling and measurement of AlGaN/GaN HFETs built on sapphire and SiC substrates," *53rd Electronic Components & Technology Conference, 2003 Proceedings,* pp. 438-442, 2003.

[33] K. Maize, E. Heller, D. Dorsey, and A. Shakouri, "Thermoreflectance CCD imaging of self heating in AlGaN/GaN high electron mobility power transistors at high drain voltage," in *Semiconductor Thermal Measurement and Management Symposium (SEMI-THERM), 2012 28th Annual IEEE*, 2012, pp. 173-181.

[34] A. Majumdar, J. Lai, M. Chandrachood, O. Nakabeppu, Y. Wu, and Z. Shi, "Thermal Imaging by Atomic-Force Microscopy Using Thermocouple Cantilever Probes," *Review of Scientific Instruments,* vol. 66, pp. 3584-3592, Jun 1995.

[35] R. Aubry, J. C. Jacquet, J. Weaver, O. Durand, P. Dobson, G. Mills, M. A. di Forte-Poisson, S. Cassette, and S. L. Delage, "SThM temperature mapping and nonlinear thermal resistance evolution with bias on AlGaN/GaN HEMT devices," *Ieee Transactions on Electron Devices,* vol. 54, pp. 385-390, Mar 2007.

[36] T. Batten, A. Manoi, M. J. Uren, T. Martin, and M. Kuball, "Temperature analysis of AlGaN/GaN based devices using photoluminescence spectroscopy: Challenges and comparison to Raman thermography," *Journal of Applied Physics,* vol. 107, Apr 1 2010.

[37] T. Beechem III, "Metrology of gan electronics using micro-raman spectroscopy," Ph.D. Ph.D. thesis, Georgia Institute of Technology, 2008.

[38] M. Kuball, G. J. Riedel, J. W. Pomeroy, A. Sarua, M. J. Uren, T. Martin, K. P. Hilton, J. O. Maclean, and D. J. Wallis, "Time-resolved temperature measurement of AlGaN/GaN electronic devices using micro-Raman spectroscopy," *Ieee Electron Device Letters,* vol. 28, pp. 86-89, Feb 2007.

[39] J. R. Ferraro and K. Nakamoto, *Introductory Raman Spectroscopy*, 2 ed.: Academic Press, 2003.

[40] I. DeWolf, "Micro-Raman spectroscopy to study local mechanical stress in silicon integrated circuits," *Semiconductor Science and Technology,* vol. 11, pp. 139-154, Feb 1996.

[41] Z. Feng, "Micro-Raman scattering and microphotoluminescence of GaN thin films grown on sapphire by metal-organic chemical vapor deposition," *Optical engineering,* vol. 41, p. 2022, 2002.

[42] F. C. Wang, C. L. Cheng, Y. F. Chen, C. F. Huang, and C. C. Yang, "Residual thermal strain in thick GaN epifilms revealed by cross-sectional Raman scattering and cathodoluminescence spectra," *Semiconductor Science and Technology,* vol. 22, pp. 896-899, Aug 2007.

[43] C. Kisielowski, J. Kruger, S. Ruvimov, T. Suski, J. W. Ager, 3rd, E. Jones, Z. Liliental-Weber, M. Rubin, E. R. Weber, M. D. Bremser, and R. F. Davis, "Strain-related phenomena in GaN thin films," *Phys Rev B Condens Matter,* vol. 54, pp. 17745-17753, Dec 15 1996.

[44] D. G. Zhao, S. J. Xu, M. H. Xie, S. Y. Tong, and H. Yang, "Stress and its effect on optical properties of GaN epilayers grown on Si(111), 6H-SiC(0001), and c-plane sapphire," *Applied Physics Letters,* vol. 83, pp. 677-679, Jul 28 2003.

[45] J. M. Wagner and F. Bechstedt, "Properties of strained wurtzite GaN and AlN: Ab initio studies," *Physical Review B,* vol. 66, pp. -, Sep 15 2002.

[46] Y. F. Li, B. Yao, Y. M. Lu, Y. Q. Gai, C. X. Cong, Z. Z. Zhang, D. X. Zhao, J. Y. Zhang, B. H. Li, D. Z. Shen, X. W. Fan, and Z. K. Tang, "Biaxial stress-dependent optical band gap, crystalline, and electronic structure in wurtzite ZnO: Experimental and ab initio study," *Journal of Applied Physics,* vol. 104, pp. -, Oct 15 2008.

[47] A. Sarua, H. F. Ji, M. Kuball, M. J. Uren, T. Martin, K. J. Nash, K. P. Hilton, and R. S. Balmer, "Piezoelectric strain in AlGaN/GaN heterostructure field-effect transistors under bias," *Applied Physics Letters,* vol. 88, Mar 6 2006.

[48] T. Beechem, A. Christensen, D. S. Green, and S. Graham, "Assessment of stress contributions in GaN high electron mobility transistors of differing substrates using Raman spectroscopy," *Journal of Applied Physics,* vol. 106, Dec 1 2009.

[49] W. S. Li, Z. X. Shen, Z. C. Feng, and S. J. Chua, "Temperature dependence of Raman scattering in hexagonal gallium nitride films," *Journal of Applied Physics,* vol. 87, pp. 3332-3337, Apr 1 2000.

[50] M. Kuball, J. M. Hayes, Y. Shi, and J. H. Edgar, "Phonon lifetimes in bulk AlN and their temperature dependence," *Applied Physics Letters,* vol. 77, pp. 1958-1960, Sep 25 2000.

[51] M. Kuball, J. M. Hayes, M. J. Uren, T. Martin, J. C. H. Birbeck, R. S. Balmer, and B. T. Hughes, "Measurement of temperature in active high-power AlGaN/GaN HFETs using Raman spectroscopy," *Ieee Electron Device Letters,* vol. 23, pp. 7-9, Jan 2002.

[52] T. Beechem, A. Christensen, S. Graham, and D. Green, "Micro-Raman thermometry in the presence of complex stresses in GaN devices," *Journal of Applied Physics,* vol. 103, Jun 15 2008.

[53] T. Batten, J. W. Pomeroy, M. J. Uren, T. Martin, and M. Kuball, "Simultaneous measurement of temperature and thermal stress in AlGaN/GaN high electron mobility transistors using Raman scattering spectroscopy," *Journal of Applied Physics,* vol. 106, Nov 1 2009.

[54] M. Kuball, J. M. Hayes, Y. Shi, J. H. Edgar, A. D. Prins, N. W. A. van Uden, and D. J. Dunstan, "Raman scattering studies on single-crystalline bulk AlN: temperature and pressure dependence of the AlN phonon modes," *Journal of Crystal Growth,* vol. 231, pp. 391-396, Oct 2001.

[55] I. Ahmad, V. Kasisomayajula, D. Y. Song, L. Tian, J. M. Berg, and M. Holtz, "Self-heating in a GaN based heterostructure field effect transistor: Ultraviolet and visible Raman measurements and simulations," *Journal of Applied Physics,* vol. 100, Dec 1 2006.

[56] K. Barghout and J. Chaudhuri, "Calculation of residual thermal stress in GaN epitaxial layers grown on technologically important substrates," *Journal of Materials Science,* vol. 39, pp. 5817-5823, Sep 15 2004.

[57] M. Leszczynski, H. Teisseyre, T. Suski, I. Grzegory, M. Bockowski, J. Jun, S. Porowski, K. Pakula, J. M. Baranowski, C. T. Foxon, and T. S. Cheng, "Lattice parameters of gallium nitride," *Applied Physics Letters,* vol. 69, pp. 73-75, Jul 1 1996.

[58] C. Roder, S. Einfeldt, S. Figge, and D. Hommel, "Temperature dependence of the thermal expansion of GaN," *Physical Review B,* vol. 72, Aug 2005.

[59] S. A. Kukushkin, A. V. Osipov, V. N. Bessolov, B. K. Medvedev, V. K. Nevolin, and K. A. Tcarik, "Substrates for epitaxy of gallium nitride: New materials and techniques," *Reviews on Advanced Materials Science,* vol. 17, pp. 1-32, Mar 2008.

[60] H. Iwanaga, A. Kunishige, and S. Takeuchi, "Anisotropic thermal expansion in wurtzite-type crystals," *Journal of Materials Science,* vol. 35, pp. 2451-2454, May 2000.

[61] J. B. Wachtman, T. G. Scuderi, and G. W. Cleek, "Linear Thermal Expansion of Aluminum Oxide and Thorium Oxide from 100-Degrees-K to 1100-Degrees-K," *Journal of the American Ceramic Society,* vol. 45, pp. 319-323, 1962.

[62] Z. Li and R. C. Bradt, "Thermal-Expansion and Thermal-Expansion Anisotropy of Sic Polytypes," *Journal of the American Ceramic Society,* vol. 70, pp. 445-448, Jul 1987.

[63] J. Pernot, E. Bustarret, M. Rudzinski, P. R. Hageman, and P. K. Larsen, "Strain relaxation in GaN grown on vicinal 4H-SiC(0001) substrates," *Journal of Applied Physics,* vol. 101, pp. -, Feb 1 2007.

[64] S. Tripathy, S. J. Chua, P. Chen, and Z. L. Miao, "Micro-Raman investigation of strain in GaN and AlxGa1-xN/GaN heterostructures grown on Si(111)," *Journal of Applied Physics,* vol. 92, pp. 3503-3510, Oct 1 2002.

[65] C. G. Van de Walle, "Effects of impurities on the lattice parameters of GaN," *Physical Review B,* vol. 68, pp. -, Oct 15 2003.

[66] M. A. Moram and M. E. Vickers, "X-ray diffraction of III-nitrides," *Reports on Progress in Physics,* vol. 72, pp. -, Mar 2009.

[67] A. Polian, M. Grimsditch, and I. Grzegory, "Elastic constants of gallium nitride," *Journal of Applied Physics,* vol. 79, pp. 3343-3344, Mar 15 1996.

[68] A. F. Wright, "Elastic properties of zinc-blende and wurtzite AlN, GaN, and InN," *Journal of Applied Physics,* vol. 82, pp. 2833-2839, Sep 15 1997.

[69] M. A. Moram, Z. H. Barber, and C. J. Humphreys, "Accurate experimental determination of the Poisson's ratio of GaN using high-resolution x-ray diffraction," *Journal of Applied Physics,* vol. 102, pp. -, Jul 15 2007.

[70] S. J. Xu, W. Liu, and M. F. Li, "Effect of temperature on longitudinal optical phonon-assisted exciton luminescence in heteroepitaxial GaN layer," *Applied Physics Letters,* vol. 77, pp. 3376-3378, Nov 20 2000.

[71] H. Seo, Q. Chen, M. Iliev, L. Tu, C. Hsiao, J. Mean, and W. Chu, "Epitaxial GaN nanorods free from strain and luminescent defects," *Applied Physics Letters,* vol. 88, p. 153124, 2006.

[72] N. Thillosen, K. Sebald, H. Hardtdegen, R. Meijers, R. Calarco, S. Montanari, N. Kaluza, J. Gutowski, and H. Luth, "The state of strain in single GaN nanocolumns as derived from micro-photoluminescence measurements," *Nano Lett,* vol. 6, pp. 704-8, Apr 2006.

[73] M. Jamil, J. Grandusky, V. Jindal, F. Shahedipour-Sandvik, S. Guha, and M. Arif, "Development of strain reduced GaN on Si (111) by substrate engineering," *Applied Physics Letters,* vol. 87, p. 082103, 2005.

[74] F. Demangeot, J. Frandon, M. A. Renucci, O. Briot, B. Gil, and R. L. Aulombard, "Raman determination of phonon deformation potentials in alpha-GaN," *Solid State Communications,* vol. 100, pp. 207-210, Oct 1996.

[75] F. Demangeot, J. Frandon, P. Baules, F. Natali, F. Semond, and J. Massies, "Phonon deformation potentials in hexagonal GaN," *Physical Review B,* vol. 69, pp. -, Apr 2004.

[76] M. Klose, N. Wieser, G. C. Rohr, R. Dassow, F. Scholz, and J. Off, "Strain investigations of wurtzite GaN by Raman phonon diagnostics with photoluminescence supplement," *Journal of Crystal Growth,* vol. 190, pp. 634-638, Jun 1998.

[77] J. Kim, K. Baik, C. Park, S. Cho, S. J. Pearton, and F. Ren, "Measurement of external stress on bulk GaN," *Physica Status Solidi a-Applications and Materials Science,* vol. 203, pp. 2393-2396, Aug 2006.

[78] W. G. Perry, T. Zheleva, M. D. Bremser, R. F. Davis, W. Shan, and J. J. Song, "Correlation of biaxial strains, bound exciton energies, and defect microstructures in GaN films grown on AlN/6H-SiC(0001) substrates," *Journal of Electronic Materials,* vol. 26, pp. 224-231, Mar 1997.

[79] X. X. Han, J. J. Wu, J. M. Li, G. W. Cong, X. L. Liu, Q. S. Zhu, and Z. G. Wang, "Photoluminescence investigation of two-dimensional electron gas in an undoped AlxGa1-xN/GaN heterostructure," *Chinese Physics Letters,* vol. 22, pp. 2096-2099, Aug 2005.

[80] L. Dong, S. K. Yadav, R. Ramprasad, and S. P. Alpay, "Band gap tuning in GaN through equibiaxial in-plane strains," *Applied Physics Letters,* vol. 96, May 17 2010.

[81] A. Soltani, A. BenMoussa, S. Touati, V. Hoel, J. C. De Jaeger, J. Laureyns, Y. Cordier, C. Marhic, M. A. Djouadi, and C. Dua, "Development and analysis of low resistance ohmic contact to n-AlGaN/GaN HEMT," *Diamond and Related Materials,* vol. 16, pp. 262-266, Feb 2007.

[82] T. Matsuki, N. Mise, S. Inumiya, T. Eimori, and Y. Nara, "Impact of gate metal-induced stress on performance modulation in gate-last metal-oxide-semiconductor field-effect transistors," *Japanese Journal of Applied Physics Part 1-Regular Papers Brief Communications & Review Papers,* vol. 46, pp. 3181-3184, May 2007.

[83] T. Onodera and H. Nishi, "Theoretical-Study of the Piezoelectric Effect on Gaas-Mesfets on (100), (011), and (111bar) Ga, and (111) as Substrates," *Ieee Transactions on Electron Devices,* vol. 36, pp. 1580-1585, Sep 1989.

[84] E. D. Haberer, C. H. Chen, M. Hansen, S. Keller, S. P. DenBaars, U. K. Mishra, and E. L. Hu, "Enhanced diffusion as a mechanism for ion-induced damage propagation in GaN," *Journal of Vacuum Science & Technology B,* vol. 19, pp. 603-608, May-Jun 2001.

[85] J. M. Hwang, J. T. Hsieh, H. L. Hwang, O. Breitschadel, and H. Schweizer, "Defect depth profiling using photoluminescence and cathodoluminescence spectroscopy: the role of oxygen on reactive ion beam etching of GaN in O-2/Ar plasmas," *Applied Surface Science,* vol. 175, pp. 450-455, May 15 2001.

[86] D. G. Zhao, D. S. Jiang, J. J. Zhu, Z. S. Liu, S. M. Zhang, H. Yang, and J. W. Liang, "The influence of V/III ratio in the initial growth stage on the properties of GaN epilayer deposited on low temperature AlN buffer layer," *Journal of Crystal Growth,* vol. 303, pp. 414-418, May 15 2007.

[87] A. Sarua, H. Ji, J. W. Pomeroy, M. J. Uren, T. Martin, and M. Kuball, "Converse piezoelectric strain in undoped and Fe-doped AlGaN/GaN heterostructure field effect transistors studied by Raman scattering," *Semiconductor Science and Technology,* vol. 25, Aug 2 2010.

[88] B. T. Berntein, "Elastic Constants of Synthetic Sapphire at 27degrees C," *Journal of Applied Physics,* vol. 34, pp. 169-&, 1963.

[89] K. Kamitani, M. Grimsditch, J. C. Nipko, C. K. Loong, M. Okada, and I. Kimura, "The elastic constants of silicon carbide: A Brillouin-scattering study of 4H and 6H SiC single crystals," *Journal of Applied Physics,* vol. 82, pp. 3152-3154, Sep 15 1997.

[90] B. A. Walmsley, Y. Liu, X. Z. Hu, M. B. Bush, K. J. Winchester, M. Martyniuk, J. M. Dell, and L. Faraone, "Effects of deposition temperature on the mechanical and physical properties of silicon nitride thin films," *Journal of Applied Physics,* vol. 98, Aug 15 2005.

[91] D. Faurie, P. O. Renault, E. Le Bourhis, P. Villain, P. Goudeau, and F. Badawi, "Measurement of thin film elastic constants by X-ray diffraction," *Thin Solid Films,* vol. 469, pp. 201-205, Dec 22 2004.

[92] P. M. Fabis, "Reliability of radio frequency/microwave power packages: the effects of component materials and assembly processes," *Microelectronics Reliability,* vol. 39, pp. 1265-1274, Aug 1999.

[93] N. Killat, M. Montes, J. W. Pomeroy, T. Paskova, K. R. Evans, J. Leach, X. Li, U. Ozgur, H. Morkoc, K. D. Chabak, A. Crespo, J. K. Gillespie, R. Fitch, M. Kossler, D. E. Walker, M. Trejo, G. D. Via, J. D. Blevins, and M. Kuball, "Thermal Properties of AlGaN/GaN HFETs on Bulk GaN Substrates," *Ieee Electron Device Letters,* vol. 33, pp. 366-368, Mar 2012.

[94] Z. Li and R. C. Bradt, "Thermal-Expansion of the Hexagonal (6h) Polytype of Silicon-Carbide," *Journal of the American Ceramic Society,* vol. 69, pp. 863-866, Dec 1986.

[95] E. A. Burgemeister, W. Vonmuench, and E. Pettenpaul, "Thermal-Conductivity and Electrical-Properties of 6h Silicon-Carbide," *Journal of Applied Physics,* vol. 50, pp. 5790-5794, 1979.

[96] T. F. Retajczyk and A. K. Sinha, "Elastic Stiffness and Thermal-Expansion Coefficients of Various Refractory Silicides and Silicon-Nitride Films," *Thin Solid Films,* vol. 70, pp. 241-247, 1980.

[97] P. Eriksson, J. Y. Andersson, and G. Stemme, "Thermal characterization of surface-micromachined silicon nitride membranes for thermal infrared detectors," *Journal of Microelectromechanical Systems,* vol. 6, pp. 55-61, Mar 1997.

[98] D. S. Green, J. D. Brown, R. Vetury, S. Lee, S. R. Gibb, K. Krishnamurthy, M. J. Poulton, J. Martin, and J. B. Shealy, "Status of GaN HEMT performance and reliability," *Gallium Nitride Materials and Devices III, Proc. of SPIE,* vol. 6894, 2008.

[99] E. R. Heller, R. Vetury, and D. S. Green, "Development of a Versatile Physics-Based Finite-Element Model of an AlGaN/GaN HEMT Capable of Accommodating Process and Epitaxy Variations and Calibrated Using Multiple DC Parameters," *Ieee Transactions on Electron Devices,* vol. 58, pp. 1091-1095, Apr 2011.

[100] W. L. Liu and A. A. Balandin, "Temperature dependence of thermal conductivity of AlxGa1-xN thin films measured by the differential 3 omega technique," *Applied Physics Letters,* vol. 85, pp. 5230-5232, Nov 29 2004.

[101] F. Bertoluzza, N. Delmonte, and R. Menozzi, "Three-dimensional finite-element thermal simulation of GaN-based HEMTs," *Microelectronics Reliability,* vol. 49, pp. 468-473, May 2009.

[102] A. Manoi, J. W. Pomeroy, N. Killat, and M. Kuball, "Benchmarking of Thermal Boundary Resistance in AlGaN/GaN HEMTs on SiC Substrates: Implications of the Nucleation Layer Microstructure," *Ieee Electron Device Letters,* vol. 31, pp. 1395-1397, Dec 2010.

[103] E. Gmelin, M. Asen-Palmer, M. Reuther, and R. Villar, "Thermal boundary resistance of mechanical contacts between solids at sub-ambient temperatures," *Journal of Physics D-Applied Physics,* vol. 32, pp. R19-R43, Mar 21 1999.

[104] J. Gleize, M. A. Renucci, J. Frandon, E. Bellet-Amalric, and B. Daudin, "Phonon deformation potentials of wurtzite AlN," *Journal of Applied Physics,* vol. 93, pp. 2065-2068, Feb 15 2003.

[105] E. R. Heller and A. Crespo, "Electro-thermal modeling of multifinger AlGaN/GaN HEMT device operation including thermal substrate effects," *Microelectronics Reliability,* vol. 48, pp. 45-50, Jan 2008.

[106] M. Hosch, J. W. Pomeroy, A. Sarua, M. Kuball, H. Jung, and H. Schumacher, "Field Dependent Self-Heating Effects in High-Power AlGaN/GaN HEMTs," *CS MANTECH Conference,* pp. 32-55, 2009.

[107] M. Bauer, A. M. Gigler, A. J. Huber, R. Hillenbrand, and R. W. Stark, "Temperature-depending Raman line-shift of silicon carbide," *Journal of Raman Spectroscopy,* vol. 40, pp. 1867-1874, Dec 2009.

[108] J. D. Brown, S. Gibb, J. McKenna, M. Poulton, S. Lee, K. Gratzer, B. Hosse, T. Mercier, Y. Yang, M. Young, D. Green, R. Vetury, and J. Shealy, "Performance, Reliability, and Manufacturability of AlGaN/GaN High Electron Mobility Transistors on Silicon Carbide Substrates," *ECS Transactions,* vol. 3, pp. 161-179, 2006.

[109] H. Kim, A. Vertiatchikh, R. M. Thompson, V. Tilak, T. R. Prunty, J. R. Shealy, and L. F. Eastman, "Hot electron induced degradation of undoped AlGaN/GaN HFETs," *Microelectronics Reliability,* vol. 43, pp. 823-827, Jun 2003.

[110] E. R. Heller, S. Choi, D. Dorsey, R. Vetury, and S. Graham, "Electrical and structural dependence of operating temperature of AlGaN/GaN HEMTs," *Microelectronics Reliability,* vol. 53, pp. 872-877, 2013.

[111] S. M. Lee, R. Vetury, J. D. Brown, S. R. Gibb, W. Z. Cai, J. M. Sun, D. S. Green, and J. Shealy, "Reliability assessment of AlGaN/GaN HEMT technology on SiC for 48V applications," *2008 Ieee International Reliability Physics Symposium Proceedings - 46th Annual,* pp. 446-449, 2008.

[112] M. G. Ancona, S. C. Binari, and D. J. Meyer, "Fully coupled thermoelectromechanical analysis of GaN high electron mobility transistor degradation," *Journal of Applied Physics,* vol. 111, Apr 1 2012.

[113] J. Joh, F. Gao, T. Palacios, and J. A. del Alamo, "A model for the critical voltage for electrical degradation of GaN high electron mobility transistors," *Microelectronics Reliability,* vol. 50, pp. 767-773, Jun 2010.

[114] M. D. Hodge, R. Vetury, J. Shealy, and R. Adams, "A Robust AlGaN/GaN HEMT Technology for RF Switching Applications," in *Compound Semiconductor Integrated Circuit Symposium (CSICS), 2011 IEEE*, 2011, pp. 1-4.

[115] B. D. Christiansen, R. A. Coutu, E. R. Heller, B. S. Poling, G. D. Via, R. Vetury, and J. B. Shealy, "Reliability Testing of AlGaN/GaN HEMTs under Multiple Stressors," *2011 Ieee International Reliability Physics Symposium (Irps),* 2011.

[116] P. Makaram, J. Joh, J. A. del Alamo, T. Palacios, and C. V. Thompson, "Evolution of structural defects associated with electrical degradation in AlGaN/GaN high electron mobility transistors," *Applied Physics Letters,* vol. 96, Jun 7 2010.

[117] C. Y. Chang, T. Anderson, J. Hite, L. Lu, C. F. Lo, B. H. Chu, D. J. Cheney, E. A. Douglas, B. P. Gila, F. Ren, G. D. Via, P. Whiting, R. Holzworth, K. S. Jones, S. Jang, and S. J. Pearton, "Reverse gate bias-induced degradation of AlGaN/GaN high electron mobility transistors," *Journal of Vacuum Science & Technology B,* vol. 28, pp. 1044-1047, Sep-Oct 2010.

[118] C. Y. Chang, E. A. Douglas, J. Kim, L. Lu, C. F. Lo, B. H. Chu, D. J. Cheney, B. P. Gila, F. Ren, G. D. Via, D. A. Cullen, L. Zhou, D. J. Smith, S. Jang, and S. J. Pearton, "Electric-Field-Driven Degradation in OFF-State Step-Stressed AlGaN/GaN High-Electron Mobility Transistors," *Ieee Transactions on Device and Materials Reliability,* vol. 11, pp. 187-193, Mar 2011.

[119] E. A. Douglas, C. Y. Chang, B. P. Gila, M. R. Holzworth, K. S. Jones, L. Liu, J. Kim, S. Jang, G. D. Via, F. Ren, and S. J. Pearton, "Investigation of the effect of temperature during off-state degradation of AlGaN/GaN High Electron Mobility Transistors," *Microelectronics Reliability,* vol. 52, pp. 23-28, Jan 2012.

[120] S. Einfeldt, H. Heinke, V. Kirchner, and D. Hommel, "Strain relaxation in AlGaN/GaN superlattices grown on GaN," *Journal of Applied Physics,* vol. 89, pp. 2160-2167, Feb 15 2001.

[121] S. Choi, E. Heller, D. Dorsey, and S. Graham, "Analysis of the residual stress distribution in AlGaN/GaN high electron mobility transistors," *Journal of Applied Physics,* vol. 113, 2013.

[122] Z. Q. Fang, B. Claflin, and D. C. Look, "Deep Traps in AlGaN/GaN Heterostructure Field-Effect Transistors Studied by Current-Mode Deep-Level Transient Spectroscopy: Influence of Device Location," *Journal of Electronic Materials,* vol. 40, pp. 2337-2343, Dec 2011.

[123] Y. F. Wu, M. Moore, A. Saxler, T. Wisleder, and P. Parikh, "40-W/mm Double Field-plated GaN HEMTs," in *Device Research Conference, 2006 64th*, 2006, pp. 151-152.

[124] S. Choi, E. R. Heller, D. Dorsey, R. Vetury, and S. Graham, "The Impact of Bias Conditions on Self-Heating in AlGaN/GaN HEMTs," *IEEE Transactions on Electron Devices,* vol. 60, pp. 159 - 162 2013.

[125] S. Demirtas, J. Joh, and J. A. del Alamo, "High voltage degradation of GaN High Electron Mobility Transistors on silicon substrate," *Microelectronics Reliability,* vol. 50, pp. 758-762, Jun 2010.

[126] M. Meneghini, A. Stocco, M. Bertin, D. Marcon, A. Chini, G. Meneghesso, and E. Zanoni, "Time-dependent degradation of AlGaN/GaN high electron mobility transistors under reverse bias," *Applied Physics Letters,* vol. 100, Jan 16 2012.

[127] A. V. Sotnikov, H. Schmidt, M. Weihnacht, E. P. Smirnova, T. Y. Chemekova, and Y. N. Makarov, "Elastic and Piezoelectric Properties of AlN and LiAlO2 Single Crystals," *Ieee Transactions on Ultrasonics Ferroelectrics and Frequency Control,* vol. 57, pp. 808-811, Apr 2010.

[128] *Sentaurus Device User Manual*, Ver. A-2007.12 ed. Mountain View, CA: Synopsys, Inc., 2007.

[129] *ANSYS/Mechanical Software Suite*. Canonsburg, PA: ANSYS, Inc.

[130] *Introduction to COMSOL Multiphysics, VERSION 4.2a*. Los Angeles, CA: COMSOL Inc., 2011.

[131] S. Choi, E. R. Heller, D. Dorsey, R. Vetury, and S. Graham, "Thermometry of AlGaN/GaN HEMTs Using Multispectral Raman Features," *IEEE Transactions on Electron Devices,* vol. 60, pp. 1898-1904, 2013.

[132] R. O. A. Hall, "The thermal expansion of silicon.," *Acta Crystallographica,* vol. 14, pp. 1004-1005, 1961.

[133] J. J. Hall, "Electronic Effects in the Elastic Constants of n-Type Silicon," *Physical review,* vol. 161, pp. 756-761, 1967.

[134] C. J. Glassbrenner and G. A. Slack, "Thermal Conductivity of Silicon + Germanium from 3 Degrees K to Melting Point," *Physical Review a-General Physics,* vol. 134, pp. 1058-&, 1964.

[135] W. Soluch, E. Brzozowski, M. Lysakowska, and J. Sadura, "Determination of Mass Density, Dielectric, Elastic, and Piezoelectric Constants of Bulk GaN Crystal," *Ieee Transactions on Ultrasonics Ferroelectrics and Frequency Control,* vol. 58, pp. 2469-2474, Nov 2011.

[136] L. Patrick and W. J. Choyke, "Static Dielectric Constant of Sic," *Physical Review B,* vol. 2, pp. 2255-&, 1970.

[137] A. P. Mirgorodsky, M. B. Smirnov, E. Abdelmounim, T. Merle, and P. E. Quintard, "Molecular Approach to the Modeling of Elasticity and Piezoelectricity of Sic Polytypes," *Physical Review B,* vol. 52, pp. 3993-4000, Aug 1 1995.

[138] M. A. D. Maur, G. Romano, and A. Di Carlo, "Electro-Thermo-Mechanical Simulation of AlGaN/GaN HEMTs," *2012 15th International Workshop on Computational Electronics (Iwce),* 2012.

[139] W. Saito, Y. Kakiuchi, Y. Saito, K. Tsuda, I. Omura, and M. Yamaguchi, "Suppression of dynamic on-resistance increase and gate charge measurements in high-voltage GaN-HEMTs with optimized field-plate structure," *Ieee Transactions on Electron Devices,* vol. 54, pp. 1825-1830, Aug 2007.

[140] L. Liu, T. S. Kang, D. A. Cullen, L. Zhou, J. Kim, C. Y. Chang, E. A. Douglas, S. Jang, D. J. Smith, S. J. Pearton, W. J. Johnson, and F. Ren, "Effect of source field plate on the characteristics of off-state, step-stressed AlGaN/GaN high electron mobility transistors," *Journal of Vacuum Science & Technology B,* vol. 29, May 2011.

[141] S. Demirtas and J. A. del Alamo, "Effect of Trapping on the Critical Voltage for Degradation in GaN High Electron Mobility Transistors," *2010 International Reliability Physics Symposium,* pp. 134-138, 2010.

[142] Y.-F. C. Wu, R. ; Fichtenbaum, N. ; Dora, Y. ; Suh, C.S. ; Shen, L. ; Parikh, P. ; Mishra, U.K. , "Total GaN solution to electrical power conversion," presented at the Device Research Conference (DRC), 2011 69th Annual, Transphorm Inc., Goleta, CA, USA 2011.

[143] S. Y. Park, C. Floresca, U. Chowdhury, J. L. Jimenez, C. Lee, E. Beam, P. Saunier, T. Balistreri, and M. J. Kim, "Physical degradation of GaN HEMT devices under high drain bias reliability testing," *Microelectronics Reliability,* vol. 49, pp. 478-483, May 2009.

[144] E. A. Douglas, C. Y. Chang, D. J. Cheney, B. P. Gila, C. F. Lo, L. Lu, R. Holzworth, P. Whiting, K. Jones, G. D. Via, J. Kim, S. Jang, F. Ren, and S. J. Pearton, "AlGaN/GaN High Electron Mobility Transistor degradation under on- and off-state stress," *Microelectronics Reliability,* vol. 51, pp. 207-211, Feb 2011.

[145] M. Kuball, M. Tapajna, R. J. T. Simms, M. Faqir, and U. K. Mishra, "AlGaN/GaN HEMT device reliability and degradation evolution: Importance of diffusion processes," *Microelectronics Reliability,* vol. 51, pp. 195-200, Feb 2011.

[146] F. Gao, B. Lu, L. B. Li, S. Kaun, J. S. Speck, C. V. Thompson, and T. Palacios, "Role of oxygen in the OFF-state degradation of AlGaN/GaN high electron mobility transistors," *Applied Physics Letters,* vol. 99, Nov 28 2011.

[147] F. Gao, D. Chen, B. Lu, H. L. Tuller, C. V. Thompson, S. Keller, U. K. Mishra, and T. Palacios, "Impact of Moisture and Fluorocarbon Passivation on the Current Collapse of AlGaN/GaN HEMTs," *Ieee Electron Device Letters,* vol. 33, pp. 1378-1380, Oct 2012.

[148] A. Sarua, T. Batten, H. Ji, M. J. Uren, T. Martin, and M. Kuball, "Thermal and Piezoelectric Stress in Operating AlGaN/GaN HFET Devices and Effect of the Fe Doping in the GaN Buffer Layer," presented at the CS MANTECH Conference, Tampa, Florida, USA, 2009.